Quality of heart rate variability features obtained from ballistocardiograms

by

Ahmad Suliman

B.S., Kabul University, 2003

M.S., Kansas State University, 2010

AN ABSTRACT OF A DISSERTATION

submitted in partial fulfillment of the
requirements for the degree

DOCTOR OF PHILOSOPHY

Department of Electrical and Computer Engineering
College of Engineering

KANSAS STATE UNIVERSITY
Manhattan, Kansas

2019

Abstract

Heartbeat intervals (HBIs) vary over time, and that variance can be quantified as heart rate variability (HRV). HRV has several health-related applications including long-term health monitoring and sleep quality assessment.

The focus of this research is obtaining HRV from ballistocardiograms (BCGs), force signals caused by micro-movements of the human body in response to blood ejections. This method of HRV estimation is attractive because it does not require direct attachment of any sensor to the body. However, the HBIs and corresponding HRV measured with BCGs are different than those obtained via electrocardiograms (ECGs), signals obtained by attaching electrodes to the body to detect electrical heart activity. Because ECG-based HRV is typically considered ground truth, differences in BCG-based versus ECG-based parameters are referred to as HBI and HRV errors.

This research investigates the effects of HBI error on HRV feature quality. While a few studies have used BCG-based HBIs to estimate HRV features for sleep staging, the effects of HBI error on the quality of the resulting HRV features seem to have been overlooked. As a result, an acceptable HBI error range has not been defined. One contribution of this work is the development of such an acceptable error range.

This dissertation work (*i*) develops a hardware and software system necessary to record BCGs and to perform BCG peak detection to obtain HBIs with the least possible error, (*ii*) determines an allowable range for HBI error by studying the effects of this error on HRV quality in the context of HRV-based sleep staging, and (*iii*) compares the determined acceptable HBI error range to the HBI error of our final system. The inherent error in BCG-based HBI determination due to physiological and platform effects is also taken into account in this comparison.

A minimum HBI error of 20 ms was obtained from the system developed in (*i*), and the allowable error range was determined to be 30 ms based on the investigations conducted in (*ii*). The combined physiological and platform effects led to an error of 8.8 ms on average. Based on the comparisons conducted in (*iii*), the developed system is suitable for long-term sleep quality assessment. In addition, the effects of the HBI errors introduced by this system on the resulting HRV features are negligible in the sleep staging context.

Quality of heart rate variability features obtained from ballistocardiograms

by

Ahmad Suliman

B.S., Kabul University, 2003

M.S., Kansas State University, 2010

A DISSERTATION

submitted in partial fulfillment of the
requirements for the degree

DOCTOR OF PHILOSOPHY

Department of Electrical and Computer Engineering
College of Engineering

KANSAS STATE UNIVERSITY
Manhattan, Kansas

2019

Approved by:

Major Professor
David E. Thompson

Copyright

Abstract

Heartbeat intervals (HBIs) vary over time, and that variance can be quantified as heart rate variability (HRV). HRV has several health-related applications including long-term health monitoring and sleep quality assessment.

The focus of this research is obtaining HRV from ballistocardiograms (BCGs), force signals caused by micro-movements of the human body in response to blood ejections. This method of HRV estimation is attractive because it does not require direct attachment of any sensor to the body. However, the HBIs and corresponding HRV measured with BCGs are different than those obtained via electrocardiograms (ECGs), signals obtained by attaching electrodes to the body to detect electrical heart activity. Because ECG-based HRV is typically considered ground truth, differences in BCG-based versus ECG-based parameters are referred to as HBI and HRV errors.

This research investigates the effects of HBI error on HRV feature quality. While a few studies have used BCG-based HBIs to estimate HRV features for sleep staging, the effects of HBI error on the quality of the resulting HRV features seem to have been overlooked. As a result, an acceptable HBI error range has not been defined. One contribution of this work is the development of such an acceptable error range.

This dissertation work (*i*) develops a hardware and software system necessary to record BCGs and to perform BCG peak detection to obtain HBIs with the least possible error, (*ii*) determines an allowable range for HBI error by studying the effects of this error on HRV quality in the context of HRV-based sleep staging, and (*iii*) compares the determined acceptable HBI error range to the HBI error of our final system. The inherent error in BCG-based HBI determination due to physiological and platform effects is also taken into account in this comparison.

A minimum HBI error of 20 ms was obtained from the system developed in (*i*), and the allowable error range was determined to be 30 ms based on the investigations conducted in (*ii*). The combined physiological and platform effects led to an error of 8.8 ms on average. Based on the comparisons conducted in (*iii*), the developed system is suitable for long-term sleep quality assessment. In addition, the effects of the HBI errors introduced by this system on the resulting HRV features are negligible in the sleep staging context.

Table of Contents

List of Figures

List of Tables

Acknowledgments

First and foremost, I would like to extend my sincere thanks to my supervisor Dr. David E. Thompson I would never be able to finish this work without his inspiration and guidance.

I would also like to express my deepest and genuine appreciations to my doctoral committee members Dr. Steve Warren, Dr. Dwight Day, Dr. Punit Prakash and Dr. Dale Schinstock.

A special thank you goes to Dr. Dwight Day again and Dr. Sanjoy Das. I got an opportunity to join K-State again for my doctoral degree because of their confidence in me.

I can't appreciate enough the support I got from the ECE Department and I would like to acknowledge the Student Opportunity Award Fellowship (Fall 2014 and Spring 2015).

Above all, I would never pursue PhD without encouragement from my father and mother. Unconditional love and support from my spouse, Frozaan Suliman, during challenging times have been a great inspiration. I know Saarah (10), Haajar (7), Aasyah (6) and Aayeshah (3) have missed a lot during this endeavor.

Chapter 1

Introduction

Heart rate variability (HRV) is the measurement of variations in the heartbeat intervals (HBIs). HRV features have applications in the field of sleep staging [1–5] and other sleep quality assessments [6, 7]. In addition, HRV is useful for long-term heart health monitoring and other clinical research [8, 9]. In [8], HRV is used to investigate relations between cardiac autonomic modulations and breast cancer, and [9] investigates HRV as a measure of subjective well-being. This latter study aims to enable assessment of psychological processes through physiology.

To extract HRV features, it is necessary to obtain HBIs. In a clinical setting, HBIs are obtained by detecting the heartbeats from electrocardiograms (ECGs) [10–12] or photoplethysmograms (PPGs) [11]. In ECG, HBIs are estimated from the time between consecutive R-peaks of the ECG signal, and is also termed R-to-R interval (RRI). With PPG, HBIs are estimated from the time between consecutive peaks of the pulse signal, and is therefore sometimes called the pulse-to-pulse interval (PPI) [13] (the resulting HRV measurement may be called pulse rate variability (PRV)). HRV obtained from ECG is considered ground truth (GT) whenever the performance of an alternative method for HRV estimation is evaluated [2, 14–21].

1.1 Motivation

Due to the growing need for long-term health monitoring, which includes sleep quality assessment, nighttime data recording is necessary. Essential types of nighttime data include HRV, breathing and restlessness information. HRV and breathing information may be obtained from an ECG or PPG. However, ECG requires worn electrodes and PPG requires a worn optical sensor (e.g. a finger clip). As a result, both approaches are not ideal for long-term health monitoring applications because these attached devices are either uncomfortable or can become detached easily. In addition, certain populations, such as those with autism, may find wearable devices completely intolerable.

One of several unobtrusive alternatives to ECG or PPG is the ballistocardiogram (BCG). BCG is a signal resulting from micro-movements of the human body caused by blood ejections from the heart. Heartbeat detection or heart rate estimation using BCG has seen recent research interest [22] among other non-contact heartbeat detection methods. Because it is non-contact, BCG is suitable for long-term health monitoring. However, the sensors must be mounted to a platform. In addition, the platform to be considered should involve substantial day-to-day interaction with the population of interest. Therefore, we chose a bed-mounted system, as most people get 6-10 hours of sleep and it potentially allows us to monitor sleep quality as well as cardiac health.

The prominent peaks of the BCG are called the J peaks and represent the blood ejection at the aortic artery. It is possible to estimate HRV features from the HBI obtained using J-to-J peak intervals (JJIs) of the BCG [1].

An example of obtaining RRI and JJI estimates from simultaneous ECG and BCG recordings from a bed system is illustrated in Fig. 1.1. Clearly, the HRV features obtained from the JJIs are not the same as the features obtained from the RRIs. The discrepancies between ECG and BCG-based HRV features stem from three main sources: (i) the underlying dif-

[1] A note on terminology: different references in this study have used heartbeat intervals (HBIs) or beat-to-beat intervals (BBIs) to refer to J-to-J interval (JJIs). This dissertation reserves the term HBI to refer to heartbeat interval regardless of the ECG or BCG being its source signal. RRI and JJI is used in this work to explicitly refer to ECG-based and BCG-based HBIs, respectively. Furthermore, HBI error refers to the RRI-JJI difference, since ECG is typically considered GT for these comparisons.

ferences in the cardiac physiology captured by an ECG and a BCG, (*ii*) the errors involved in the process of BCG detection and peak identification or in other words, the errors due to the technology involved in JJI estimation, and (*iii*) platform or bed effects related to the coupling between heart forces and the sensors. These sources of error are discussed in 1.1.1, 1.1.2 and 1.1.3, respectively.

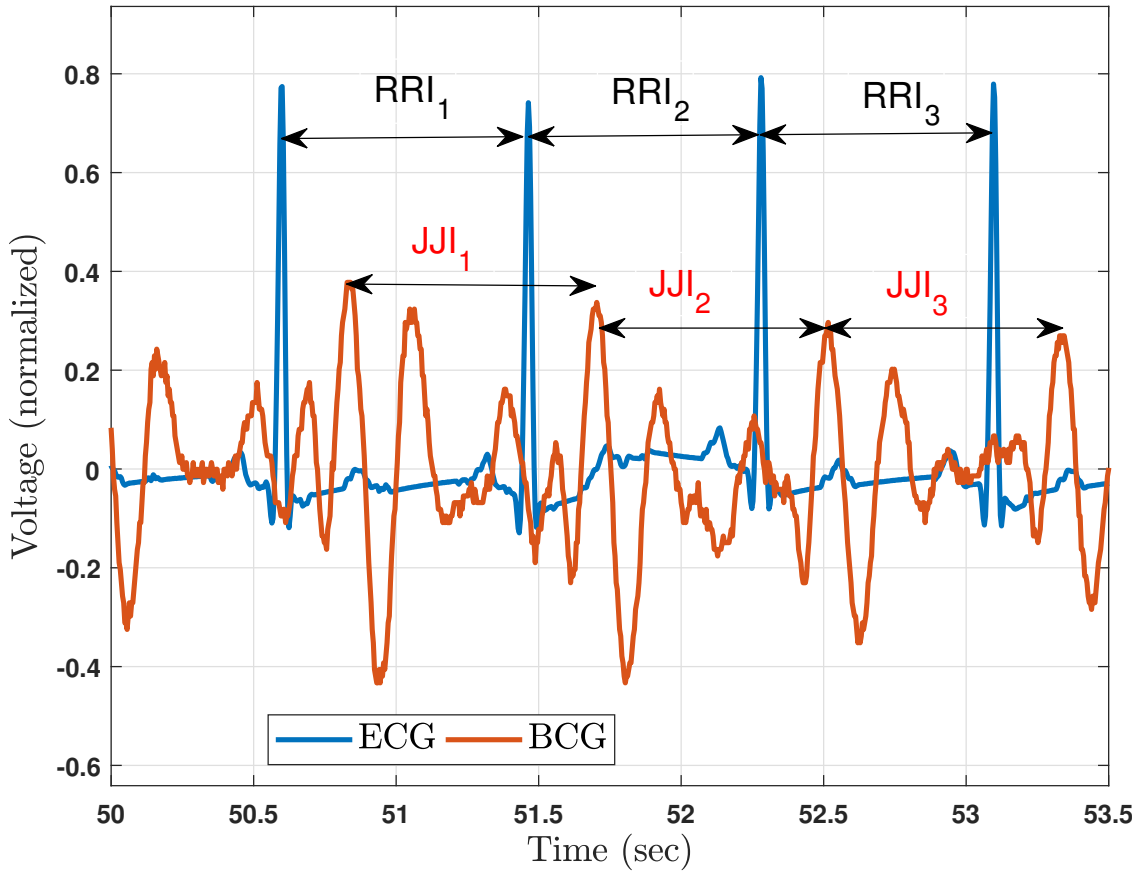

Figure 1.1: RRI and JJI estimates from simultaneous ECG and BCG recordings.

While the discrepancies in JJI and RRI-based HRV features due to physiology are inevitable, the technology-based error sources are technology-dependent and should be minimized. In addition, we wish to know if the differences between HBI collected with ECG and BCG have any significant impacts on the quality of the resulting HRV estimate.

To that end, this dissertation focuses on assessment of quality of the JJI-based HRV features. To conduct this assessment, this dissertation relies on a bed system built collaboratively by several lab members, including the author. The bed is primarily intended for

sleep, health, and activity monitoring of severely disabled autistic children [23–27]. This bed is equipped with two types of force sensors to record BCG, namely, electromechanical films (EMFi) and load cells. These two forms of force sensors were chosen because they are commercially available in compact form. Due to the compact form of the EMFi and load cells, these sensors can beintegrated into the bed mattress or frame. This, in turn, makes bed relocation and bedroom remodeling relatively hassle-free, which is a significant benefit for long-term health monitoring and sleep study applications.

When assessing the impact of sensors on the BCG quality, this dissertation focuses on the signals obtained from the load cells. This is because the load cells provide us with the bed user's weight information which can then be used to track their center of pressure (COP). The advantage of being able to track the COP is a benefit of these sensors, because COP provides information about restlessness during sleep [28]. The assessment of restlessness during sleep is an essential part of sleep quality assessment.

1.1.1 The physiological source of the HBI error

ECG and BCG represent two different types of cardiac activity. The former is related to the electrical cardiac activity and the latter is related to the mechanical cardiac activity. In that context, the R peaks represent ventricular contraction events and J peaks represent blood ejection events at the aortic artery. Therefore, there is always an inherent delay between the R peak of an ECG and the J peak of a BCG. This delay is called the R-to-J interval (RJI) and is indicated in Fig. 1.2 with RJI_1, RJI_2, and RJI_3. In addition, the blood ejection event at the aortic artery doesn't happen at a constant time offset from the ventricular contraction event. Therefore, RJIs vary over time, i.e., RJI_1, RJI_2 and RJI_3 in Fig. 1.2 are not equal. This variability in RJI is one factor in the RRI-JJI difference or HBI error.

1.1.2 The technological sources of the HBI error

This source of error is mainly related to hardware involved in BCG detection and the signal processing employed in J peak identification. One point of concern is the temporal accuracy

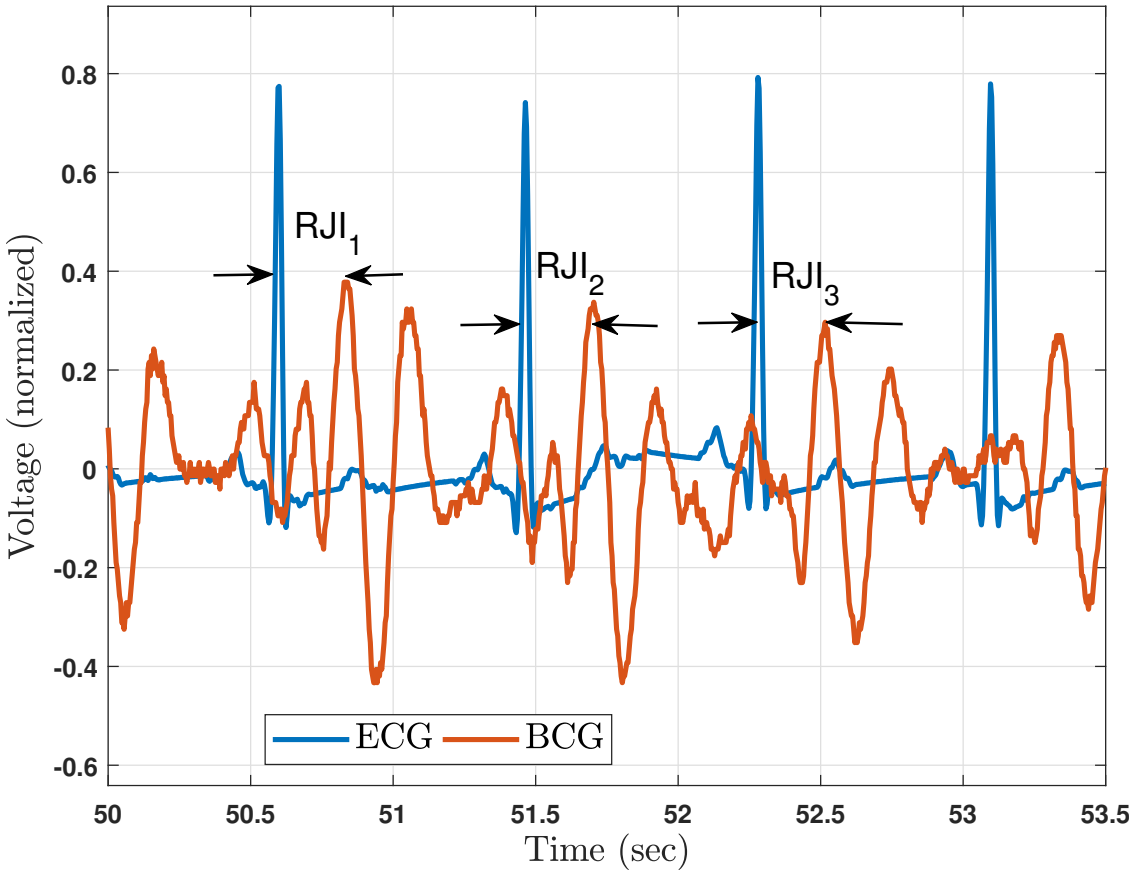

Figure 1.2: RJIs compared from simultaneous ECG and BCG recordings.

of the detected J peaks. Missed and false J peaks also contribute to HRV error. This is because HRV feature extraction involves heavily overlapped HBI windows, where effects of individual missed or false J peak gets distributed over multiple windows leading to additional error in the HRV. Fig. 1.3 shows the perturbations in the detected J peaks and Fig. 1.4 shows the missed J peaks in BCG26 (upper signal) compared to a cleaner J peak detection example in BCG19 (lower signal). The RRI and JJI are compared in the plot of Fig. 1.5. The spike in the JJI curve of the Fig. 1.5 is due to a missed J peak.

1.1.3 The HBI error related to heart force to sensor coupling effects due to the platform

There is a variable delay between the time the body exerts the force due to the cardiac activity to the bed and the time the sensor detects the force. However, for a particular

person who uses a particular platform, the variability of this delay is limited to the postures the person takes in the course of a data recording session. Since this work focuses in long-term and longitudinal data recording, it is safe to neglect the RJI variability due to body-to-force sensor coupling. Therefore, this variability is not addressed in this work.

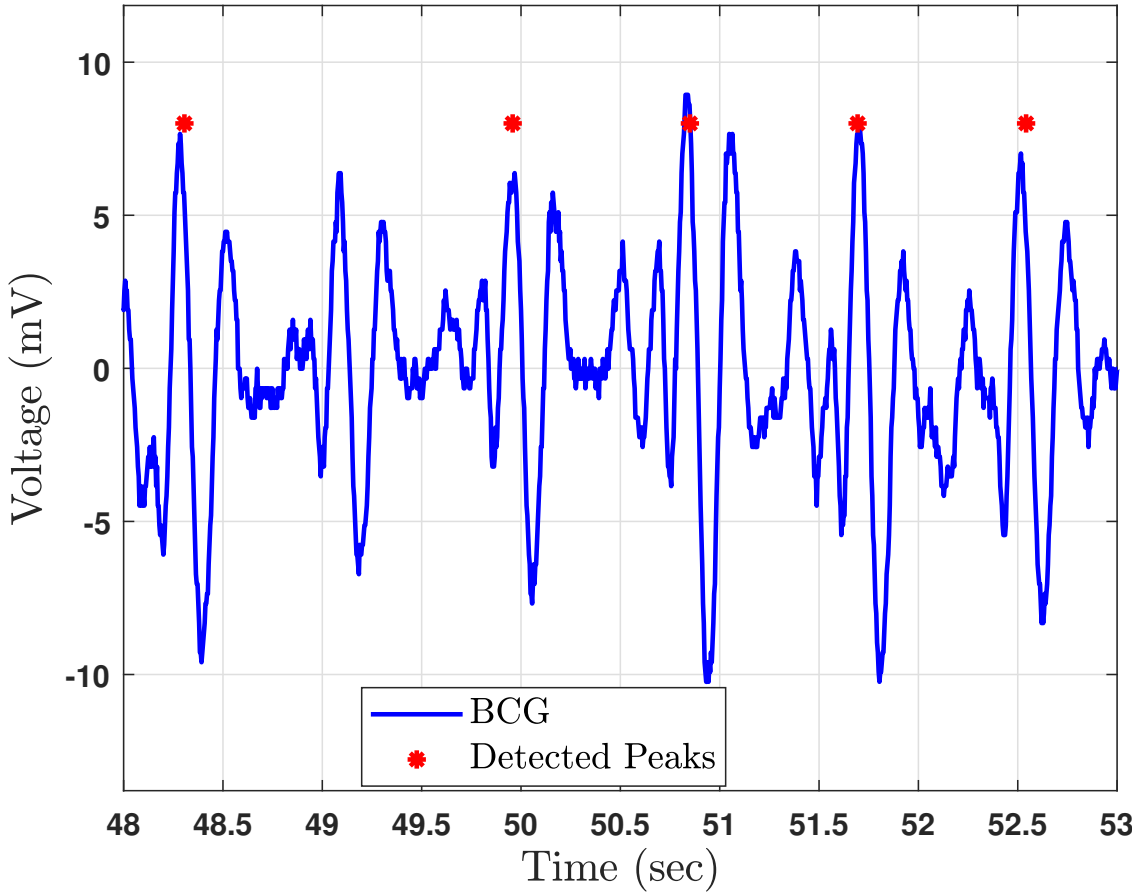

Figure 1.3: An example of perturbations in J peak detection due to peak detection algorithms.

Fig. 1.6 shows the overall system overview and summarizes different sources of error, e.g., data acquisition configurations, sensors, i.e. load cells in this case, and BCG peak detection algorithms.

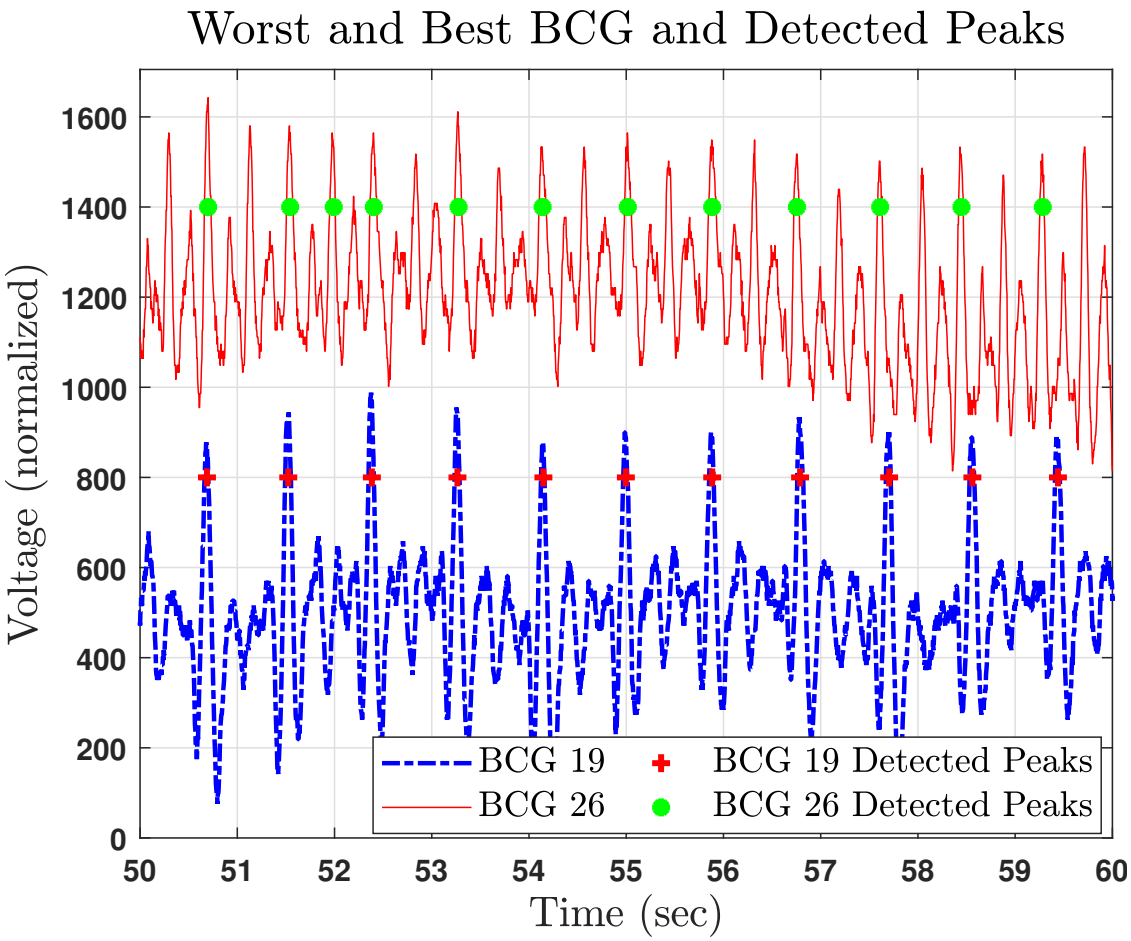

Figure 1.4: Peak detection examples of clean (BCG 19 and its peaks) and erroneous (BCG 26 and its peaks) due to technology.

1.2 Literature review

1.2.1 Non-contact heartbeat detection methods

Different non-contact sensing alternatives to ECG are proposed in the literature. Examples include bed-mounted capacitive ECG (cECG) [29–34], mattress-based photoplethysmogram (PPG) [35] and PPG imaging [36–41]. cECG is similar to ECG, with the exception that it uses capacitive coupling with the skin instead of conventional ECG electrodes that are in direct contact with the skin. Mattress-based PPG and PPG imaging work on the principles of PPG, i.e., tracking the changes in the skin's optical characteristics due to changes in the blood volume with each heartbeat. Mattress-based PPG is obtained by placing a PPG

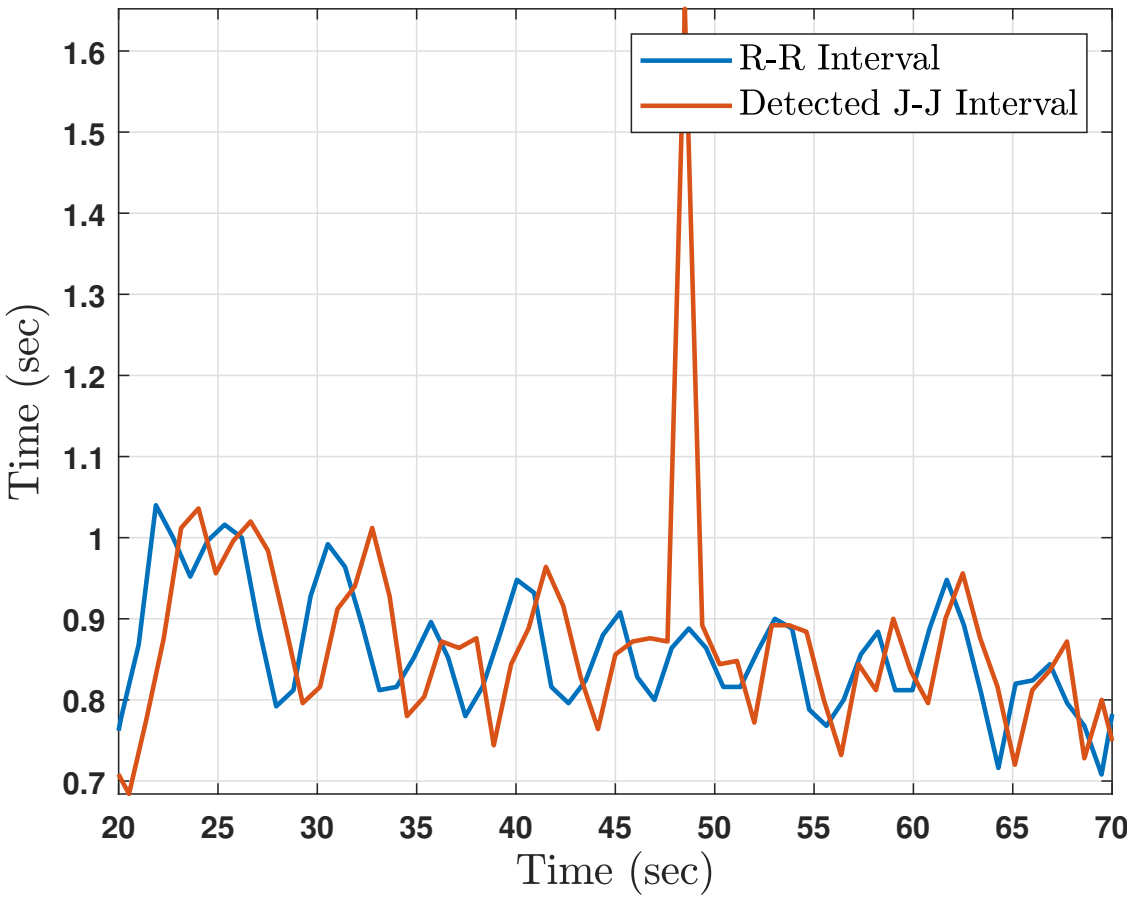

Figure 1.5: RRIs and JJIs from detected J peaks compared for simultaneous ECG and BCG recordings.

sensor on the mattress beneath its white sheet instead of placing it on a fingertip [35]. PPG imaging, on the other hand, replaces the optical sensors of the PPG with a camera that takes images of the skin. Thus, it provides a means to track the chromatic changes in skin due to blood volume changes with each heartbeat.

These sensing modalities, however, come with drawbacks. For example, cECG is considered as a wearable sensing technique rather than a non-contact technique [42]. On the other hand, PPG imaging proposed in [36–41] is not yet bed based as its latest account in [41] is still recorded in a sitting position.

Radar based methods [43–56] are also proposed as a non-contact means for vital sign detection. In this approach, the distance variations due to body movements are measured. Such movements are caused by physiological activities e.g. respiration and heartbeats. How-

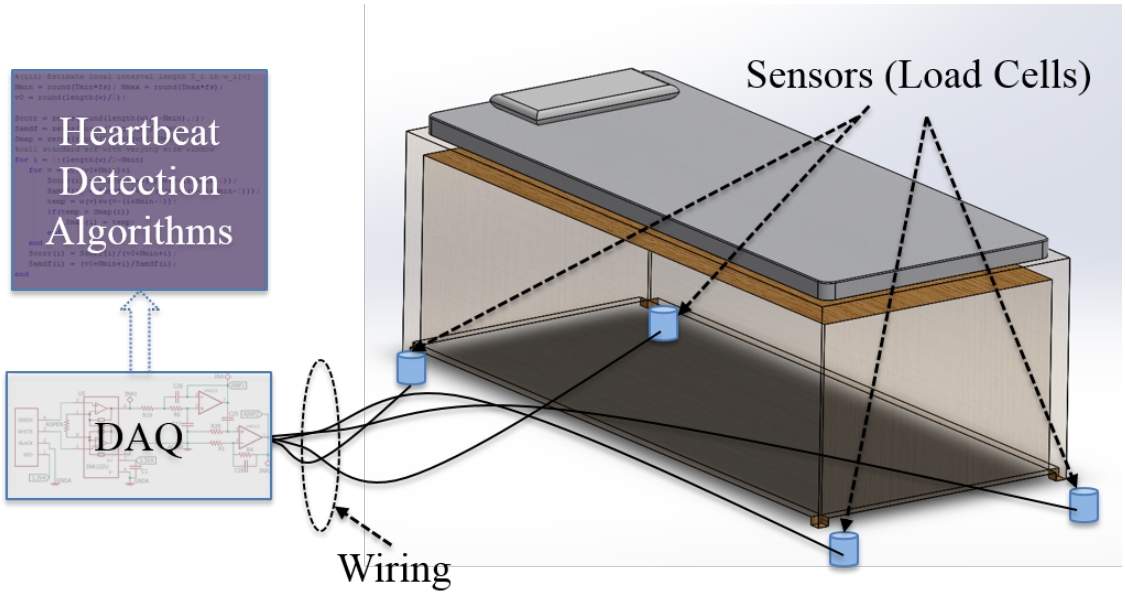

Figure 1.6: Overall system overview with main sources of HBI error (3D representation of bed courtesy of Charles Carlson).

ever, this method also works best when participants are in a seated position as concluded in [52]. Of the references mentioned, only three studies [51–53] have performed measurements from participants in a supine position. It is worth mentioning that physiological signal inferred from this technique is also called BCG in [54]. The reason for this goes back to the definition of BCG which is body micro movements due to cardiovascular activities.

Another non-contact method for heart beat detection is optical Doppler-based or laser-based techniques [57–62]. These studies also involve experiments with sitting participants except in [62] where the experiment is done with one subject in supine position in a lab setting. The flexibility and feasibility to adapt the laser-based techniques in a home setting is not yet addressed.

A limiting factor for remote sensing techniques such as radar Doppler, camera and laser (optical Doppler) is the problem of small range of coverage [63]. That is, if we want to use such systems for sleep studies, the bed occupant needs to remain at the exact same location throughout the sleep period. If the participant changes position or location, the monitoring process will be discontinued unless a tracking paradigm is also included. However, such a tracking scheme adds to the complexity and cost of the system, which is already high [64].

1.2.2 BCG: An alternative non-contact method

As other non-contact approaches mentioned above introduce some form of limitations, BCG is a promising signal that lacks the mentioned drawbacks. BCG in the form of body motion can be detected with force sensors that can be easily embedded in the patient home environment, including beds [19, 65–72] and chairs [73–75]. The capability of embedding force sensors in the bed makes it possible to overcome the limitations of other non-contact health monitoring systems as mentioned in 1.2.1. This, in turn, enables nighttime physiological data collection for long-term health monitoring and sleep quality assessment.

1.2.3 Sensing modalities for BCG detection

A variety of approaches are proposed in the literature to detect BCG. Most of the approaches are based on force sensing techniques. These approaches rely on the mechanical coupling of the body and the mattress or the platform. Due to this coupling, the body movements due to heartbeats can be measured as subtle motions of the mattress and the bed. Examples of optimal measurements include methods based on deformation of optical fibers in a mattress [76, 77] and infrared (IR) light scattering inside the mattress foam itself or in mattress cavities[65–67]. Other examples include strain gauges, conductive fibers, ultrasound sensors and pneumatic sensors. Strain gauges were employed to detect deformations of slats in a bed frame [19]. Conductive fibers were woven into a mattress [69] to measure changes in their conductance due small motions of the mattress caused by heartbeats. An ultrasound sensor was used to measure the deformation of a plate mounted underneath a mattress [70]. Pneumatic sensors in the form of air mattress [78] and air cushion [79], force coupling pads pneumatically coupled to a pressure sensor [80], air tubes [81] and water tubes [82, 83] are other alternatives proposed for BCG detection.

Commercially available force sensors for BCG detection include electromechanical films (EMFi) [17, 84, 85], Polyvinylidene Fluoride (PVDF) films [7, 86–89] and load cells [15, 20, 90–94]. To the best of our knowledge, [15, 20, 90–94] are the only references that have employed load cells for BCG detection. Of those, only [15, 90–92] have employed load cells to

detect BCG from a bed. The rest, i.e. [20, 93, 94], have used load cells to detect BCG from a weighing scale. Other groups have embedded load cells in the bed to detect respiration only as in [28] or to track the COP as in [7, 28, 88, 95]. Load cell-based COP tracking has been applied in quantifying the level of restlessness or restfulness of the sleep throughout the night [7, 28, 88, 95] which is an important metric in sleep quality assessment.

1.2.4 BCG-based HRV estimation for sleep staging

Sleep staging as a means of sleep quality assessment [96] is an important aspect of long-term health monitoring. In sleep medicine, sleep stages are labeled as rapid eye movement (REM) and non-rapid eye movement (N-REM) where the N-REM is further divided and labeled as S1, S2, S3 and S4 or as N1, N2 and N3. The former labeling is according to the Rechtschaffen Kales (R & K) rules [97] and the latter labeling is based on the American Academy of Sleep Medicine (AASM) guidelines revised in 2012 [98]. N3 is also called Slow Wave Sleep (SWS) which is equivalent to combined S3 and S4. Sleep staging in a clinical setting is performed using polysomnograms (PSGs) which is the gold standard for sleep staging. However, PSG requires many attached electrodes, and is thus not ideal for long term sleep staging. Therefore, alternatives are sought.

An alternative to PSG-based sleep staging is HRV-based sleep staging. Sleep stages are strongly correlated with the autonomic nervous system (ANS) activities [99, 100]. Furthermore, ANS activities influence heart rate [101] through the sympathetic and parasympathetic branches. Therefore, correlates of sleep stages can be inferred from HRV features. However, sleep staging with HRV typically lacks the resolution of PSG. Therefore, researchers using these techniques mostly classifysleep into REM and N-REM stages [84, 102] or SWS and non-SWS [91, 103]. To our findings, [104] is the only reference that has used HRV features to classify sleep into more stages, specifically Wake, N1, N2, "combined N1 and N2", SWS and REM. However, the reported accuracy is below 60%.

While most studies have used ECG-based HRV features for sleep staging, BCG-based HRV features have also shown promise. A classification accuracy of up to 80% is reported in

[84] based on HRV features obtained from BCG. The mentioned study analyzed data from 18 volunteers and classified sleep stages in in REM, N-REM and Wake [84]. This is comparable to the study conducted in [105] where ECG-based HRV features were used to classify REM and N-REM sleep stages on 25 participants, achieving 87% accuracy. The motion information included in [84] is believed to be a contributing factor in Wake stage classification [84]. In addition, results reported in [103] and [91] are comparable. The mentioned studies classify sleep in SWS and Non-SWS stages using HRV features obtained from ECG [103] and BCG [91]. Table 1.1 summarizes the studies that reported the highest sleep staging performance.

Table 1.1: Classification performance metrics based on HRV from ECG and BCG signals.

Signal Used	Stages Classified	Accuracy (%)	Sensitivity (%)	N	Cohen's Kappa	Study Referenced
ECG	SWS vs Non-SWS	90	69	45	0.56	[103]
ECG	SWS vs Non-SWS	81	N/A	10	N/A	[105]
BCG, Actigraphy	SWS vs Non-SWS	93	81	4	0.62	[91]
ECG	REM vs N-REM	87	87	25	0.61	[102]
ECG	REM vs N-REM	80	N/A	23	N/A	[105]
BCG, movement	REM vs N-REM	80	N/A	18	0.43	[84]

Higher accuracy, up to 89%, is also reported from other studies as quoted in [103]. However, those studies included other signals beside ECG. For example, [106, 107] has included data from respiratory impedance plethysmography (RIP) from a chest belt sensor.

Based on the performance metrics of Table 1.1 and the advantages listed for BCG, BCG-based HRV is a good candidate for sleep staging. While comparable to current ECG-based performance, BCG-based sleep staging can be further improved.

1.3 Contributions

The main contributions of this research are (*i*) designing the hardware configuration for a BCG data acquisition system, (*ii*) selecting an appropriate load cell that can detect the BCG with desirable quality, (*iii*) comparing existing BCG peak detection algorithms, and (*iv*) assessing the quality of the HRV obtained from the detected peaks of the BCG. A

brief summary of the mentioned contributions is provided in the following subsections, with references to each published work. The details for each of the main contributions listed above constitute the subsequent chapters of the dissertation.

1.3.1 The effects of data acquisition configurations on BCG quality

This part, detailed in Chapter 2, elaborates on inevitable impacts due to different data acquisition configurations. Three configurations are examined at the hardware level and their impacts on the test sine waves are quantified. Using the results of this work, one configuration was selected to evaluate and compare the effects of load cells on the quality of BCG which is covered in Chapter 3. Likewise, based on the conclusions of this work, another configuration was selected to record BCG for comparison of the BCG peak detection methods discussed in detail in Chapter 4.

1.3.2 The effects of load cell selection on BCG quality

This work is detailed in Chapter 3 and speaks to the impacts of different load cells on BCG quality. Among BCG sensing modalities discussed in 1.2.3, load cells are in the focus of this chapter. While some load cells do not respond at all to the frequency range of the BCG, others impact the quality of the detected signal. Therefore, four button-type load cells were selected for study in this work. The selection was based on either the readily availability of the load cell in the lab or their cost-effectiveness. Test forces in the forms of low-amplitude vibration, impulsive force and sine wave force were applied to the load cells. Subsequently, the impacts of the load cells on the detected signal due to the applied test forces were quantified. Using the results of this comparative study, the load cell with the least impact on the BCG was selected. The load cell selected based on the results of this investigation was used in the study discussed in Chapter 4 for BCG detection. Furthermore, the results of Chapters 2 and 3 complement the studies conducted by our group in [26, 108, 109].

1.3.3 Performance comparison of BCG peak detection methods

Since errors in the J peak detection is the main factor in HBI error, it is necessary to find a method that detects the J peaks with the least error possible. Therefore, this research, as presented in Chapter 4, compares performance of five signal processing and peak detection methods proposed in the literature. In addition, a cross-correlation approach is also included as a baseline for performance. The initial findings of this work are published in [110] and final results are published in [111]. Based on the results of this work, the best performing method was selected for BCG peak detection. The detected BCG peaks were then used to complement the study conducted in Chapter 5.

1.3.4 BCG-based HRV features quality assessment

In this study the clinical validity of HRV based on BCG peaks is examined. In particular, impacts of the HBI error on the quality of HRV features are quantitatively evaluated. The study begins with the error due to BCG peak detection by simulating it in the R-Peaks of ECG data available from the National Sleep Research Resource (NSRR) database. Since the ECG data are simultaneously collected with sleep scores in that database, it is possible to examine the effects of simulated error on the accuracy of sleep staging based on HRV features obtained from error-contaminated R-peaks. Then the error resulting in poor sleep staging accuracy is compared with the error due to the best BCG peak detection method identified in Chapter 4. The results of this study will help identify an allowable range of error in BCG peak detection algorithms. More details on this work is provided in Chapter 5.

Chapter 2

BCG detection hardware

2.1 Introduction

High-level system specifications for BCG detection hardware is available in the literature, e.g., corner frequencies for the signal conditioning circuits [112], and sampling rate and resolution for the data acquisition units [91]. However, two problems exist: (*i*) the provided information varies from research group to research group, with no unified set of values, and (*ii*) details on the configuration of different pieces of hardware cannot be inferred from the body of literature.

This chapter first introduces hardware involved in acquiring center of pressure (COP) and ballistocardiograms (BCGs), from a circuit and system point of view. An initial introduction to load cells as force sensors, together with two other types of film-based force sensors is provided in this chapter. A more detailed study of load cells is presented in Chapter 3. After introducing the hardware, the chapter investigates three proposed data acquisition configurations. The effects of these configurations on signal quality are quantified through initial sine wave force tests that (*i*) validate circuits' outputs and (*ii*) facilitate an objective comparison of the three configurations in terms of the signal to noise ratio (SNR) of the acquired signal. Pros and cons of each configuration are discussed.

The following sections introduce the force sensors typically used for BCG detection, the

signal conditioning and data acquisition configurations, and the testing process for those configurations. Ultimately, the system to be used for completing the subsequent chapters will be identified.

2.2 Platform description

Since this study is geared toward nighttime data collection in the home environment, the bed design described in [23–27] is considered here and in subsequent chapters. Fig. 2.1 shows a 3D representation of the platform, i.e., the bed, and how the load cells are positioned beneath its posts.

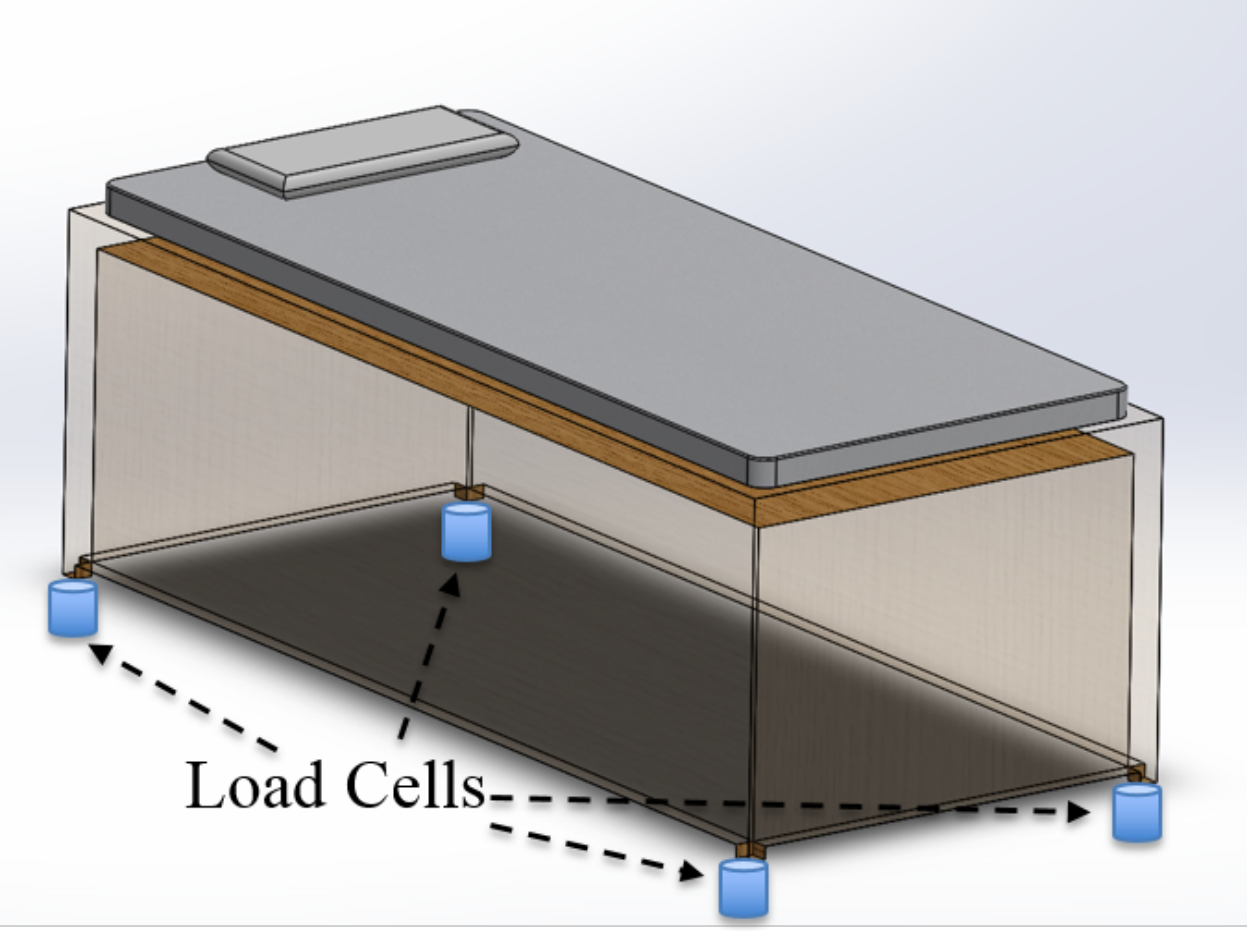

Figure 2.1: 3D representation of the bed (courtesy of Charles Carlson) and the position of load cells indicated by small cylinders beneath its posts.

2.3 Sensors

2.3.1 Load cells

A load cell is a transducer that converts applied force into an electrical output. Each button-type load cell utilized for this effort consists of a stainless steel housing that surrounds a collection of strain gauges arranged in a Wheatstone bridge configuration. When a compressive force is applied to the load cell, it produces a differential output voltage that is commensurate with the applied force. The sensitivity of the output voltage depends on the power source connected to the load cell; the output is rated in mV/V (mV of output signal per volt of excitation voltage at full rated compression). For example, for a 200-kg-rated load cell with a sensitivity of 1 mV/V powered with a 5 V source, a full 200 kg compressive load will generate an output of 5 mV.

2.3.2 Electromechanical films (EMFi's)

Electromechanical films (EMFis) are very thin (with a thickness of as low as 37 μm) polypropylene sheets. They are highly sensitive to forces applied in a normal direction with respect to their surface. Very subtle variations in the applied forces cause a variable voltage proportional to the applied force that can be measured across its output terminals [113]. Due to this high sensitivity, these sensors are used in vital sign monitoring studies as they can detect the micro-movements of the body caused by cardiovascular activities such as heartbeats and respiration. Such movements represent forces on the order of Newtons [114] and can still be detected by these sensors. These sensors are typically placed under the mattress in the mentioned applications.

2.3.3 Polyvinylidenefluoride (PVDF)

PVDF is made of piezoelectric material which is metallized to provide electrodes. A signal is detected on the mentioned electrodes when the film is compressed by any external force [113]. A version used in [113] came with a thickness of 110 μm metallized with silver ink.

Typically, these films are placed under the torso to capture both the BCG and respiration [88]. Since the material in both EMFi and PVDF is of a capacitive nature, only the variations in the applied force can be measured in the form of a variable voltage across their output terminals [113]. Therefore, they cannot be standalone sensors for a bed system where COP is also a signal of interest as discussed in 1.1 and 1.2.3. While both load cells and EMFi's were used in conducting the bed-based studies as in our previous works [25, 26, 108], this dissertation focuses on the load cell signals.

2.4 The signal conditioning circuit

Like many cardiopulmonary signals, a BCG is a low-frequency signal with a small pulsatile amplitude that rides on top of a much larger baseline (in this case, force from the combined weight of the bed and the subject). The BCG has cardiac frequency components in the range of approximately 0.5 to 20 Hz, whereas its respiration components primarily reside in the frequency range of approximately 0.05 to 0.7 Hz. In theory, one should be able to separate the constant voltage offset, or "DC" baseline, from the cardiac and respiration components using a highpass filter with a very low cutoff frequency. Considering these requirements, a signal conditioning circuit was designed. The block diagram in Fig. 2.2 describes the various steps involved in the signal conditioning circuit. Brief descriptions for each block in the block diagram of Fig. 2.2 are provided in 2.4.1 to 2.4.4.

2.4.1 Instrumentation amplifier (Inst Amp)

The instrumentation amplifier is a type of amplifier that amplifies the difference between the signals on its input terminals (Pins 2 and 3 of U5 in the circuit of Fig. 2.3). In our case, the input differential signal comes from the output terminals of the load cells. This signal is named "LC Signal" in the block diagram of Fig. 2.2. The gain of the instrumentation amplifier can be adjusted by connecting a gain resistor between a pair of its external pins (Pins 1 and 8 of U5 in the circuit of Fig. 2.3). The gain resistor is labeled as "ROPEN" in

the circuit of Fig. 2.3. It is worth mentioning that the useful gain for the instrumentation amplifier is limited by the aforementioned DC voltage offset from the weight of the bed and user. As a result, the adjustable gain of the instrumentation amp is useful primarily to address weight differences between populations or different bed setups.

2.4.2 Lowpass filter (LPF)

The LPF block is implemented with a unity gain, two-pole Sallen-Key lowpass filter with a corner frequency of 35 Hz. This LPF helps mitigate the effects of power line and other ambient high-frequency noise on the pre-amplified signal from the instrumentation amplifier's output. The output of this block contains both the weight on the load cell and the BCG riding on it. The weight information is labeled "Weight" in Fig. 2.2. The BCG, however, is too small to be directly detected due to the limited gain provided by the instrumentation amplifier as discussed in 2.4.1. Therefore, it needs further amplification after the removal of the DC offset.

2.4.3 Highpass filter (HPF)

The HPF is a single-pole passive filter with a corner frequency of 0.05 Hz. The HPF is necessary to block the high offset due to the weight signal that limits the amplification capability of the instrumentation amplifier as discussed in 2.4.1. Blocking the offset due to the weight signal will allow further amplification of the filtered signal for a detectable BCG. The low corner frequency of 0.05 Hz helps preserve respiration information at the same time which is necessary in sleep staging.

2.4.4 The amplifier (Amp)

The final amplifier (Amp) introduces a gain of 33 and applies a second stage of amplification to the BCG. This step is necessary because the signal on the output of the HPF is not large enough for direct quantization.

The circuit in Fig. 2.3 provides a low-level detail of the signal conditioning circuit described by the block diagram of Fig. 2.2. In the circuit, decoupling capacitors were used but such peripheral details are included in Appendix C.

The signal labeled as "ANP1" in the circuit of Fig. 2.3 is the lowpass-filtered signal carrying the weight information obtained by the load cell.The BCG is present in ANP1 as well, though it is smaller than the weight signal. The signal labeled "ANP2" is the highpass-filtered and amplified version of ANP1, which includes a detectable BCG.

Fig. 2.4 shows the printed circuit board (PCB) implementation of the circuit in Fig. 2.3. The particular PCB implementation shown in Fig. 2.4 is used in data acquisition

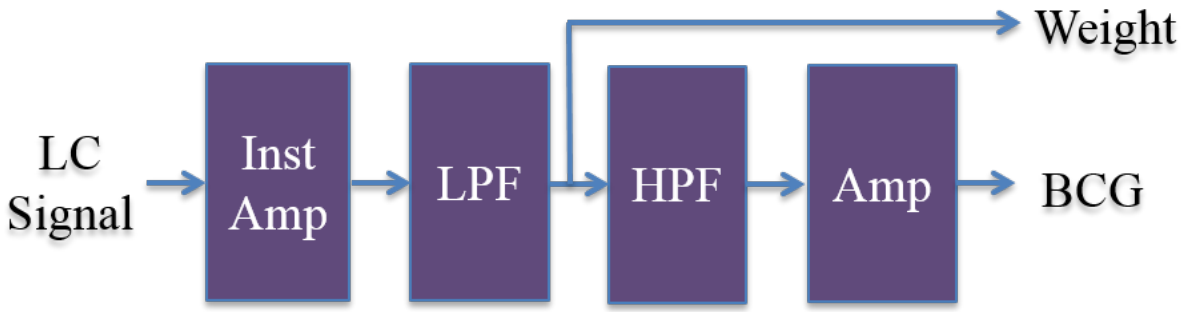

Figure 2.2: Block diagram of the signal conditioning circuit. The Amp has a gain of 33

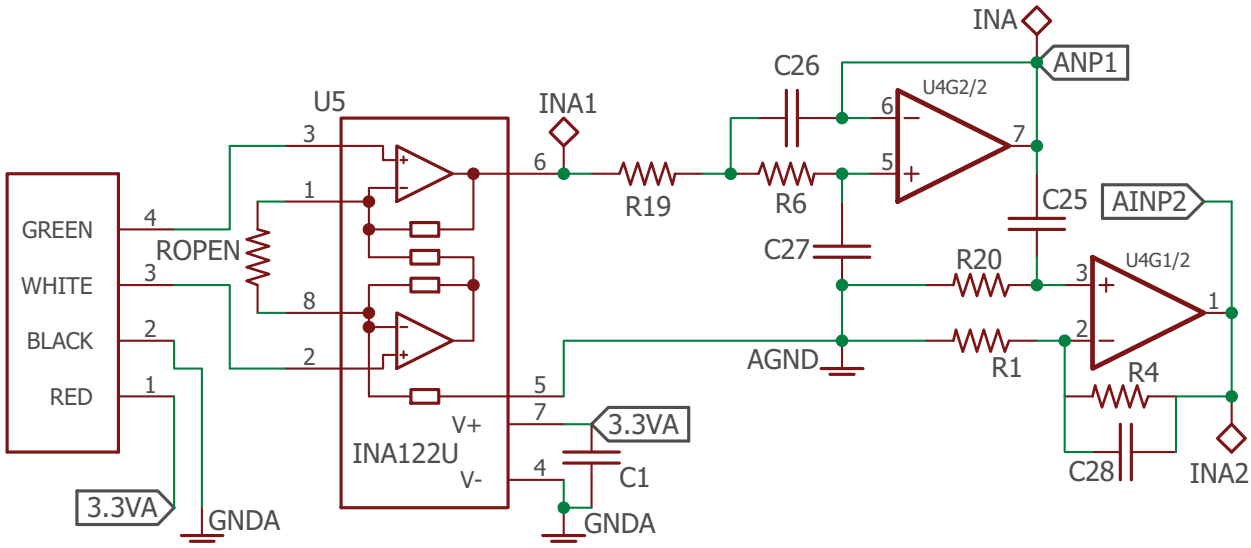

Figure 2.3: Circuit diagram realizing the signal conditioning.

configuration II as will be described in 2.5.2.

2.5 Data acquisition configurations

Signal quality is of a high concern in any application, and especially in this application with low-amplitude and low-frequency signals. As a rule of thumb, signal conditioning and conversion to digital signals should be performed near the sensor. However, since the load cells are located apart from each other at four corners of the bed, it is necessary to figure out an optimal location for the signal amplifier and analog to digital converter (ADC). Therefore, the following design alternatives were considered:

1. Apply signal conditioning and digitization as close to each load cell as possible and then transmit the digital signal to a central location for acquisition.

2. Apply signal conditioning as close to each load cell as possible and then transmit the amplified signal to a central location for digitization and acquisition.

3. Avoid any signal conditioning to the sensor signal as it may introduce electronics-induced noise to the signal. Instead, digitize the sensor output immediately with a

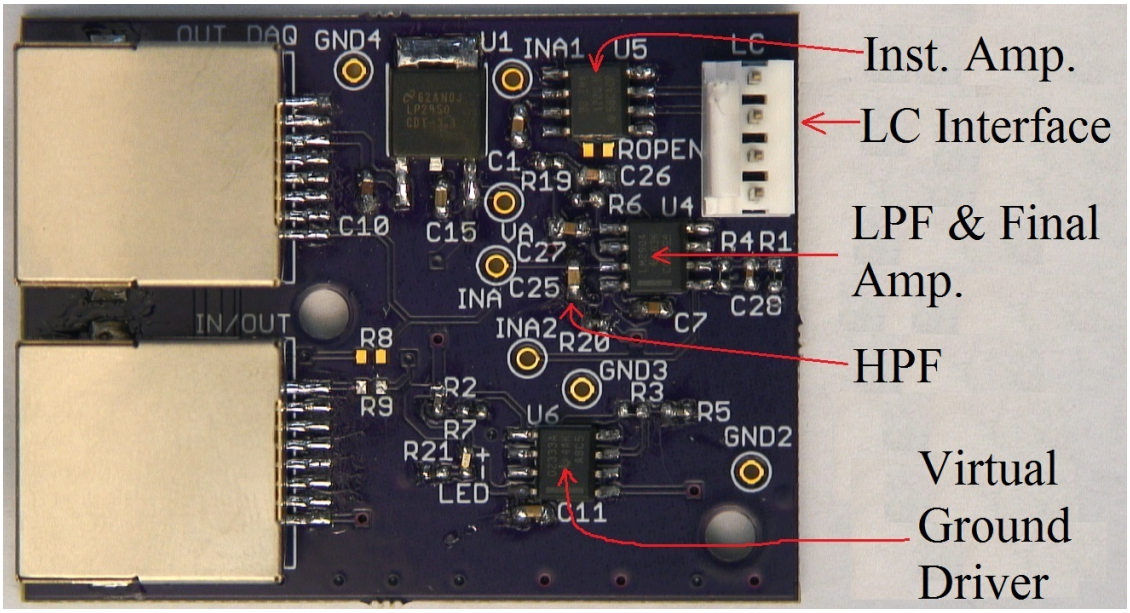

Figure 2.4: PCB implementation of the signal conditioning circuit.

higher-resolution ADC and transmit the digital signal to a central location for acquisition.

For that purpose, the signal conditioning and data acquisition combinations in the form of the following configurations were examined:

2.5.1 Configuration I: daisy-chain

This configuration, illustrated in Fig. 2.5, implements the first scenario. That is, signal conditioning and digitization are done as close to each load cell as possible. Then the digital signal is transmitted to a central location for acquisition through a serial peripheral interface (SPI) protocol. This approach is implemented with ADCs in a daisy chain configuration, to avoid requiring separate SPI connections between each ADC and the central acquisition unit, e.g., the microcontroller. Interconnection of ADCs in daisy chain mode is illustrated in Fig. 2.9 and discussed further in 2.5.1. In the block diagram of Fig. 2.5, the data acquisition (DAQ_n) unit, with n = 1, 2, 3 and 4, is composed of two parts: (*i*) signal conditioning described in 2.4, and (*ii*) the blocks ADC1 and ADC2. The ADC1 and ADC2 blocks convert the weight and BCG signals to digital, respectively. The circuits in Fig. 2.3 and Fig. 2.6 are implemented on the same printed circuit board (PCB) shown in Fig. 2.7. This PCB constitutes a DAQ unit.

The circuit diagram in Fig. 2.6 provides details for the ADC1 and ADC2 connections. The ADC chips designated as U8 an U9 are the ADC1 and ADC2 in the block diagram of Fig. 2.5, respectively. Note that AINP1 and ANPI2 are the signals showing the analog outputs from the circuit of Fig. 2.3 that become inputs to the ADCs in the circuit of Fig. 2.6.

Low-voltage differential signaling (LVDS) drivers and receivers were installed between each ADC board to address ringing effects observed on the SPI signal. Prior to LVDS implementation, the ringing behavior (particularly of the clock) caused substantial bit errors during transmission. The circuit of Fig. 2.6 shows how DIN-DOUT pins of the ADCs (U8 and U9) are connected to the blocks labeled “IN” and “OUT” through LVDS drivers.

The "IN" and "OUT" blocks in the circuit of Fig. 2.6 represent RJ-45 connectors used for interconnection between communicating boards. RJ-45 connectors were used in the interface because they can be connected with easily-available Ethernet cables. The Ethernet cables, in turn, provide twisted pairs of wires and thus fulfill the differential requirement of LVDS communication.

Fig. 2.8 shows all the DAQs and the interconnections between them. It also shows how the signal from each load cell reaches each of those DAQs. The microcontroller (μC) block in Fig. 2.8 represents the microcontroller board that communicates with the first DAQ unit over SPI. The DAQ board interfaced with the microcontroller board uses the OUT block in the figure whereas its IN block is used to communicate with a previous DAQ board. The acquired data by the microcontroller is then transferred to a host PC (the PC block in this diagram) using the Universal Asynchronous Receiver/Transmitter (UART) interface of the MATLAB application residing on the PC.A detailed bill of materials for both circuits of Fig. 2.3 and Fig. 2.6 is provided in Table C.2 in Appendix C.

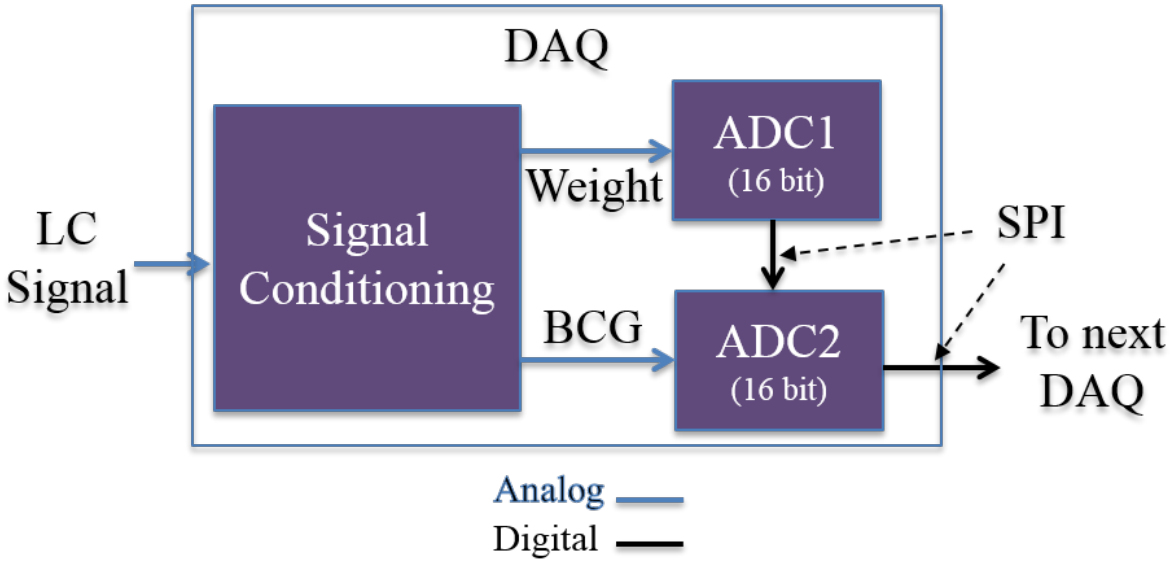

Figure 2.5: Board-level daisy chain block diagram of a single DAQ unit.

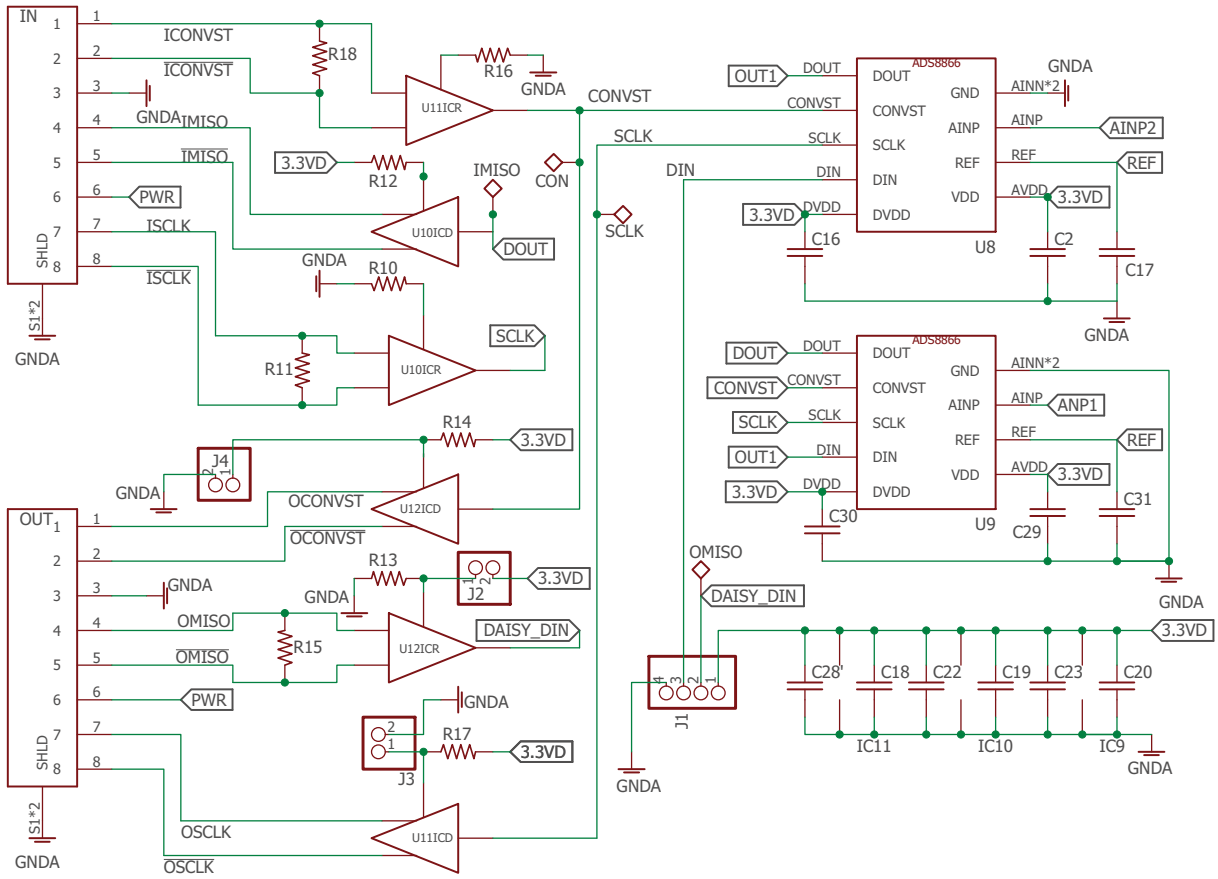

Figure 2.6: Circuit diagram for the ADC part of the Configuration I.

ADCs in daisy-chain connection

In this configuration, DAQ units are cascaded through digital input (DIN) and digital output (DOUT) interfaces of the ADCs. An ADC-level block diagram of this configuration is shown in Fig. 2.9. The conversion results from all the ADCs travel bit-by-bit through the entire chain until they reach to the first ADC which is interfaced with the microcontroller, the "Digital Host" block, in the diagram. The microcontroller receives the digital signal using the same SPI protocol used by the ADCs.

LVDS effects

We also tested this configuration with the distance between communicating devices reduced to the shortest possible distance, in order to see if LVDS was necessary in such a scenario.

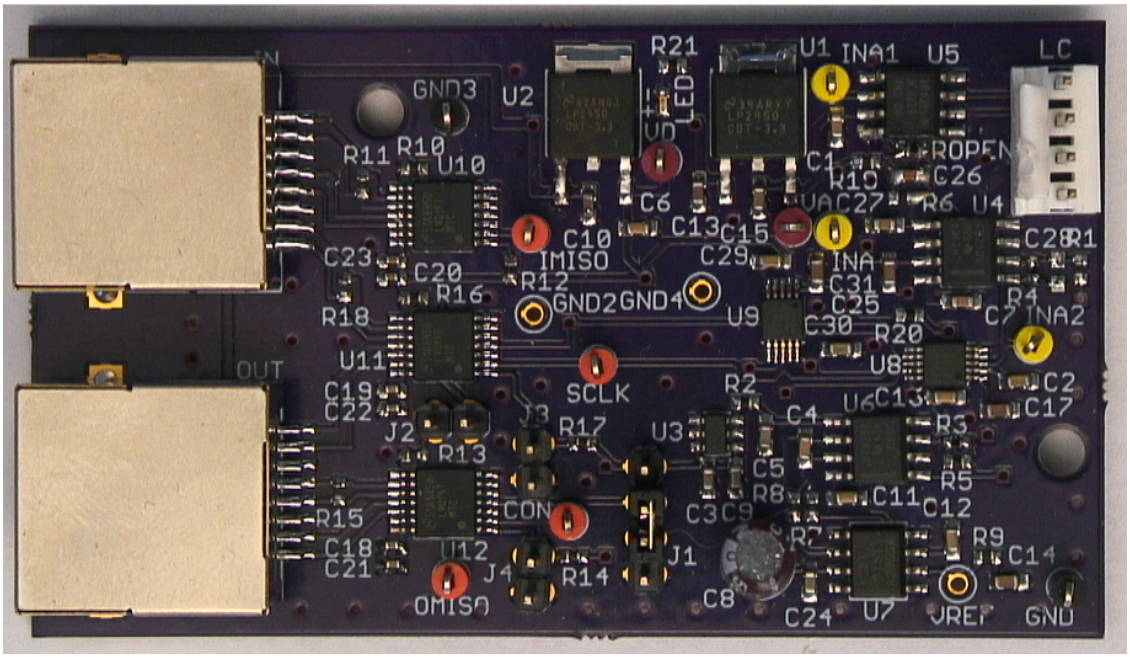

Figure 2.7: PCB implementation of the circuit diagrams of Fig. 2.3 and Fig. 2.6 representing a single board of the four boards used in Configuration I.

2.5.2 Configuration II: NI-DAQ

This configuration, illustrated in Fig. 2.10, implements the second scenario. That is, signal conditioning is done near each load cell, whereas the digitization is done at a central point (a

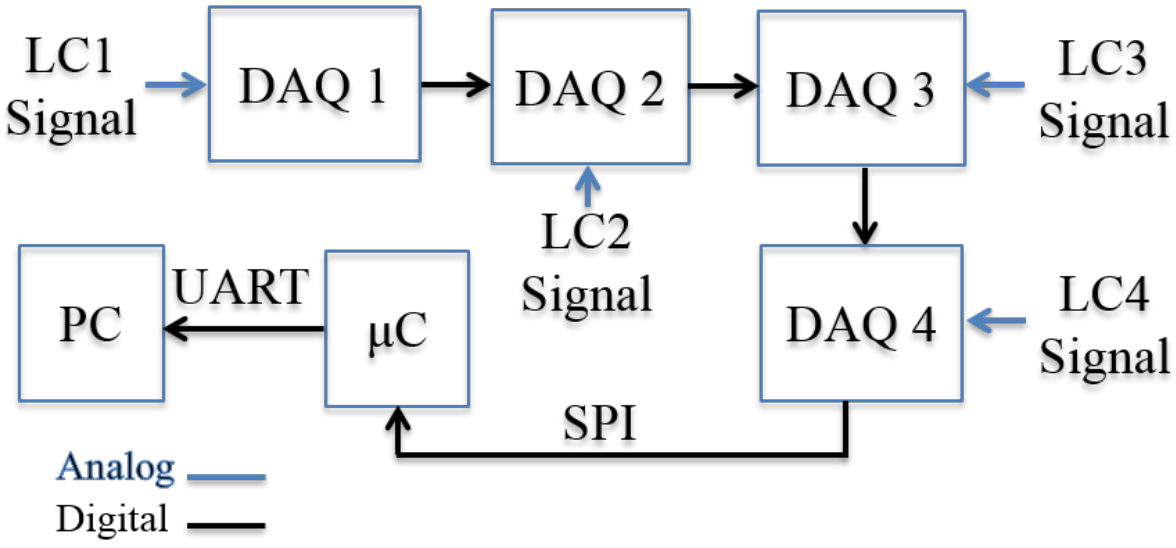

Figure 2.8: Board level daisy chain block diagram of a single data acquisition (DAQ) unit.

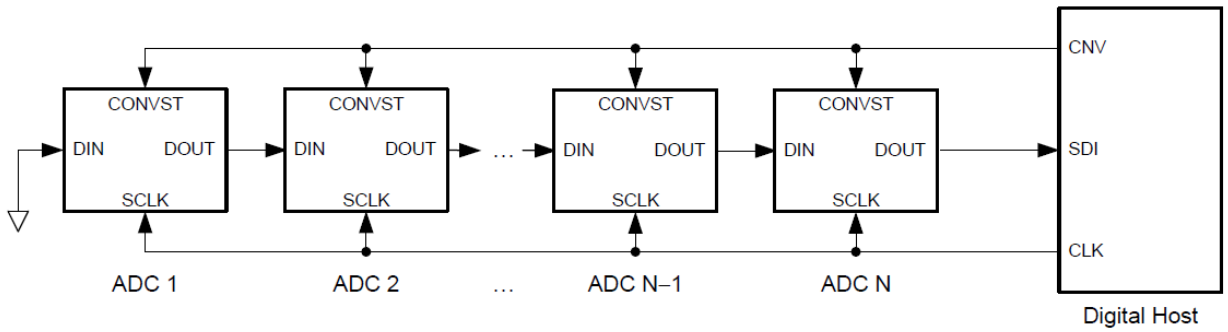

Figure 2.9: ADC level daisy chain block diagram.

C series National Instruments 9220 analog module, called the NI-DAQ from here on). This point is intended to be equidistant to each signal conditioning circuit. In this scenario, the amplified analog signal has to travel a significant distance before it is converted to a digital signal in the data acquisition unit. The NI-DAQ is then responsible to convert the received signal to digital and send it out over Ethernet or WiFi-based packets to the host PC. The host PC then collects the received data through a virtual instrument interface provided by LabVIEW.

The block named Signal Conditioning Board in the diagram of Fig. 2.10 is identical to the signal conditioning part of Configuration I and is realized with the same circuit of Fig. 2.3. The contrast is however in the way the amplified signals ANP1 and ANP2 of the circuit of the Fig. 2.3 are connected to the ADC. In Configuration II, the mentioned signals are connected through twisted pairs of wires to the NI-based ADC module whereas in Configuration I they were connected to the daisy chain ADC through the traces of the PCB where both the signal conditioning and the ADC were implemented. Here, the signal conditioning board is on a separate PCB (Fig. 2.4) and the NI-based ADC module is separate.

The 3xSig. Cond. Brd block represents three other copies of the Signal Conditioning Board in the diagram of Fig. 2.10. Two ADC channels of the NI-DAQ are connected to each Signal Conditioning Board. Thus, a total of eight ADC channels are occupied by these boards.

2.5.3 Configuration III: 24-bit ADC

This configuration implements the third scenario, i.e., avoiding any signal conditioning to the sensor signal. Instead, the sensor output is digitized immediately with a higher resolution ADC and transmitted in that digital form to a central location for acquisition. This configuration offers the possibility of avoiding the noise due to the amplification in the signal conditioning modules, as well as reducing component count and thus cost and complexity.

In this test, a high resolution, 24-bit ADC was utilized since those small BCG peaks on the output of the load cells cannot be captured with a 16-bit ADC without prior amplification.

We were also interested to test if the existence of a signal conditioning circuit with a 24-bit ADC would improve the overall performance. Thus two scenarios are presented in Table 2.1: (*i*) Conf-III: 24-bit ADC with signal conditioning, (*ii*) Conf-III: 24-bit ADC without signal conditioning. The signal conditioning board of configuration II was used to test the scenario (*i*). Fig. 2.11 illustrates this configuration. The dotted lines of the Signal Conditioning block signify that the configuration was tested with and without the block.

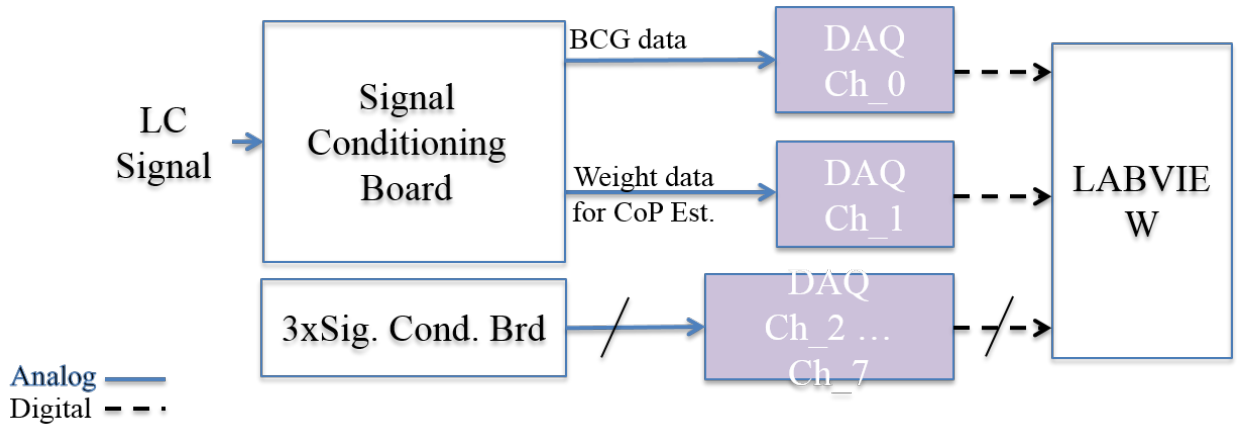

Figure 2.10: Block diagram of the signal conditioning and data acquisition in configuration II.

2.6 Sine wave force tests

In order to quantify the effects of different configurations discussed above, a sine wave force with a known frequency of 5 Hz was applied to a test platform under which a single load cell was positioned. The force was provided by a speaker that was fed from an audio amplifier. The signal to the audio amplifier was provided from a signal generator. More details on this setup are provided in Chapter 3 where effects of the load cells on the BCG are evaluated. All tests were performed with the FX1901 from TE Connectivity.

2.6.1 Performance metric

Signal to noise ratio (SNR) was used as the performance metric, or the quantitative measure of the impact of the three DAQ configurations. The final resulting signal stored in the PC was compared with a "carrier" signal when calculating the SNR. The carrier signal in this case is a built-in utility of the MATLAB function "snr" when used with the syntax snr(X), X being the signal of interest. This function computes the SNR of the signal X over a periodogram

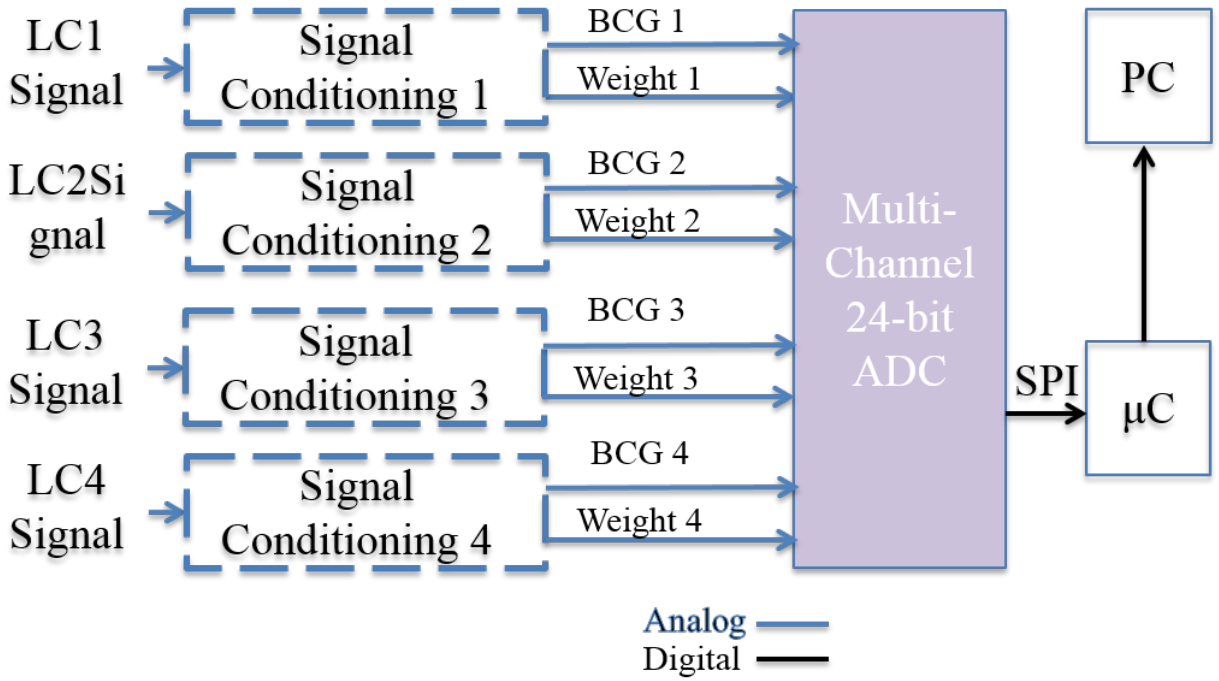

Figure 2.11: Block diagram for signal conditioning and data acquisition configuration III.

of the same length as the length of X vector using a Kaiser window, while excluding the power of the first six harmonics including the fundamental. The SNR measured has units of dBc, indicating that the comparison is done in reference to a carrier. Since the test signal is a sine wave, we believe this is a valid metric.

2.7 Results

The comparison results, given as SNR in dBc, are presented in Table 2.1. In the table, Conf-I through Conf-III refers to the three configurations elaborated in 2.5.1 to 2.5.3, respectively. The term "Factory" indicates the original wire length of the load cell as delivered from the company. PCB refers to the short traces of the PCB. N-A, i.e., Not Available, means that the distance was not present which was the case with Configuration III when no signal conditioning was in place between the load cell and the ADC. The term "No LVDS" in the table refers to a test scenario where LVDS was not used in the configuration I, as pointed out in 2.5.1.

The term "LL" stands for Long Length and refers to the addition of an extra wire of length 8 feet to emulate the unavoidable distance introduced by the long edge of the bed. Also, LL can be used to estimate the effects of long wires between the bed and the PC recording the data. "ML" stands for Minimal Length and refers to the shortest interconnecting wires between load cells and boards or between two boards if needed. In the former case, it is the length of the load cell wires after cutting. The length of ML was approximately 2 inches.

2.8 Discussion

Based on the numbers in Table 2.1, Configuration I with an SNR of 26.74 dBc is the best-performing configuration. Other advantages that this configuration offers are simultaneous conversion of the signal from all sensors, conversion to digital signal near the sensor thus facilitating less noisy signal acquisition, scalability to add new sensors, and low cost compared to Configuration II. The disadvantages are increased complexity due to LVDS circuitry and

Table 2.1: SNR comparison of different configurations and different distances between the sensors (LC), signal conditioning circuits (Cond.) and the ADCs. ML = 2", LL = 8'

DAQ Configuration	Wire Length LC to Cond.	Wire Length Cond. to ADC	SNR (dB)
Conf-I	ML	PCB	25.07
	Factory	PCB	26.74
	Factory + LL	PCB	20.61
Conf-I: No LVDS	Factory	ML	15.60
	Factory	LL + ML	7.80
Conf-II	Factory	ML	20.50
	Factory	LL + ML	21.60
Conf-III	ML	LL	26.14
	LL + ML	PCB	23.56
	ML	PCB	25.30
Conf-III: No Conditioning	ML	N-A	13.90
	LL + ML	N-A	12.47

less convenient interfacing with the host PC. The second preferred configuration would be Configuration III with 26.14 dBc SNR. The advantages of this configuration are higher resolution (up to 24 bits), centralized digitization while allowing signal conditioning near the load cell, reduced complexity and the lowest cost. The only disadvantage of this configuration at this point is the interfacing challenge with the host PC, same as in the case of Configuration I. Configuration II with a maximum SNR of 21.60 dBc presents the third performance. The advantage of this configuration is the readily available interface with Ethernet or WiFi offered by the NI module. The disadvantage of this configuration, besides the SNR, is the high cost of the C series NI 9220 analog module.

The challenge of interfacing with the host PC is not yet addressed for Configurations I and III. As a result, use of these configurations depends on the availability of a running host PC in the vicinity of the bed to establish a serial interface between the microcontroller involved and the MATLAB that runs on the host PC. While an alternative of a Raspberry Pi unit is under investigation, we conclude that the mentioned configurations are not yet ready for a long-term remote-running scenario intended for long-term health monitoring. Given the mentioned limitation for Configurations I and III, this dissertation has nearly exclusively used Configuration II. The only exception is that the sine wave force tests for load cell

comparison performed in Chapter 3 are done using Configuration I. The reason was that the tests were short experiments; the end-interfacing with MATLAB was established and the configuration provides a high SNR.

The multi-channel ADCs in Configurations II and III implement a multiplexer to read from all the channels. This multiplexing scheme introduces a delay in sampling from all the sensors and a simultaneous read is not possible, in contrast with Configuration I. However, in low frequency applications such as ours and with sampling rates of 250Hz and above, the delay between sampling instances can likely be ignored.

The experiment does show several clear results. As expected, long distances between the sensor and the signal conditioning circuit results in adverse outcomes. Further, LVDS is necessary for the daisy-chain configuration. This confirms the necessity of these drivers in long distance SPI communications as well as in short distance communication. Finally, both Configurations II and III present better results with longer wires between the signal conditioning board and the ADC. The reason for the phenomenon is not clear, and may actually represent electro-magnetic coupling between our signal source and the long wires rather than a true improvement in signal quality.

2.9 Conclusion and future work

The hardware for BCG and COP detection and recording was introduced. Three different signal conditioning and data acquisition configurations were presented and their effects on the acquired signal were quantified. While a configuration with the least adverse effects on the signal was identified, its practical use in a home setting is not yet possible. Therefore, interfacing solutions with the host PC needs to be sought as a future effort in the form of either TCP/IP protocols or a web-based cloud protocol.

Chapter 3

Effects of sensor selection on signal quality

3.1 Introduction

Multiple studies have used bed-based BCGs acquired with different types of pressure or force sensors. E.g., Mendez et al. [115] and Jung et al. [88] used electromechanical films (EMFi's) and polyvinylidene fluoride (PVDF) films, respectively, to acquire nighttime BCGs. Load cells have also played a role in BCG acquisition [91, 116]. However, the literature in BCG detection has contained limited information regarding solutions to hardware challenges encountered in sensor selection. Hardware design information in such publications often remain limited to system block diagrams and high-level circuit descriptions [116]. Low-level challenges encountered when building these BCG acquisition systems are not often addressed. These details and lessons learned play an important role in BCG signal optimization and the efficient use of design time, especially for researchers that are new to this field and rely on published literature for guidance. This chapter addresses the effects of load cell selection and its associated impacts on the BCG quality.

Challenges include poor signal quality and intermittent signal behavior between load cells under identical conditions. Load cells with nearly identical specifications can still produce

BCGs of very different quality. Strain gauges are notoriously noisy, and manufacturing techniques vary, so one can save time and effort by performing comparative analyses on what appear to be similar load cell designs prior to adopting a given model for larger scale deployment. Load cells with higher capacities are essentially manufactured for heavier duty applications, and such applications are more tolerant to small errors in specifications. On the contrary, in applications such as ballistocardiography, the summative weight of the subject and the bed drives the overall weight specification for the load cell, forcing the relatively small BCG itself to coincide with the noisiest operational range of the load cell. Load cell specifications, though, are not reported to that level of relative precision. Empirical testing is needed.

This chapter provides an objective rationale for selecting a load cell in use for this dissertation by comparing performance of four load cells readily available in the lab or in the retail market. Therefore, this chapter considers four brands of load cells under similar testing circumstances, addressing their responses to different low-magnitude known test forces. These test forces are: (*i*) small vibrations due to an eccentric rotating mass (ERM), (*ii*) impulsive force, and (*iii*) sinusoidal force. The latter two force tests are applied using a speaker. Quantitative performance comparisons are presented for the load cells in question. In addition, graphical performance comparisons are presented.

3.2 Methods

3.2.1 Informal Background

Based on a prior student's work, we initially planned on using the LCM 302 load cell. Unfortunately for us, we performed only limited initial testing (observing the differential voltage on the output terminals of the load cell in response to a constant applied weight, and recording a few responses to impulsive inputs). The responses to these initial tests led us to believe that the LCM 302 was suitable for our application. However, our circuit (using said load cell) kept failing to detect BCG.

Different signal conditioning circuit iterations were tested to rule out flaws in the circuit design. Around this time, we also began the sine wave tests as discussed in Chapter 2. Later, a different load cell was procured and tested.

A slight improvement in the obtained signal from the new load cell encouraged further investigation in this direction. Therefore, two more load cells were considered for a comparative study among a total of four similar button-type load cells. This step assisted us in selecting a load cell with good signal quality. The following tests were conducted to quantify the effects of each load cell on the detected signals. In all subsequent tests, the differences in the sensitivity of the load cells were addressed by adjusting the gain of the instrumentation amplifier to which each load cell was connected.

3.2.2 Sensitivity tests

Based on the initial responses of the load cells to the BCG and inability of one particular load cell (LCM 302) to detect it, we decided to verify the sensitivity of the load cells to the applied forces quantitatively. Therefore, we evaluated the responses of the load cells to an applied static weight under a constant DC voltage.

The sensitivity of each load cell was re-evaluated by applying a constant force of 104.5 N (23 lbs) while recording the difference in the voltage on their output terminals due to the applied force. The voltage measurements were carried out using an Agilent 34401A multimeter. The sensitivity was then calculated using Eq. 3.1. The calculated values are summarized in Table 3.4 where they are compared with the nominal sensitivities as listed in their data sheets.

$$Output\ Voltage\ Sensitivity = \frac{\delta v}{f * V_t} * f_{MAX}\ (mv/V) \tag{3.1}$$

Where δv is defined in Eq. 3.2, f if the applied constant force, V_t is the excitation voltage applied on the input terminals of each load cell, and f_{MAX} is the maximum capacity of each

load cell.

$$\delta v = v_{o_L} - v_{o_{NL}} \tag{3.2}$$

v_{o_L} is the voltage measured at the differential output terminals of each load cell under constant load. $v_{o_{NL}}$ is the voltage measured at the differential output terminals of each load cell at no load.

During this experiment an allowable gain was also determined for the instrumentation amplifier. The gain was set such that it would provide maximum amplification to the applied signal without letting the output of the instrumentation amplifier rail to the supply voltage. In addition, values for the gain resistor of the instrumentation amplifier were estimated to address various body weight ranges expected to occupy the bed.

3.2.3 Load cells' response to small vibrations

An eccentric rotating mass (ERM) was used to apply mechanical vibrations at ten different frequencies: 52, 83, 111, 139, 151, 185, 205, 227, 238 and 263 Hz. The ERM was mounted on the bed and thus its vibrations were coupled to the load cells. The ERMs used in this test come with the following drawbacks:

1. The frequency of vibration and amplitude of vibration are controlled by the same voltage input. Although we used normalization to offset this issue, some issues may remain.

2. They do not allow testing of the load cells in the primary frequency range of BCG since they do not rotate at very low frequency ranges of below 0.5 Hz.

3. The speed varies by a few Hz around the set point, which makes it difficult to distinguish between the effects of the load cell and the ERM.

3.2.4 Variable force source description

Due to the limitations introduced by the ERMs in the small vibration tests described in 3.2.3, it was necessary to seek an alternative testing approach. For that purpose, a variable force controlling and recording system was built. This system controls the characteristics of the exerted force on the bed and records its response from the load cells.

This system consists of a signal generator, an audio amplifier and a speaker. The signal coming from the signal generator is amplified by the audio amplifier and is supplied to the speaker. The speaker transduces the received signal into a force which is transmitted to the bed through a coupling between the speaker and the bed. Subsequently, the transmitted force is detected by the load cells. At this point, a differential voltage can be measured at the output terminals of the load cells that corresponds to the applied varying force. The measured differential voltage is eventually stored in a PC for further analysis using the DAQ configuration I as described in 2.5.1. This process is illustrated in the block diagram of Fig. 3.1.

The PC in the figure runs a MATLAB session that accomplishes two tasks. The first task is to provide instructions to the signal generator to supply desired signals. The instructions included the commands to turn on or off the output of the signal generator as well. The second task is to record the data received from the microcontroller over the UART interface

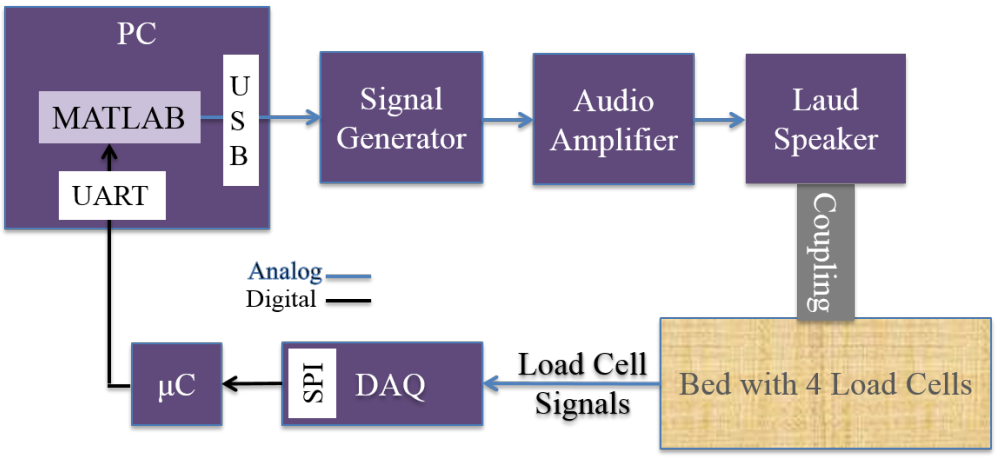

Figure 3.1: The block diagram of force source controlling and recording system (Audio amplifier courtesy of Garrett Peterson).

of the same MATLAB session.

The picture in Fig. 3.2 provides a snapshot of the setup. A structure that supports an audio speaker as a controllable varying-force source is also shown in the picture. The structure allows the speaker to be mounted on the bed and maintain a proper coupling with it. The force source, i.e. the speaker, was positioned in the middle (center) of the bed in order to keep the distance between the force source and the load cells equal. This system facilitates variable force tests where the variable force is of two natures: (i) impulsive force, and (ii) sinusoidal force as elaborated in 3.2.6 and 3.2.7 respectively.

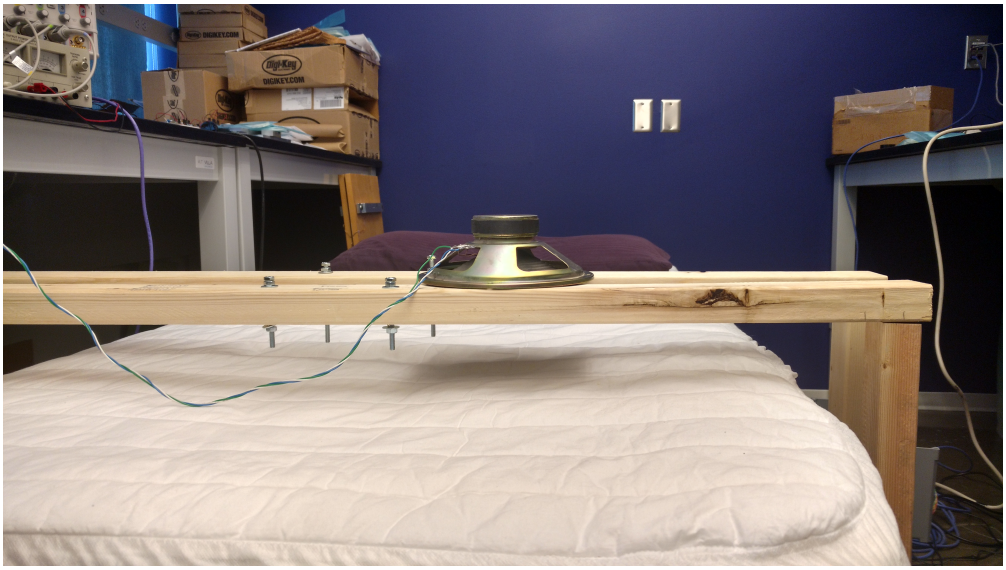

Figure 3.2: Snapshot of force source support setup

3.2.5 Weight arrangements

Since the BCG may be coming from participants with different weights, a combination of different weights on the bed was examined. In addition, the COP of a sleeping person may change during the course of a data recording session. In order to account for a possible subset of points from the trajectory of the COP, the weights were spread over the bed with different arrangements. Fig. 3.3 shows the spread of the weights as scheduled according to Tables 3.1 and 3.2. The weight arrangements described in Table 3.1 was used for impulsive force test experiments. Likewise, the weight arrangements described in Table 3.2 was used

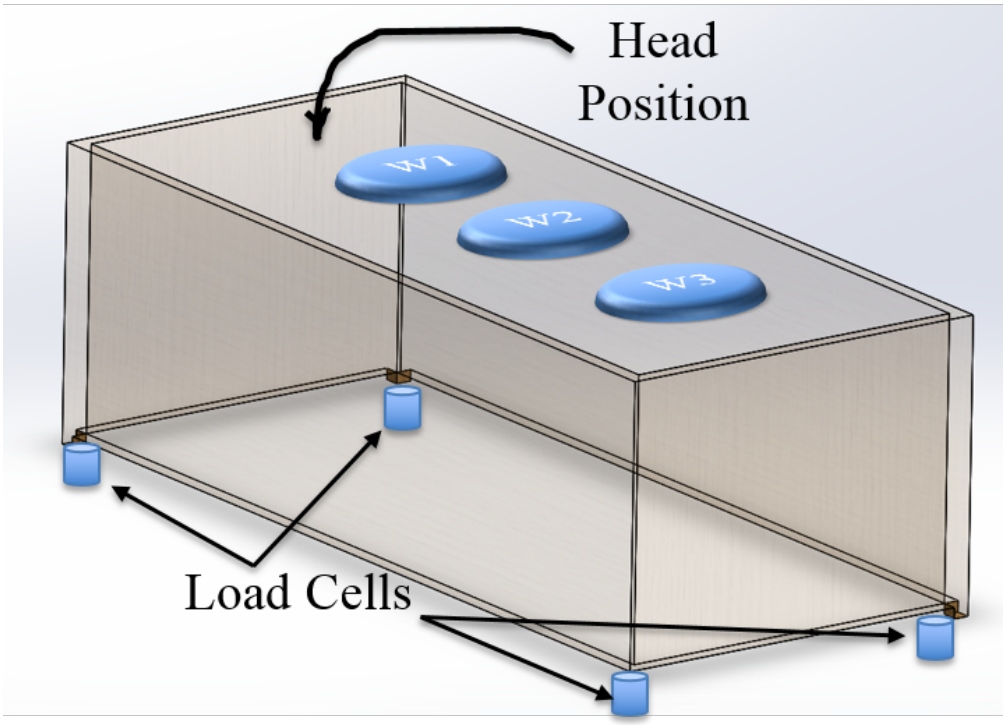

Figure 3.3: Bed and the weights spread over it (3D representation of bed courtesy of Charles Carlson).

for sine wave force test experiments.

Table 3.1: Weight schedule for impulsive force test

Weight Configuration #	Weight W1 (lb)	Weight W2 (lb)	Weight W3 (lb)
1	80	70	80
2	80	45	80
3	80	70	55
4	80	45	45
5	80	70	35
6	80	45	35
7	80	45	60
8	80	60	45
9	80	35	70
10	80	35	45
11	80	35	25

3.2.6 Impulsive force test

The goal in this test is to observe the overall load cell responses to a wide range of frequencies. In order to create such an impulsive force, the signal generator was first set in the DC output mode while its output was kept turned off. A voltage level of 5V was set for the output. Then, once everything was ready and recording was ongoing, a pair of subsequent commands to turn on and immediately turn off the output of the signal generator was sent by MATLAB to the signal generator. This way, it was possible to emulate an impulse-like signal with relatively small width and an amplitude of 5V. Based on our observations from the time-domain impulsive force responses of the load cells, the average width was 170 ms. In theory, the frequency content of an impulse signal is infinite, allowing measurement of the response of the load cells to an infinite range of frequencies. However, an impulse force with zero width that results in infinite frequency bandwidth is not practically possible. As a result, this test is limited to frequency ranges with a maximum bandwidth ($maxBW$). In addition, the sampling frequency (sf) is another limit to the range of frequency for which a response can be measured. With $maxBW$ defined in Eq. 3.3, the maximum frequency range over which the load cell responses can be measured is defined in Eq. 3.4.

$$maxBW = \frac{1}{Width\ of\ the\ impulse\ force} \tag{3.3}$$

Table 3.2: Weight schedule for sine wave force test

Weight Configuration #	Weight W1 (lb)	Weight W2 (lb)	Weight W3 (lb)
1	35	45	35
2	105	45	80
3	80	45	80
4	25	45	25

$$Maximum\ Frequency\ Range = \min\left(maxBW, \frac{sf}{2}\right) \tag{3.4}$$

Using Eq. 3.3, the average observed width of 170 ms translates to approximately 58 Hz. Since the sampling frequency was set to 250 Hz during these tests, then according to Eq. 3.4, the maximum frequency range will be 58 Hz. This range is just above the bandwidth of interest for BCG (0.05 to 35 Hz) [] so an overall response of the load cells to the BCG bandwidth can be observed.

Conducting this test produced time-domain responses for each weight schedule scenario as listed in Table 3.1 and representative plots are shown in Fig. 3.4 and Fig. 3.5. In addition, frequency-domain responses were produced for the mentioned weight schedules. The average of the frequency responses over the number of weight schedules is shown in Fig. 3.6.

3.2.7 Sinusoidal force test

In addition to the impulsive force test, we also tested load cell responses to some individual known frequencies. In this test, the weight combinations were reduced to only four experiments and the schedule was also changed as most of the weights had to be returned to their lender. The schedule for this weight arrangement is provided in Table 3.2.

Sine wave-forces with different frequencies were applied to the bed to address the bandwidth of the BCG. Table 3.3 provides the frequencies and related resolutions for which sine waves were generated. In order to capture the behavior of the conditioning circuit, we increased the resolution of test frequencies near the corner frequencies of our hardware filters (0.05 to 35 Hz). Sample outputs due to 1 and 15 Hz sine waves for weight arrangement # 3 are depicted in Fig. 3.7 and Fig. 3.8 respectively in the results section.

In order to provide an overview of the load cell responses, SNR of the processed load cell output was calculated for each frequency in the same manner described in 2.6.1. A plot depicting the SNR of processed load cell outputs averaged over the different weight

Table 3.3: Test frequencies and their related resolution.

Frequency Range #	Frequency 1 (Hz)	Frequency 2 (Hz)	Resolution (Hz)
1	0.1	2	0.05
2	2	5	0.1
3	5	23	1
4	23	26	0.1
5	26	45	1

arrangements of Table 3.2 is provided in Fig. 3.11 for the four load cells.

3.3 Results

3.3.1 Sensitivity test results

Table 3.4 compares the measured sensitivities and sensitivities published in their related data sheets. A column for their prices is also provided.

The outcomes of this test and the small vibrations tests with ERMs were presented in a poster in 2016 annual international conference of IEEE Engineering in Medicine and Biology Society (EMBC).

3.3.2 Impulsive force test results

The plots in Fig. 3.4 and Fig. 3.5 present impulsive force response under two different weight configurations. Fig. 3.4 shows impulsive force response when weight arrangement #1 was on the bed whereas Fig. 3.5 shows the response produced when weight arrangement #4 was

Table 3.4: Sensitivity of load cells and other related information.

Load Cell	**Distributor**	**Price**	**Measured Sensitivity**	**Published Sensitivity**	**Max Load**
TAS606	Karlsson	$57	2mV/V	2mV/V	1.96 KN
LCM302	Omega	$315	<1mV/V	2mV/V	2.00 KN
FC2311	TE Connectivity	$131	20mV/V	20mV/V	1.11 KN (250 lb)
FX1901	TE Connectivity	$31	20mV/V	20mV/V	0.89 KN (200 lb)

on the bed.

Fig. 3.6 shows the frequency responses of the load cells to an impulsive force. Each load cell response is averaged over all weight arrangements described in Table 3.1.

3.3.3 Sinusoidal force test results

Sample time-domain load cell responses to sine waves of 1 Hz and 15Hz is shown in Fig. 3.7 and Fig. 3.8 respectively. The responses are produced under the weight arrangement #3 of Table 3.2. Please note the difference in LCM302 load cell response in both scenarios.
Fig. 3.9 and Fig. 3.10 show the corresponding frequency responses of the load cells to 1 Hz and 15 Hz sine waves, respectively, under the same weight arrangement. Again, please note the differences in magnitude of the responses in both cases, in particular for the LCM302.
Fig. 3.11 shows the SNR of the sine wave outputs of the load cells at the tested frequencies

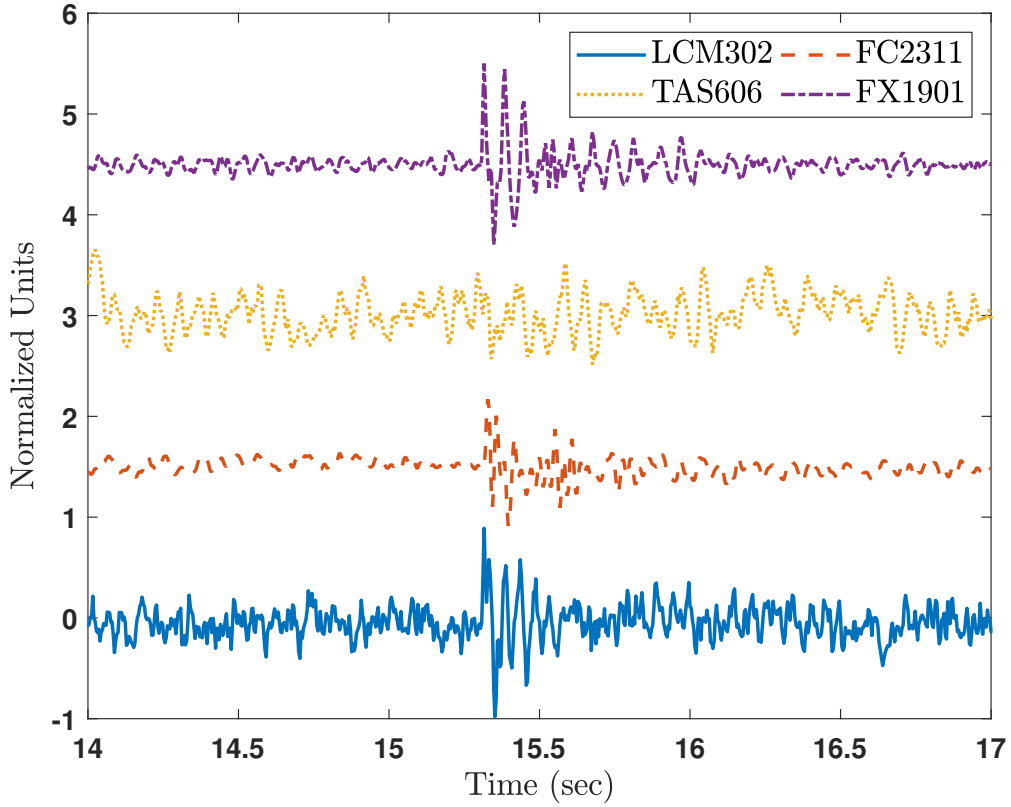

Figure 3.4: Load cell response to impulsive force under the weight arrangement # 1 of Table 3.1

in Table 3.3. The SNR values are averaged over the four weight arrangements described in Table 3.2.

3.4 Discussions

3.4.1 Impulse response

Fig. 3.4 and Fig. 3.5 show that impulse responses were changing with the different weight arrangements. This is likely reflecting the fact that resonance of the bed-mass system changes as we change the weights. Therefore, the varying weights of different users could be expected to have effects on the obtained signal. Also, the varying amplitudes of the impulse responses in Fig. 3.4 and Fig. 3.5 can be related to varying COP due to changes in weight combinations. Also, from the averaged frequency response of the impulsive force test as in Fig. 3.6, it can

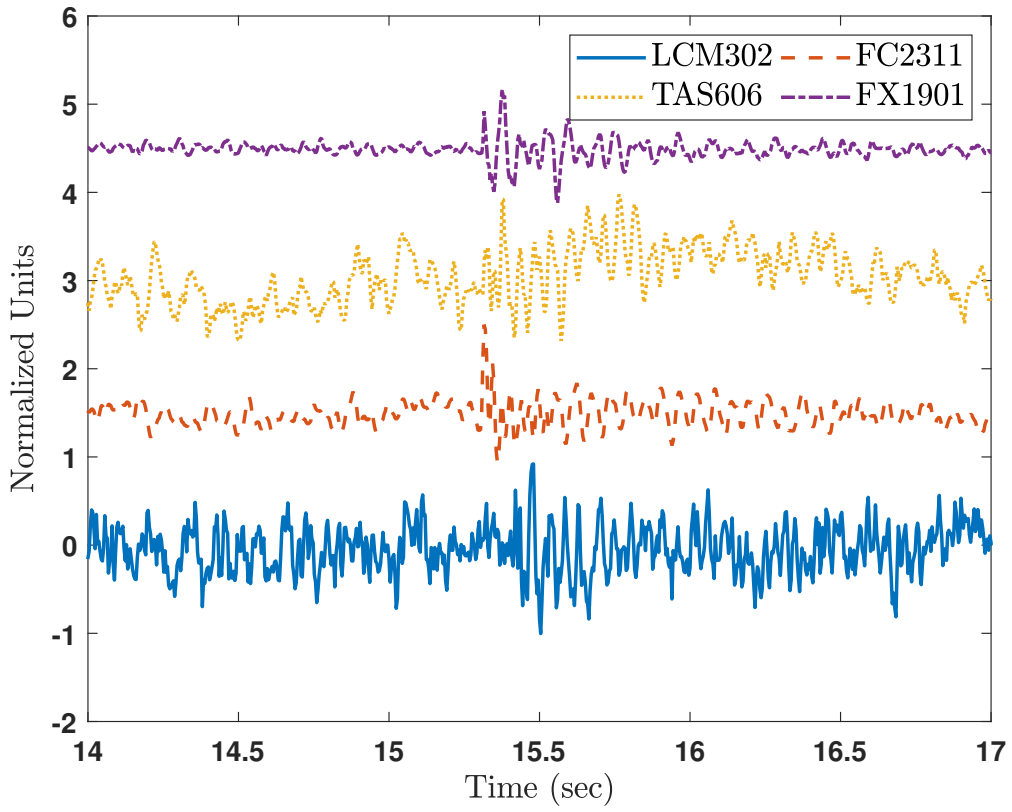

Figure 3.5: Load cell response to impulsive force under the weight arrangement # 4 of Table 3.1

be seen that LCM 302 presents a noisier signal in general.

3.4.2 Sine wave response

From the sine wave responses, one important conclusion is that the LCM302 load cell performs well only at around 15Hz, whereas its performance degrades severely at frequencies above or below 15 Hz. This behaviour is evident in both time domain and frequency domain responses. Therefore, the LCM302 is not a suitable candidate for BCG applications.

Comparing the curves in Fig. 3.11, it is easy to rank the FX1901 as the best performing load cell followed by the FC2311. In our estimation, TAS606 could be considered for BCG applications, but performs below the others. Although the FX1901 and FC2311 have similar SNRs in the frequency range of 0.1 to 16 Hz, the FX1901 has better performance for frequencies above 16 Hz. In addition, the FX1901 is the lowest priced load cell we tested.

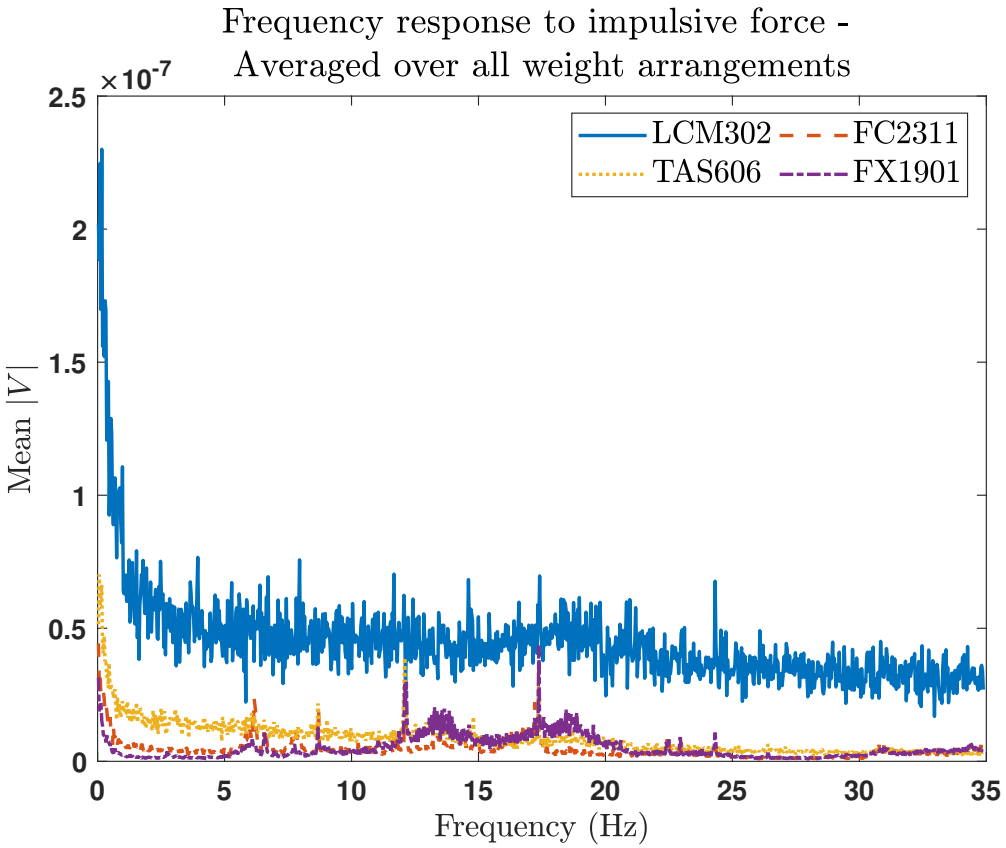

Figure 3.6: Frequency response to impulsive force averaged over all weight arrangements of Table 3.1

Therefore, the candidate load cell for our subsequent studies is FX1901.

3.4.3 Limitations

The bed utilized for this work [23–27] does not allow multiple load cells to be placed simultaneously under the same corner of the bed. In addition, setting the force source in the middle of the bed does not guarantee equal distribution of the force over all the four load cells. On the other hand, using a single corner of the bed while switching the load cells would result in different force-to-platform coupling effects every time a new load cell is placed for test. Thus, a trade-off was made. We had to decide between two settings: (i) keep the force-to-platform coupling constant, and (ii) minimize the distance between the force source and the load cell under test. In the case of (i), the four load cells are positioned beneath the posts of the bed at its four corners and the force source is in the middle of the bed (here we also tentatively

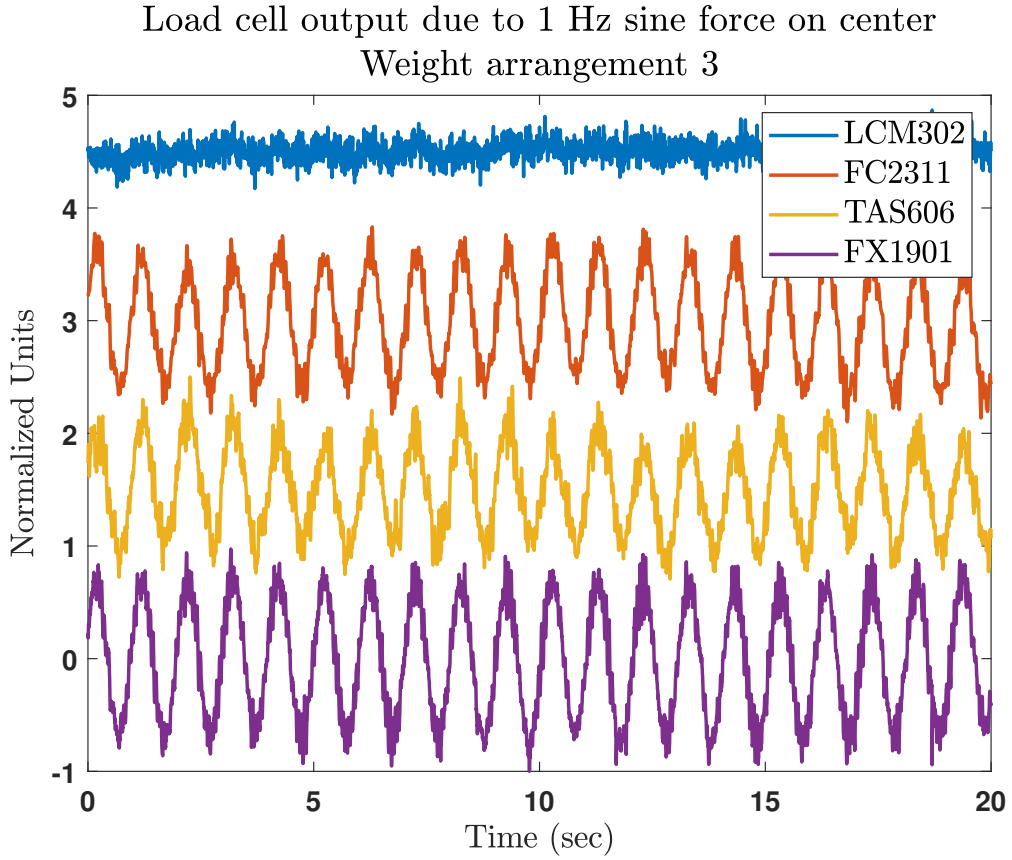

Figure 3.7: Load cell responses to a 1 Hz sine wave force under weight arrangement # 3

assume that the force is distributed equally on four load cells which might not be the case). In the case of (ii), the tests are performed on each load cell one at a time. However, this results in introducing variable force-to-platform effects. We picked (i).

Another limitation is the estimation of the range of frequencies provided by the impulsive force. Since we are measuring the width of the pulse on the output of the load cell, it is not a representative of the actual applied impulsive force. On the other hand, the sine-wave force test resulted in poor results when below 1 Hz. This was due to the audio amplifier and speaker effects on the amplitude of the test signal with those frequencies.

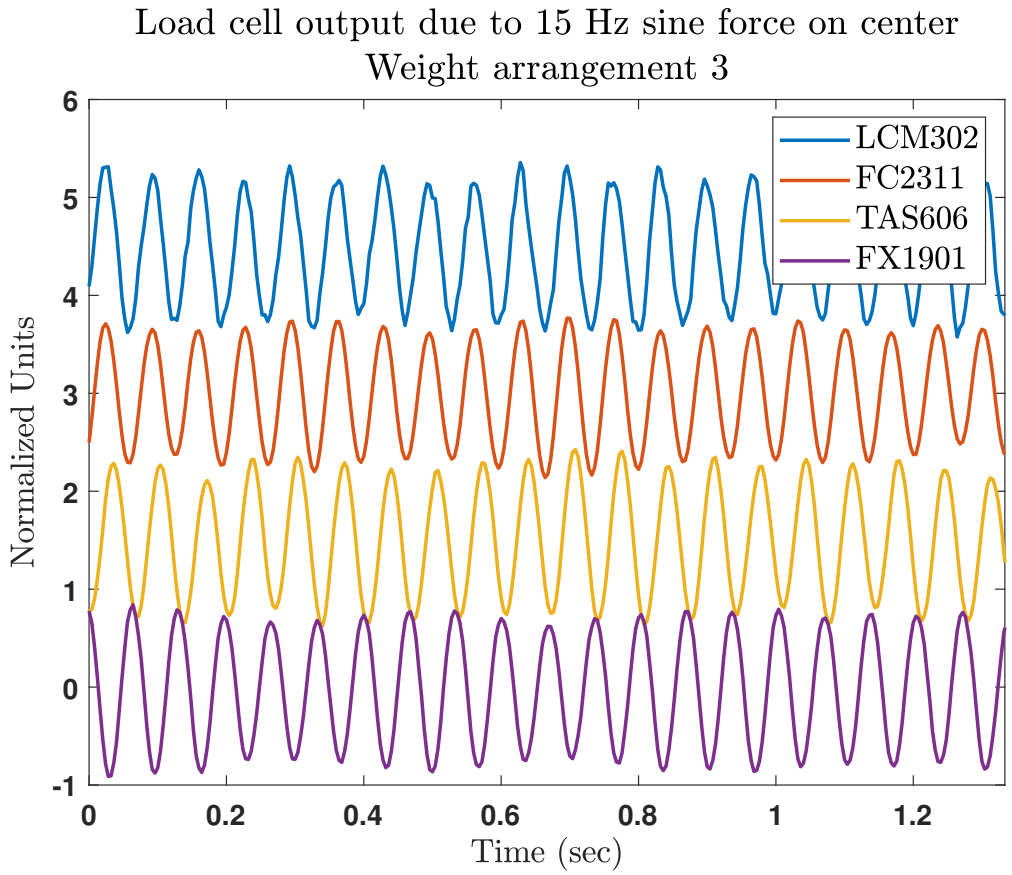

Figure 3.8: Load cell responses to a 15 Hz sine wave force under weight arrangement # 3

3.5 Conclusion

Bed-based load cells can provide effective means to acquire nighttime BCGs. Load cell selection and testing are important when designing such circuitry. Even though load cell specifications may appear nearly identical between manufacturers, it is crucial to test the performance of these sensors and choose the one that provides optimal signal quality. Most load cells are not designed for the purpose of acquiring such small signals relative to such large signal baselines, and may have undesirable noise or frequency characteristics. While the load cells used are not perfectly identical in sensitivity and range, the observed differences in their detected signal are much larger than would be expected from their specifications.

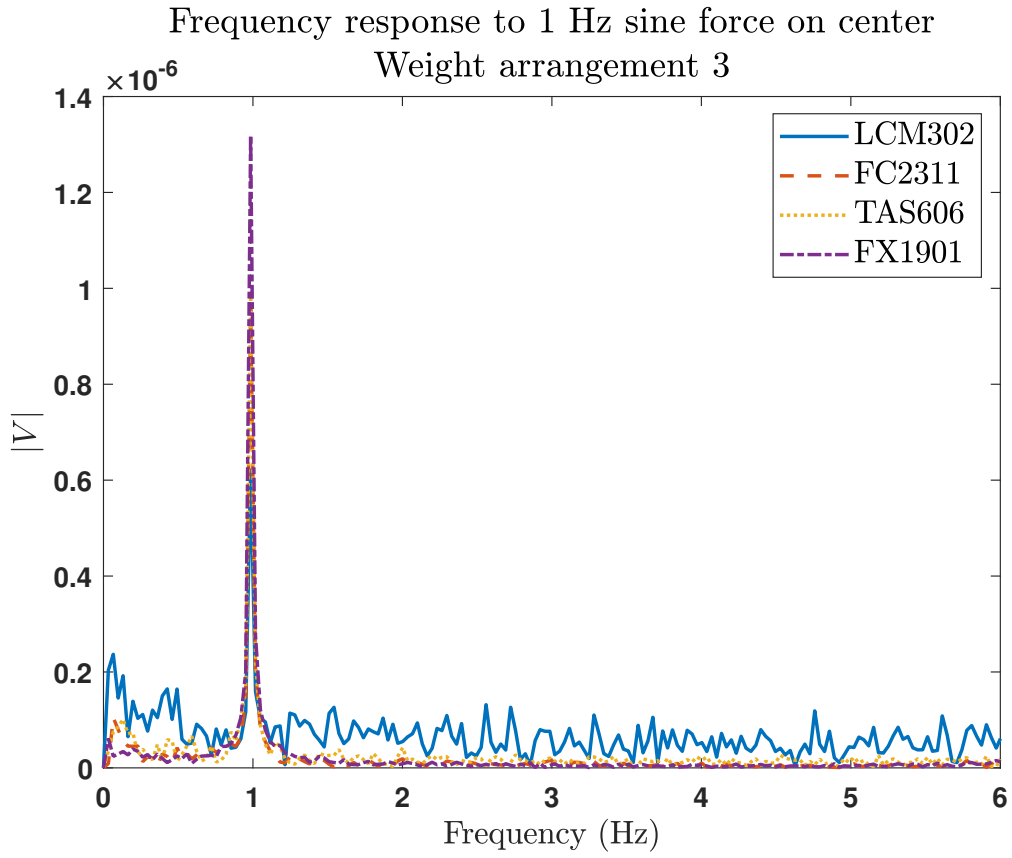

Figure 3.9: Load cell frequency responses to a 1 Hz sine wave force under weight arrangement # 3

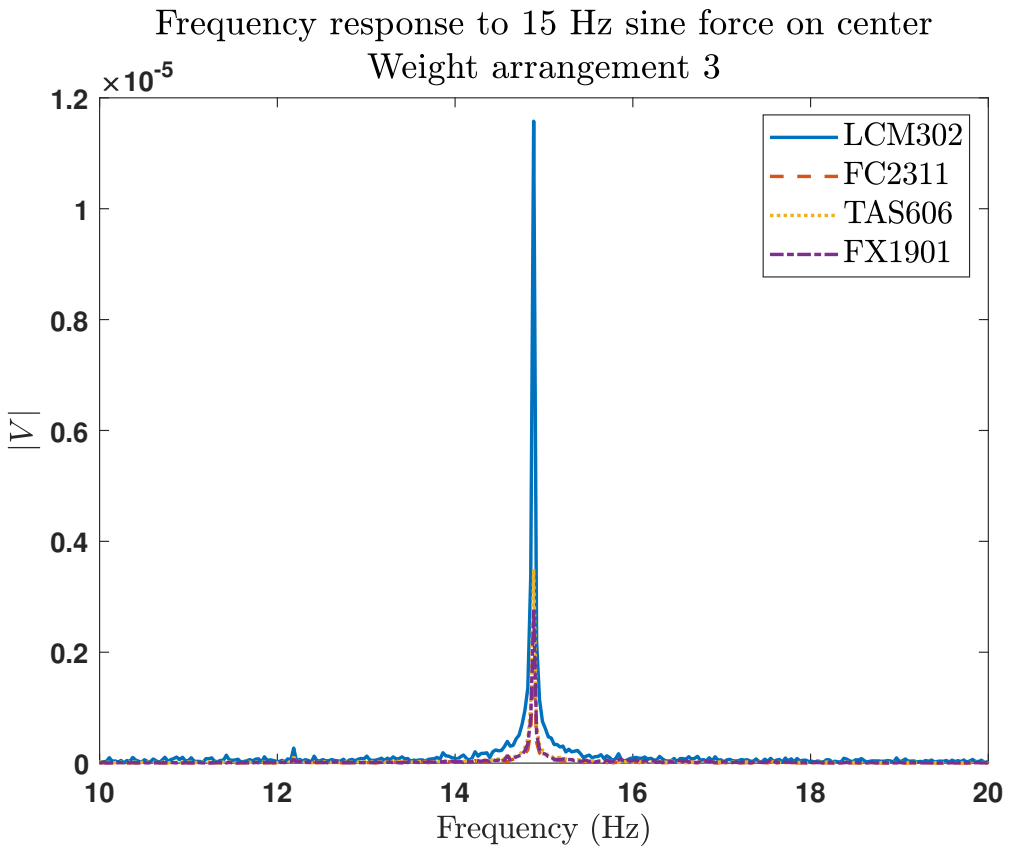

Figure 3.10: Load cell frequency responses to a 15 Hz sine wave force under weight arrangement # 3

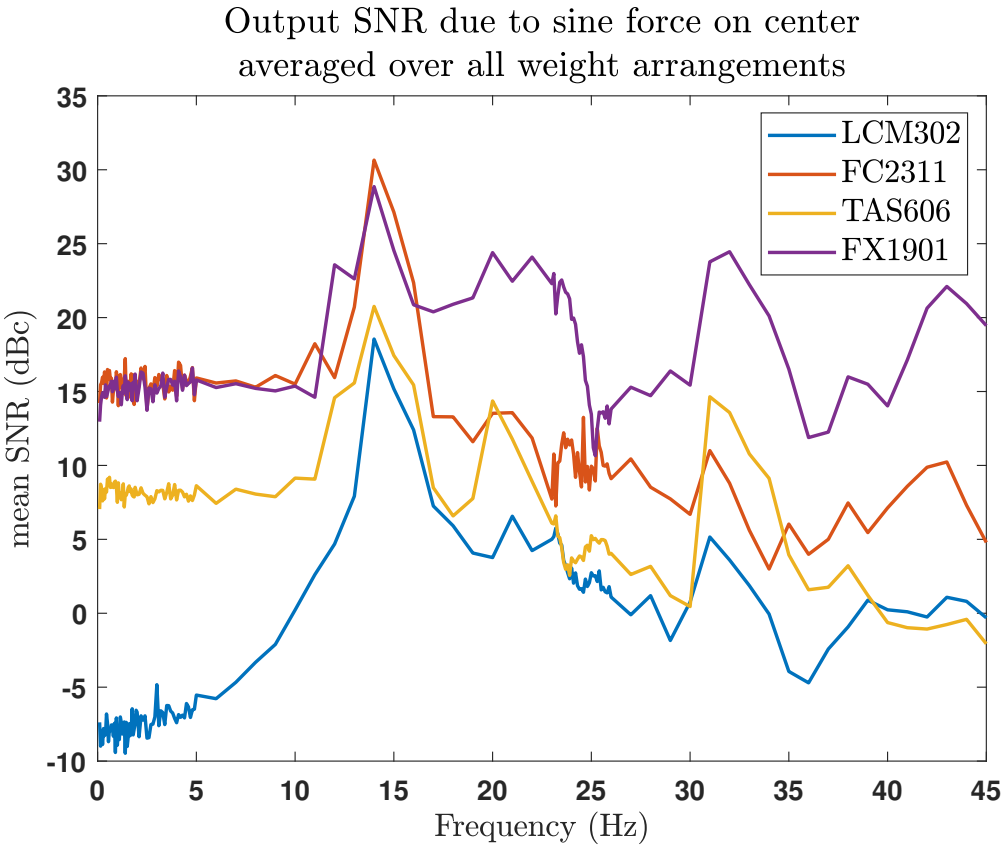

Figure 3.11: SNR of load cell responses to the sine wave forces with frequencies listed in Table 3.3 averaged over the four weight arrangements in Table 3.2

Chapter 4

Existing methods for BCG-based heart rate estimation and their performance

Primary results of this chapter was published in [110] and its final results are published in [111]. Please cite these publications rather than this dissertation.

4.1 Introduction

The BCG obtained by the system described in chapters 2 and 3 can now be used to estimate HBI from its J peaks. However, J peak detection from a BCG is not a trivial task. Several studies have proposed methods to detect J peaks [15, 16, 18, 21, 68, 77, 80, 82, 84, 117–125]. While most of these studies have reported reasonable J peak detection, it is hard to compare those results and select a method.

A few studies have performed small-scale comparisons of peak detection methods. For example, [15] quotes the performance of seven existing methods and [63] compares methods intended for camera-based sensors. Several groups have compared their proposed approach with previous methods from their own or affiliated labs [17, 68, 82, 126]. The "multi-method"

algorithm [77], which runs four peak-detection algorithms on a ballistocardiogram (BCG) segment and fuses results from the three best-performing methods, could be considered a comparison. However, it focuses on the overall performance of three fused methods as a single method. Finally, [127] compares the performance of the "Maximal Overlap Discrete Wavelet Transform (MODWT)" [68] with performances of three other signal processing techniques using the mean absolute error (MAE) between the resulting ECG-based and BCG-based pulse rates.

Based on this early review, a broad quantitative performance comparison of signal processing methods proposed by different research groups is lacking. Further, a consensus does not exist in this research community regarding which peak detection method best serves as a gold standard for performance comparisons. Such comparisons would be well served by (1) a common data set with which multiple methods could be tested and (2) access to original source code that would allow for accurate code replication. This paper proposes a framework where the performance of different BCG peak detection methods and their associated signal processing techniques can be objectively evaluated in terms of peak detection efficiency and sensitivity.

This work compares five BCG peak detection methods, where three are recreated from the literature [15, 17, 123] and two are adapted from original code [68, 82]. This original source codes were modified to address differences in sensing methods and sampling frequencies. The authors recently conducted a pilot study involving five participants in [110] to compare three peak detection methods [15, 17, 82]. The present study extends that work to include the performance of two additional methods [68, 123], where data from total of 30 participants supplement the original data in [110]. For clarity in this paper, each of these five methods is referred to by the last name of the corresponding first author: Lee [15], Lydon [82], Brüser [17], Alvarado [123] and Sadek [68]. A simple technique based on cross correlation (XCOR) is also included as a baseline for comparison.

This work contributes

• a comparison of five peak-detection techniques applied to load-cell data,

- two proposed peak-detection methods for use in HRV applications,
- performance benchmarks for researchers who seek to improve peak-detection performance and/or develop new BCG peak-detection approaches, and
- a portfolio of replicated algorithms for the peak detection methods presented here.

An overview of the signal processing and peak detection approaches utilized here is provided in Section I of the Appendix A. The reader is encouraged to refer to the original work for further details. When possible, the authors have preserved the terms originally employed in each study.

The rest of this paper is organized as follows. The Methods section describes the participant demographics, data collection approach, and performance metrics. That section also details the algorithm comparisons, including parameter optimization steps. The Results section reports the outcomes of these comparisons, and the Discussion section comments on these results, the limitations of these analyses, and future work.

4.2 Methods

4.2.1 Data recording

Thirty healthy volunteers participated in this study: fourteen male (ages 30.9 $\pm$ 6.3 years) and sixteen female (ages 46.0 $\pm$ 18.5 years). Participants provided informed consent, and the recording process was performed in accordance with Kansas State University Institutional Review Board protocol No. 9386. Each participant laid on their back on a full-size bed with a stiff mattress. BCGs were recorded using four Measurement Specialties FX1902 load cells positioned beneath the corner bedposts. The signal conditioning circuitry employed bandpass filters with corner frequencies of 0.05 and 35 Hz - these circuits are further described in [25]. ECGs were simultaneously recorded using a GE Datex-Ohmeda Cardiocap^{TM}/5 patient monitor. The conditioned BCGs and ECGs were digitized at 250 Hz using a National Instruments (NI) 9220 16-bit multichannel data acquisition system, and these data were transferred to a local PC with an NI 9184 Ethernet chassis controlled by a LabVIEW virtual

instrument. Data were visually inspected, and segments corrupted by motion artifacts were removed prior to heartbeat interval identification. From that point, all available data were included in the study.

4.2.2 Signal source selection

For each subject, a signal quality index (SQI) [128] was calculated for each of the four BCG segments acquired from the load cells, and then the BCG segment with the highest SQI was selected. That segment was then preprocessed as specified in each peak-detection method's original paper. SQI calculation details are provided in Section IV of the Appendix A.

4.2.3 Ground truth peak labeling

The most prominent BCG peaks, termed "J peaks," identify heartbeat times. Simultaneously-recorded ECG R peaks were used as visual aids to identify BCG J peaks (except for two participants whose data were acquired before an ECG was included and for one case where an ECG recording was not possible). Due to variability in R-to-I intervals [129], and consequently R-to-J intervals, automated ECG-based J-peak annotation was avoided. Instead, given labeling conventions as in [130, 131], and with R peaks as visual references, two sets of 100 consecutive J peaks from two separate two-minute-long BCG sections were visually identified and annotated for use as ground truth (GT) peaks. The first set was used to optimize each peak-detection method, and the second set was used to evaluate the method's performance. For the three BCG recordings where simultaneous ECG data were unavailable, only BCG sections with visually indisputable J peaks as depicted in Fig. 4.1 were included in the study.

4.2.4 Performance metrics

A detection percentage (Det.) parameter is used as a sensitivity parameter to quantify the ability of an algorithm to correctly identify J peaks (i.e., a true positive rate). A false

alarm rate (FAR) parameter represents the counter metric, or specificity. Any temporal shift introduced by a signal processing step was corrected so that the detected peaks in the BCG segment would align in time with their corresponding GT peaks. A detection, or true positive (TP), is defined as a detected peak that is within $d = 0.06$ sec of the GT peak [110]. While Šprager and Zazula [77] suggest 0.075 sec instead, this stricter criteria improves specificity and exceeds the IEC standard for ECG QRS detection, which is also used in [77]. If multiple peaks are detected within a target window, the positive peak closest to the GT peak is considered a TP, and the rest are counted as false positives (FPs). Likewise, peaks detected outside of the specified window are considered FPs. Unsuccessful detection within the target window near the GT peak is counted as a missed event or false negative (FN). The FAR is then defined as the number of all FP events between the first and last GT peaks divided by the time between the first and last GT peaks in seconds and is reported as counts/sec. The third metric considered in this study is the efficiency, r, as proposed in [77], which is defined in Eq. 4.1 as

$$r = \sqrt[3]{r_s \cdot r_p \cdot r_v} \tag{4.1}$$

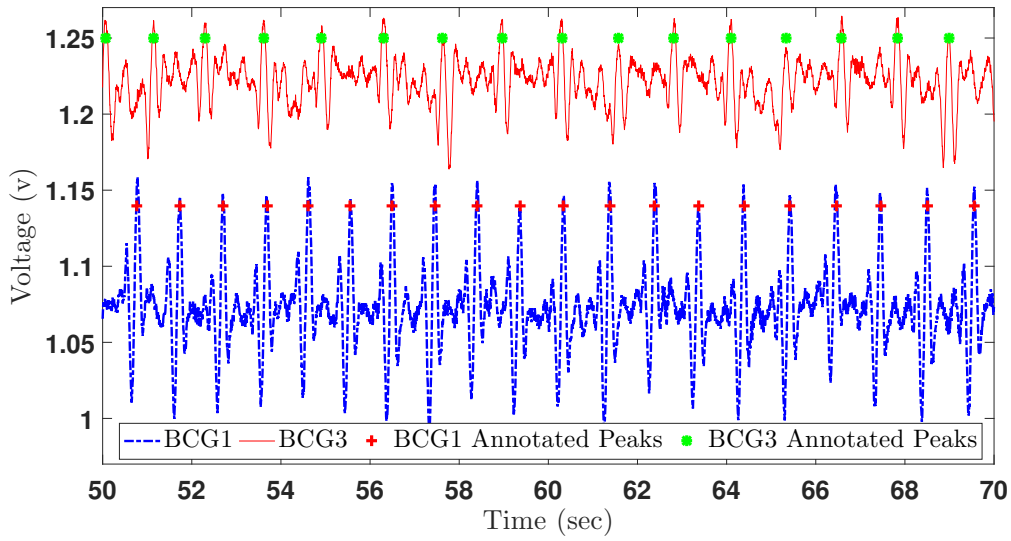

Figure 4.1: BCG excerpt with annotated J peaks for the 1st (bottom) and 3rd (top) participants for whom a simultaneous ECG was unavailable.

where r_s and r_p represent sensitivity and precision, respectively, and r_v is the variability score. These parameters are defined in [77] as

$$r_s = \frac{\text{TP}}{\text{TP} + \text{FN}} \tag{4.2}$$

$$r_p = \frac{\text{TP}}{\text{TP} + \text{FP}} \tag{4.3}$$

and

$$r_v = P\big(\big|t_{d_i} - \big(t_{r_i} + \bar{\tau}\big)\big| < d\big) \tag{4.4}$$

where P is the probability, t_{d_i} and t_{r_i} are the i^{th} time indices of the detected and GT peaks, respectively, and τ is the average time between detected and GT peaks if R peaks are used as GT peaks [77]. Since visually annotated J peaks are used as GT peaks, τ is dropped and Eq. 4.4 becomes

$$r_v = P\big(\big|t_{d_i} - t_{r_i}\big| < d\big) \tag{4.5}$$

Looking at Eqs. 4.2 and 4.5, however, one can see that Eq. 4.5 is numerically equivalent to Eq. 4.2, i.e., $r_v = r_s$, and therefore a modified definition for r_v is considered in this work to avoid duplication in Eq. 4.1. The modified definition proposed here is the ratio of the number of detections within $d/2$ to the number of detections within d:

$$r_{v_{mod}} = \frac{P\left(\left|t_{d_i} - t_{r_i}\right| < d/2\right)}{r_v} = \frac{P\left(\left|t_{d_i} - t_{r_i}\right| < d/2\right)}{r_s} \tag{4.6}$$

which leads to

$$r_{mod} = \sqrt[3]{r_s \cdot r_p \cdot r_{v_{mod}}} \tag{4.7}$$

and the efficiency for each method is computed using Eq. 4.7 instead of Eq. 4.1.

The fourth proposed metric is the MAE between the GT peak times and the detected peak times (MAE_p). This metric provides insight into J peak temporal jitter. The last performance measure is the *Absolute Error (AbsErr)* between each HBI based on GT peaks (HBI_{GT}) and each HBI based on detected J peaks (HBI_{det}). It is calculated using Eq. 4.8. Here, n is the total number of HBIs based on detected peaks from all participant BCGs.

$$AbsErr_n = \left|HBI_{GT_n} - HBI_{det_n}\right| \tag{4.8}$$

4.2.5 Parameter selection and optimization

Authors of some papers that present peak-detection methods either do not report one or more parameters, or the reported parameters lead to non-optimal performance when utilized with these BCG datasets. Reporting poor performance for a method would be arguably unfair if a simple parameter change would have made it competitive. Therefore, when replicating or adapting each method, the authors had to first optimize the method's performance by varying parameter values. To that end, a range of parameter values were iterated to obtain a set of Det. and FAR pairs for each method when applied to the first segment of a BCG with its associated GT peaks. The obtained Det. and FAR pairs were used to create receiver operating characteristic (ROC) curves. Parameter values were selected to maximize the area

under the curve (AUC) for each of the ROC curves (see Fig. 4.2). The plots include only the ROC curves for those methods that were able to produce smooth curves for detection rates above 65%. The factors limiting the depiction of ROC curves to detection rates above 65%, and only for certain methods, are discussed in 4.4.1 and 4.4.4, respectively.

Since the Lee and Lydon methods were originally tested on BCGs sampled at 1000 and 100 Hz, respectively, an up-sampled and down-sampled BCG were utilized in this work in addition to direct application on our 250 Hz data. These two scenarios are labeled "Lee-US" (up-sampled BCG) and "Lydon-DS" (down-sampled BCG). This step was taken to rule out the effects of a sampling frequency mismatch. The same approach was applied with the Alvarado and Sadek methods, but it led to incomparable performances, so the results were not reported. For the Sadek method, a "minimum peak prominence" (MPP) parameter was evaluated in addition to the original "minimum peak distance" (MPD) parameter utilized with the MATLAB "findpeaks()" function. This scenario was labeled "Sadek-MPP" and was included in the results as a comparable method to the other methods that used MPP.

The optimization process is illustrated by the flowchart in Fig. 4.3. $BCG1_m$ is the first two-minute-long BCG segment from the m^{th} participant, including its associated GT peaks ($GT\ peaks1_m$); the result from that segment is detected heartbeats (HB_d). The parameter(s) noted in the flow chart are summarized in Table 4.1.

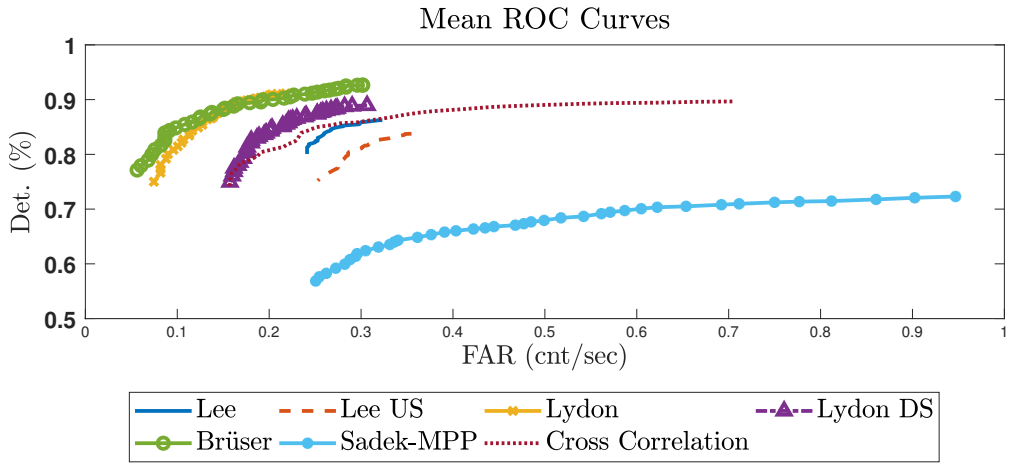

Figure 4.2: Mean ROC curves for the Lee, Lee-US, Lydon, Lydon-DS, Brüser, Sadek-MPP and XCOR methods. The -DS & -US methods are down- or up-sampled to match the original publication.

The rationale for picking these parameters and the other details of the optimizations are provided in Section II of the Appendix A. Also, a summary of the wavelet basis functions and the number of participants for whom these functions resulted in an optimal performance (with the Alvarado and Sadek methods) are provided in Tables I and II, respectively, in section III of the Appendix A.

4.2.6 Testing phase

After the parameters were optimized, performance metrics were computed when using the second BCG segment, $BCG2_m$, and its associated GT peaks, GT $peaks2_m$. These data were not used during the optimization process, so the peak-detection performance relative to these data should be a fair estimate of each method's ability. Fig. 4.4 illustrates this process further.

4.3 Results

The performance metrics described in Section 4.2.4 are summarized in Table 4.2. The columns report averages taken across the number of participants: aggregate results for Det. in

Table 4.1: List of parameters to be optimized for each method.

Method	Parameters Used
Lee, Lydon, XCOR	Moving-average (MA) Lengths
Lee, Lydon, XCOR, Sadek	"Minimum peak prominence" (MPP)
Brüser	sliding window overlap percentage, th_Q
Alvarado	wavelet basis function, wavelet decomposition level
Sadek	wavelet decomposition level, "minimum peak distance" (MPD), "Analysis Window" size

percent, FAR in counts per second, MAE_p in seconds, and r_{mod} in percent. Each row addresses a method noted in this paper.

The modified Bland-Altman plots in Figs. 4.5 and 4.6 display the *AbsErr* of each method on the dependent axis. The independent axis represents the HBI based on GT peaks as per recommendations in [132]. Each plot is based on aggregated HBI data for all 30 participants.

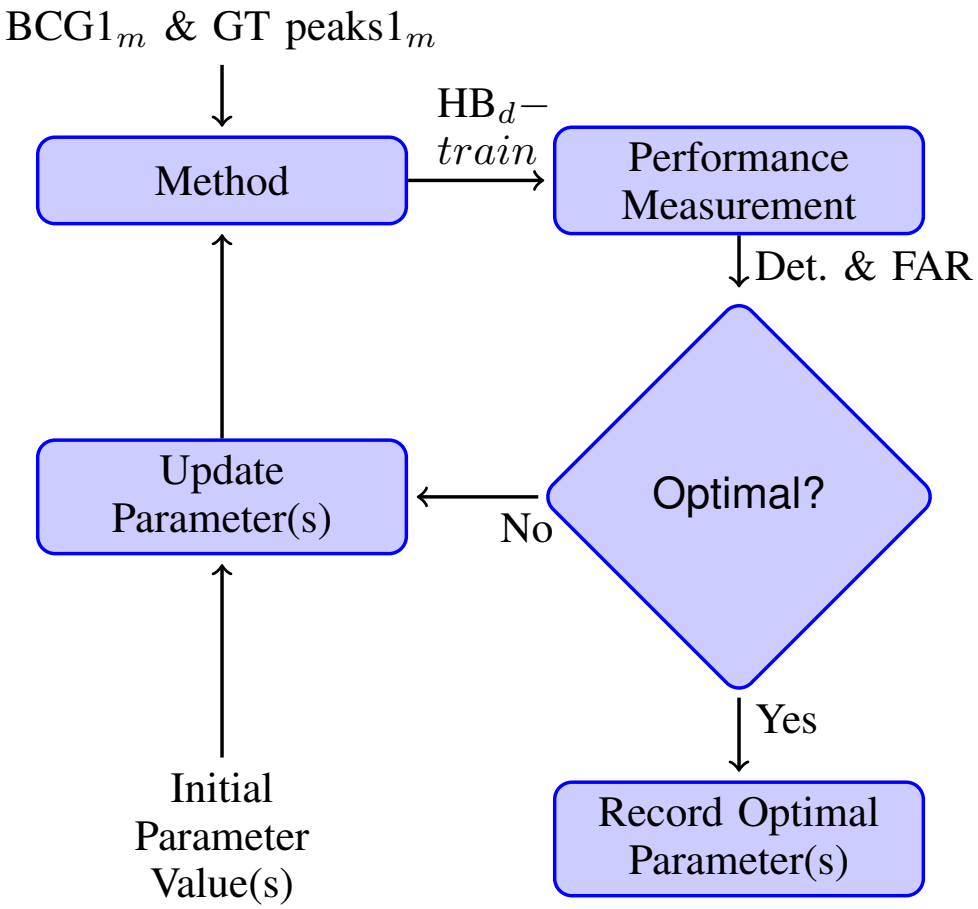

Figure 4.3: Performance optimization process. The path labeled "$HB_{d-train}$" indicates the **d**etected **h**eart**b**eats used to train the parameters to optimize the performance of a method.

Table 4.2: Performance metrics for the various peak-detection methods. Det.: detection rate in %, FAR: False Alarm Rate in alarms per second (cnt/sec), MAE_p: Mean Absolute Error between GT peak times and detected J peak times in seconds, and r_{mod}: Efficiency in %.

Methods	**Det. (%)**	**FAR (cnt/sec)**	**MAE_p(sec)**	**r_{mod} (%)**
Lee	82.8621	0.1047	0.0203	54.7228
Lee-US	82.5172	0.1028	0.0232	57.3578
Lydon	86.3448	0.0810	0.0175	66.0629
Lydon-DS	81.5172	0.0946	0.0184	60.8376
Brüser	88.9310	0.0766	0.0088	49.9188
Alvarado	79.3793	0.1714	0.0312	33.0721
Sadek	94.1724	0.0552	0.0175	44.9751
Sadek-MPP	70.2414	0.1920	0.0175	42.6856
XCOR	89.1724	0.1787	0.0103	52.3684

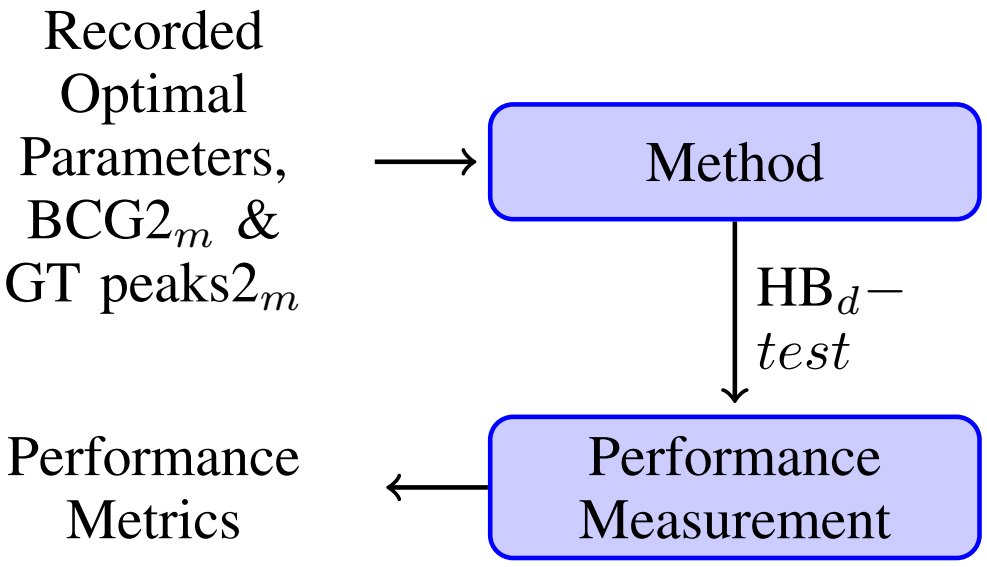

Figure 4.4: Performance evaluation based on the obtained parameters. The path labeled "HB_{d-test}" indicates the **d**etected **h**eart**b**eats used to test the performance of a method in conjunction with the parameters obtained in the optimization process, e.g., Recorded Optimal Parameters.

4.4 Discussion

4.4.1 Lee method

The advantages of this method are its relatively low FAR and its low sensitivity to the sampling rate, as noted in Table 4.2 (the performance metrics are not much different for

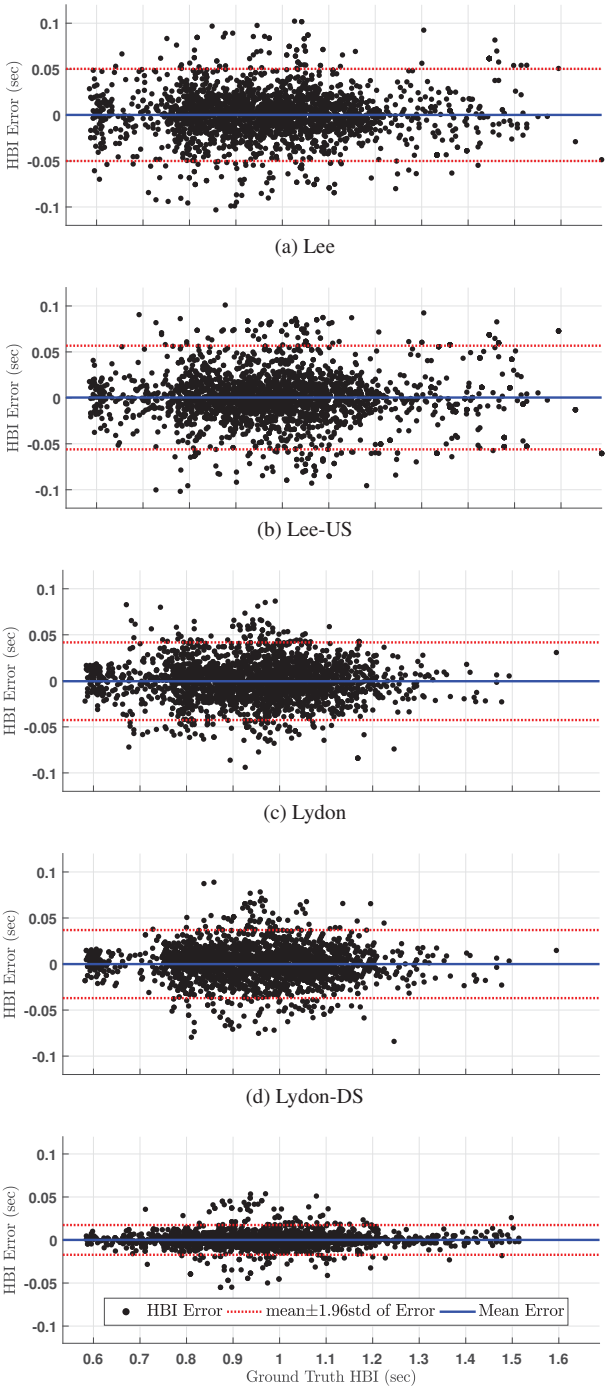

Figure 4.5: Modified Bland-Altman plots for the Lee, Lee-US, Lydon, Lydon-DS, and Brüser methods from top to bottom, respectively.

the Lee and Lee-US methods). This method also has the second highest efficiency (r_{mod}) for both sampling rates. The method's disadvantages are its relatively low detection power

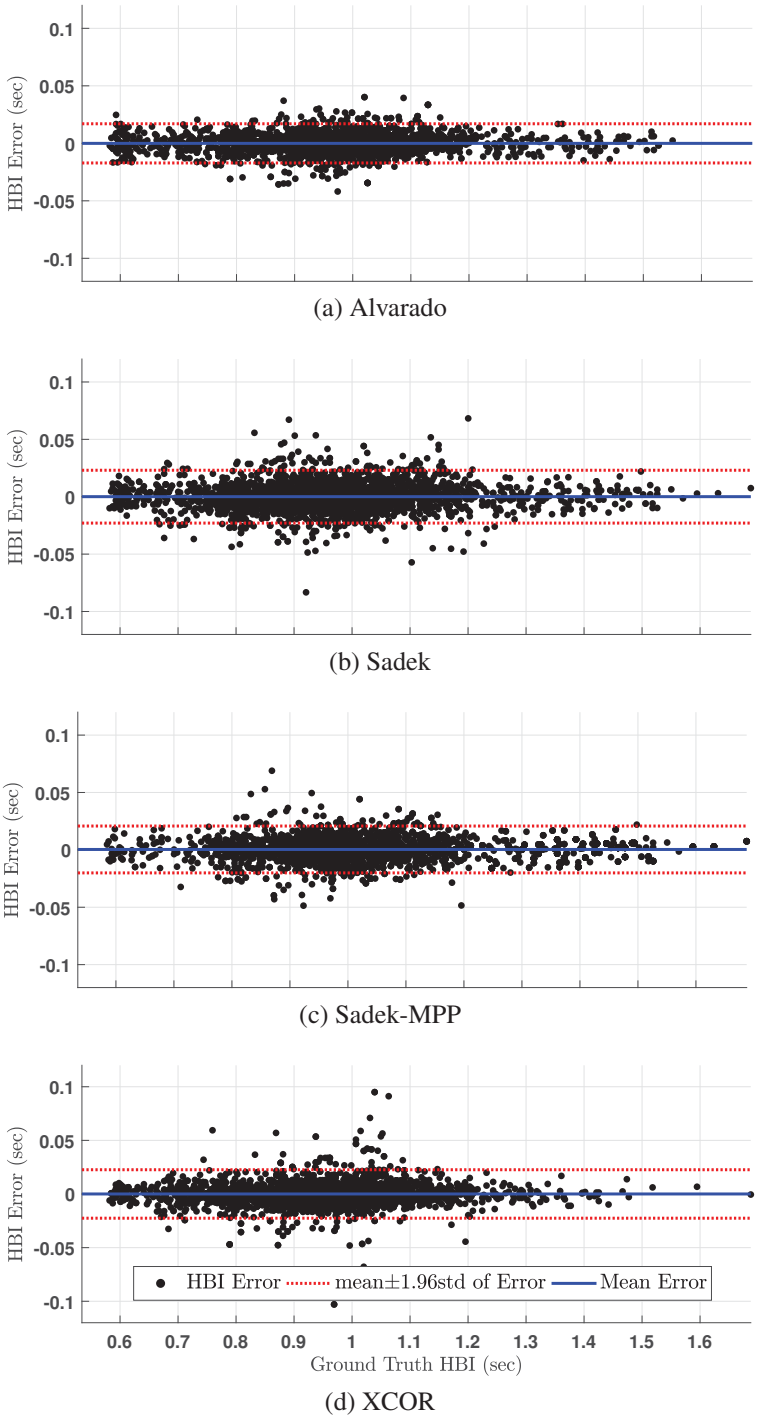

Figure 4.6: Modified Bland-Altman plots for the Alvarado, Sadek, Sadek-MPP, and XCOR methods from top to bottom, respectively.

and its second-highest MAE_p. The Lee and Lee-US methods produce the most dispersed Bland-Altman plots (see the top two panels of Fig. 4.5). Lee's method as replicated in this work is also sensitive to parameter variations, and this sensitivity increases in the case of an up-sampled BCG.

Since the next peak detection "analysis window" is based on the last peak detected in the previous window, it is not possible to create smooth ROC curves for larger ranges of the MPP values. Consequently, a complete ROC curve could not be produced during the optimization step. An example ROC curve for a wider range of MPP values is depicted in Fig. 4.7, where MPP was varied from 5e-4 to 10e-4 for participant 23. To address this issue, smaller ranges of parameter values were used to produce smooth ROC curve segments with detection rates exceeding 80% and FAR values below 0.2 cnt/sec. Exceptions were made for two participants because the parameter ranges needed to be as small as 2.2e-3 to 2.9e-3 in one case (participant number 6) and 3.2e-5 to 5e-5 in another case (participant number 3). Consequently, the Det. dropped to well below 80% and the effects were more pronounced in the Lee-US ROC curves, as can be seen in the second panel of Fig. 4.2. Similarly, for the Lee-US method applied to one participant's data, the FAR had to exceed 0.2 counts/sec to make a non-zero detection.

The method is prone to false positives introduced by end effects from filtering during each window. This problem can be alleviated by either performing preprocessing prior to windowing or by introducing an MA filter on the output. The latter was chosen but led to two MA length parameters that required optimization. Contrary to the initial study [110], performance was substantially improved by setting this second parameter in a subject-specific manner.

4.4.2 Lydon method

The advantages of this method are that it offers the highest r_{mod}, the third lowest FAR and MAE_p, and the easiest implementation after the XCOR method. The original code is also accessible. This method produced smooth ROC curves during the optimization process

and was much less sensitive to variations in MPP values compared to the Lee method. The disadvantages of this method are its relatively low detection rate and the fact that it produces the second most dispersed Bland-Altman plots (3^{rd} and 4^{th} panels of Fig. 4.5). In addition, the existence of two lengths for the MA filters, which need to be adjusted for different participants, adds to its complexity for real-time peak detection. Comparing the two sampling rate scenarios for this method, an improved performance arises in the Lydon method when compared to the Lydon-DS approach. This can be due to distortion/loss of information from down-sampling the BCG or the notion that this method may perform better with BCGs recorded at higher sampling rates.

4.4.3 Brüser method

The advantages of this method are that it has the lowest MAE_p, the second lowest FAR, and the third highest detection rate, plus it produces the second least dispersed Bland-Altman

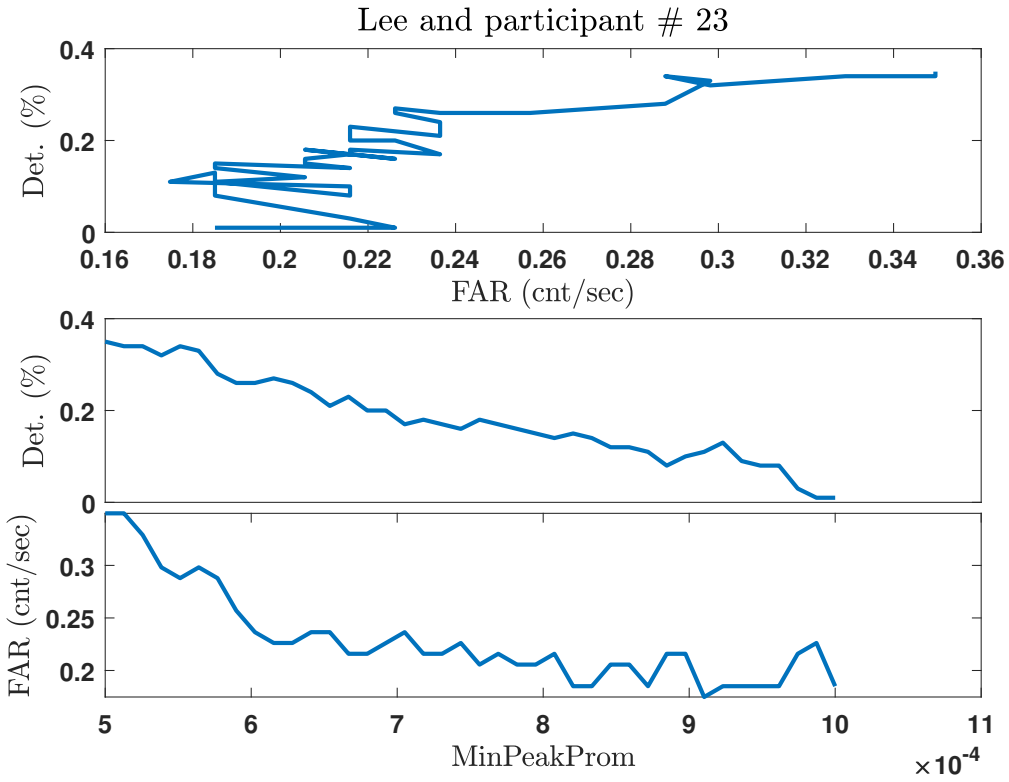

Figure 4.7: Top: ROC curve; Middle and bottom: Det. and FAR, respectively, vs minimum peak prominence (MPP) for a range of 5e-4 to 10e-4 for participant 23.

plot (see the 5^{th} panel in Fig. 4.5). This method is also less sensitive to parameter variations and produces good combinations of Det. and FAR for a larger range of parameter values. The ROC curves stay mostly near detection rates higher than 85%, with corresponding FARs as low as 0.07 counts/sec.

Interestingly, the version of Brüser's Method replicated for this work seems to produce better Bland-Altman plots when its detected peaks ("anchor points" in the original work) are used instead of the directly estimated HBIs, although this method primarily focuses on direct HBI estimation. Fig. 4.8 displays the modified Bland-Altman plot obtained from the aggregate HBI estimates. The Bland-Altman plot in this figure is more dispersed when compared to the Bland-Altman plot for the Brüser method in Fig. 4.5. Also note that the "mean±1.96std" lines have moved outside of the limits (-0.1 to 0.1 on the dependent axis) used for Bland-Altman plots in this paper.

Since this study primarily focuses on peak-detection performance, including the Bland-Altman plots due to HBIs obtained from detected peaks should still be sensible. With a single subject-specific parameter to control, this method could be attractive for longitudinal peak detection applications.

A disadvantage of this method is that it has the third lowest r_{mod} after the Alvarado and Sadek methods based on the numbers in Table 4.2. The statistical approach taken in this method to determine HBI estimates makes this method more interesting for long-term longitudinal studies, since more personalized estimators can be trained and better decisions can be made when picking suitable HBIs. On the other hand, this same approach makes this method less attractive for short-term HRV estimation applications, since prior data must be accumulated to enhance the estimators used when picking good HBI estimates.

4.4.4 Alvarado method

The advantage of this method is that it offers subject-independent amplitude and interval thresholds, owing to the adaptive nature of its peak detection algorithm, as opposed to the "findpeaks()" algorithm used in the other methods (except for Brüser's method). Out of the

six wavelet basis functions evaluated when optimizing this method, "bior2.2" resulted in the best performance for 13 BCGs. This suggests that it may be possible to deduce an optimal wavelet for a group of people with certain characteristics. This method also produces the least dispersed Bland-Altman plot: the 1^{st} panel in Fig. 4.6. The disadvantages of this method are that it produces the lowest r_{mod}, the lowest Det. after Sadek-MPP, the third highest FAR after XCOR and Sadek-MPP, and the highest MAE_p. Alvarado's method is also highly sensitive to wavelet decomposition scale selection in a non-linear fashion. For example, when changing from scale 68 to either 67 or 69 for a particular participant, the FAR will jump from zero to 0.66 or 0.63 counts/sec, respectively. Due to this non-linear sensitivity, a smooth ROC curve was not possible.

For the BCG data employed here, the originally-proposed 5^{th} decomposition level performed poorly, yielding an average detection rate of 27% and 0.89 counts/sec FAR. Different wavelet decomposition scales were therefore investigated. The best-performing scales were often much higher (between 19 and 76).

4.4.5 Sadek method

For Sadek's method, the Sadek and Sadek-MPP implementations will be discussed separately. The advantages of the Sadek algorithm are that it offers the highest detection rate, the lowest FAR, and the third lowest MAE_p, plus it produces the third least dispersed Bland-Altman

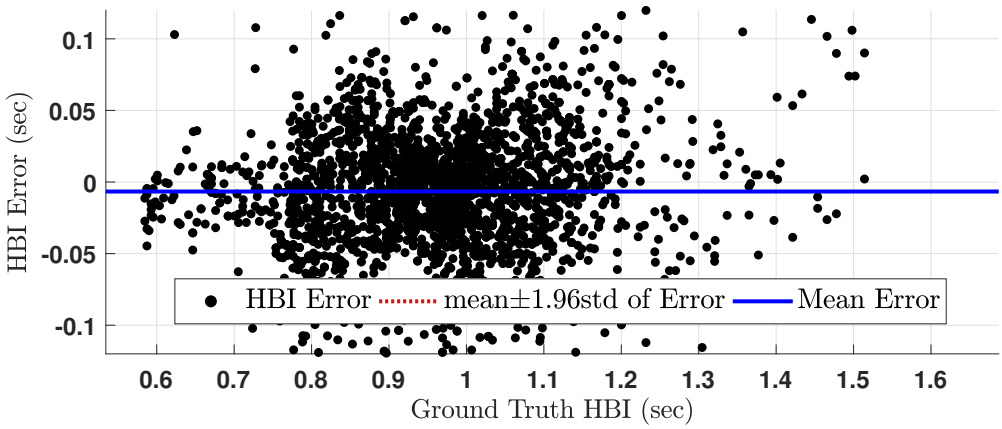

Figure 4.8: Modified Bland-Altman plot for the Brüser method when HBIs estimated by this method are used.

plot (panel two in Fig. 4.6). This method is also attractive because the code is publicly accessible. One disadvantage is that this method produces the third lowest r_{mod}. It also needs prior HBI data from a participant for proper "minimum peak distance" (MPD) selection, making short-term HRV studies impossible. In addition, this method lacks a means to find an optimal MPD value in the long run. Brüser's method, for instance, handles this automatically using statistical estimators. Because this parameter is fixed, the Sadek method may not be suitable for long-term or longitudinal studies due to changes in the underlying heart rate.

The advantage of the Sadek-MPP method is that it can be used for long-term longitudinal HRV studies, because once an optimal MPP is obtained, the MPP will not change unless the participant changes. The method's less dispersed Bland-Altman plot can be an advantage but is misleading due to the low number of detections obtained with this method; Bland-Altman plots do not account for misses. Other disadvantages of this method are that it offers the highest FAR, the lowest Det., the second-lowest r_{mod}, and a relatively high MAE_p.

The wavelet proposed in the original work, "sym8", appears to result in better performance for both the Sadek and Sadek-MPP methods when applied to these participant data. The wavelet decomposition scales do not vary significantly, and a wavelet decomposition scale of 6 seems to produce optimal results for 17 participants. This implies the possibility to identify a subject-independent scale for a group of individuals who share similar physiological and body composition traits. Note, though, that transitioning from the optimal scale to the neighboring scale impacts the performance severely. For example, a transition from scale 5 to scale 6 for participant 8 causes the detection rate to drop from 100 % to 32% and the FAR to increase from 0 to 0.64 counts/sec.

In this method, similar results are obtained whether or not windowing is applied. However, if windowing is applied, a 10-second window length as proposed in the original work is not always optimal. While the authors applied the windowing step when using an MPD to be consistent with the original work, this step was skipped when using an MPP. This can be justified because when windowing is applied after wavelet decomposition, end effects will not exist for each window and therefore will not affect the performance of the method. Also, the MATLAB "findpeaks()" function applies windowing anyway, which partly explains why

windowing does not affect performance in the first place.

Down-sampling these BCG data to the originally proposed sampling rate (50 Hz) severely impacts the performance of this method. For example, the average Det. drops to 13% and the average FAR jumps to 0.8855 counts/sec when tested with an MPD. Based on this observation, the Sadek-MPP method was not tested with a down-sampled BCG. Consequently, results for down-sampled data were not considered in the evaluation process.

4.4.6 Cross-correlation method

The advantages of this method are that it offers the second highest detection rate, the second lowest MAE_p, a relatively high r_{mod}, and minimal design complexity. The performance of this method is much less sensitive to parameter variations when compared to methods that use MPPs. As a result, it provides a larger range of parameter variations toward smoother ROC curves. As mentioned in the Methods section, the lengths of the MA filters were subject-independent except for the case of one participant whose data were later removed from the study since they caused this method to produce zero Det./FAR pairs. The disadvantages of this method are that its FAR is the second highest, and it produces a relatively more dispersed Bland-Altman plot see panel four in Fig. 4.6. The fact that it failed to find a non-zero Det./FAR pair for the BCG of a particular participant is another negative point, although those BCG data caused the Lee and Lydon methods to perform poorly as well.

4.4.7 Limitations

While considerable effort has been expended to accurately replicate each method, the possibility of error remains. Original code was not available from most of the affiliated authors (except for the authors of [82] and [68]), and some details necessary to replicate the methods were missing from each paper. Therefore, it is sensible to note that the results presented in this study relate to the performance of the authors' *replications* of each method. The parameter optimization process was included to mitigate the effects caused by inconsistencies in method implementations relative to the algorithms created for the original papers.

An occasional small modification was necessary to avoid unfairly penalizing a given method. For example, a simple MA filter was added to the Lee and Lydon methods, since their performance would otherwise have been very poor. Some parameters either were not listed in the original publications or were obviously inappropriate for these BCG data; these parameters were adjusted through the parameter optimization step described earlier. For many parameters, though, the published values were used directly without investigating other settings. Notably, the filter types, orders, and corner frequencies were implemented as published. Optimizing these parameters may have led to increased performance for some methods, but doing so would substantially increase the complexity of the optimization. While some methods originally included an automatic motion artifact removal step, that step was skipped in this study since the BCG segments selected for this work were already free of motion artifact.

As mentioned in the Methods section, BCG selection (i.e., one signal out of four available load cell signals) was based on the signal with the highest SQI. While this step was performed with the goal to select the best BCG, a higher SQI did not necessarily result in better algorithm performance. Nonetheless, the performance comparison is still reasonable, since the same BCG data were presented to all methods.

The overall low r_{mod} as noted in Table 4.2 is due to the $r_{v_{mod}}$ factor in Eq. 4.7, which is defined in Eq. 4.6. Eq. 4.6 is relatively strict at present. Ultimately, however, the research goal is to place limits on the HRV estimate error rather than the time-domain jitter. Further study will be required to elucidate this relationship.

A Bland-Altman plot compares only one performance aspect: the error between a GT value and an estimate. Since false alarm events are ignored, similar plots can be obtained for two methods with similar jitters but very different Det. and FAR values. The authors therefore suggest that Bland-Altman plots are suitable but not fully sufficient for this type of method comparison.

Since the BCG ground truth peaks were not based on the R peaks of ECG data, the mean relative error between the R-to-R intervals (RRIs) and the heartbeat intervals (HBIs) [133] was not used as a performance criterion in this work. Here, the authors believe that

MAE_p is a good replacement for this measure.

4.4.8 Future work

The role of sensor modality is unclear in terms of performance differences between these peak-detection methods. The Lee method was originally proposed for use with load cell data, consistent with this work. Lydon *et al.* used water pressure sensors in their original work, but the Lydon method can clearly be successfully used with load cell-based BCGs, since Lydon's method outperformed Lee's method in this study. Similarly, Brüser's method, though originally designed for data acquired with electromechanical films, had a high number of detections and a low timing jitter. This suggests that Brüser's method may be more robust to sensor changes than the other techniques. On the contrary, the Alvarado and Sadek-MPP methods, originally proposed for fiber-optic based sensors, performed poorly. Perhaps the sensor modality mismatch is one reason. Further study is needed.

The existence of at least one subject-dependent parameter for each method suggests that these methods will achieve their best performance in long-term and longitudinal studies only if the parameters are personalized for each user. Since each data set for this study originated from a single session, the authors cannot speak to the stability of these parameters over time.

In this study, a timing jitter up to 0.06 sec (when comparing a candidate peak to a GT peak) resulted in the tally of a detected peak. However, it is not yet clear how much timing jitter can be allowed before an HRV feature estimated using these detected peaks will become useless. Further studies are necessary to assess the impact of timing jitter on the quality of the HRV features.

As mentioned earlier, the results of this study are based on BCGs with no motion artifacts. When processing longer BCG segments, where motion artifacts are unavoidable, an automatic motion detection algorithm such as in [108, 109] may prove useful. The preferred peak-detection method as identified by this work can then be applied to the remaining clean BCG data.

BCGs are not the only unobtrusive signals used for heartbeat detection. Several other

non-contact heartbeat detection methods have been proposed in the literature, such as capacitive ECGs [29–34], mattress-based PPGs [35], PPG imaging [36–41], optical Doppler or laser-based techniques (e.g., for tracking the cardiac chamber or arterial wall movements) [57–62], thermography [134–137], video-based motion analysis [138, 139] (see [63] for a thorough review), and high frequency electromagnetic fields [140–144] (see [145] for a review and elaboration of some of these approaches). The platform developed for this work may show promise when comparing the performance of heartbeat detection methods applied to data acquired using these other sensing modalities.

4.5 Conclusion

This paper compared the peak-detection performance of various algorithms when applied to ballistocardiographic data acquired from load cells placed under the corner posts of a bed. No single method excelled in all comparison categories. However, Brüser's method had the lowest timing jitter, the second lowest false alarm rate, and the third highest detection power. Sadek's method also exhibited good performance, offering the highest detection power, the lowest false alarm rate, and the third lowest timing jitters; it would be a strong candidate if not for its high dependence on the "minimum peak distance" parameter, which requires prior knowledge of an individual's heartbeat interval. On the other hand, Sadek's method does have a subject-independent wavelet basis function which would be desirable if a robust scheme to train the "minimum peak distance" could be developed. Interestingly, the simple XCOR method presented by the authors would be in third place, as it yielded the second highest detection power and the second lowest timing jitter. However, the high false alarm rate reported by this method requires attention. The code that implements the framework proposed in this study is accessible upon request to the corresponding author. A link to Code Ocean repository will be available in the future.

4.6 Acknowledgments

Opinions, findings, conclusions, or recommendations expressed in this material are those of the authors and do not necessarily reflect the views of the funding agencies. Human subjects work affiliated with this research was approved by the Kansas State University Institutional Review Board under protocol No. 9386. The authors acknowledge and appreciate the cooperation of Dr. Skubic and her team, as well as Dr. Mokhtari and his team, for providing the original code for the Lydon and Sadek methods, respectively.

Chapter 5

The effects of BCG peak detection errors on the HRV feature quality

5.1 Introduction

Based on the conclusions of Chapter 4, the best-performing method still introduces timing jitter in the detected J-peaks. This timing jitter is with respect to GT-peaks as described in Chapter 4. The jitter results in differences between HBI obtained from detected J-peaks (HBI_{det}) and HBI obtained from the GT-peaks (HBI_{GT}). For easier reference we will call this error the HBI_{det}-HBI_{GT} error. Based on the Bland-Altman plot for the best-performing method (bottom-most panel of Fig. 4.5), the resulting HBI_{det}-HBI_{GT} error seems to be less than 15ms for a total of 3000 heartbeats from 30 participants (100 heart beats from each participant).

While an HBI_{det}-HBI_{GT} error of less than 15 ms is comparable with HBI errors reported in other HBI-related studies (Table 5.1), the effects of this range of error on the validity of resulting HRV features is not known. In fact, the impact of HBI error on the accuracy of health-related interpretations from HRV features doesn't seem to have been investigated.

Although [84, 118, 147] have reported the resulting errors in HRV features due to the JJI error and [18, 88] have reported correlation coefficient between JJI-based HRV features

Table 5.1: List of JJI-RRI errors. MAE: Mean Absolute Error; RelErr: Relative Error; Det. Rate: Detection rate; FPR: False Positive Rate; FNR: False Negative Rate; ME: Mean Error. Empty cells mean unavailable.

Reference	N	MAE (ms)	ME (ms)	RelErr (%)	Det. Rate (%)	FPR (%)	FNR (%)	Coverage (%)	Remarks
[119]	1				92.7	0.5			
[120]		24	7			0.25	2.86		BCG model
[17]	33	7		0.78				72.69	
[21]	6			0.35					
[19]	16	16.61		1.79				95	
[77]	14	22							
[117]	5			0.75					
[146]	10	17							

and RRI-based HRV features, the effects of such errors and discrepancies have not been extended to the validity of resulting HRV features. For example, this information doesn't help to establish a relationship between JJI-RRI error and sleep staging accuracy - one of several HRV applications.

An exception can be made for two studies of a single research group [80] and [148]. They have reported their JJI estimation performance in [80] and sleep staging accuracy based on that JJI in [148] where the accuracy was estimated based on polysomnogram (PSG)-based sleep scores. However, the contribution of JJI estimation error to the sleep accuracy cannot be back-calculated since JJI was not the only signal used in the study. Furthermore, the only published application of JJI-based HRV features appears to be sleep staging, and even in this area the studies have been limited to [4, 84, 88, 91, 147, 149–151] to our knowledge. As a result, an agreed upon baseline for JJI-RRI error range does not exist beyond which one should know that the resulting HRV features from the underlying JJI will no longer be valid.

The focus of this chapter is to investigate the effects of JJI-RRI error on the quality of resulting HRV features. In order to conduct this study, it is necessary to evaluate the accuracy of health-related information inferred from the HRV features estimated from the JJI in question. For that purpose, this work studies the effects of JJI-RRI error on the accuracy

of sleep staging based on the HRV features. This task is accomplished by introducing random timing jitters in the R peaks of the ECGs obtained from the sleep data in the National Sleep Research Resource (NSRR) database. In addition, the error between JJI_{det}, also known as HBI_{det} in Chapter 4, and RRI obtained from the data used in Chapter 4 will be compared to the JJI-RRI error obtained from the ECG sets of the NSRR database.

Although other applications can be imaged, we chose sleep staging to be able to compare with prior work. Furthermore, methods already exist for sleep staging with HRV features obtained from the R-peaks of an ECG [152–156]. In addition, the ready availability of sleep data with their associated ECG from the NSRR database was another motivation.

5.2 Methods

5.2.1 Data description

Simulated JJI-RRI error

We accessed the NSRR database to investigate the effects of HBI error on the accuracy of sleep staging. The NSRR database contains de-identified sleep and other physiological data including ECG recordings with corresponding sleep stage labels. The sleep stages are labeled by sleep experts using PSG. The PSG contains ECG, from which we can obtained HRV features synchronous to those sleep stage labels. To our knowledge, no database includes simultaneous BCG signals and expert sleep scores.

The R-peaks obtained from the ECG is assumed to be our clean and ground truth heartbeat data. Then artificial perturbations to the R-peak location is added to mimic timing jitter in the detected J-peaks of BCG. Following, RRI from clean and error-contaminated R-peaks are obtained. The RRI from R-Peaks with time jitters simulates the JJI from the detected J peaks of a BCG, i.e., JJI_{det}. Consequently, it is possible to calculate JJI_{det}-RRI error. The process continues by increasing the standard deviation of the perturbations until the MAE between RRI and JJI_{det} reached 60 ms. We specified 60 ms as the maximum based on the Bland-Altman plots in Fig. 4.5 and Fig. 4.6 of Chapter 4. There, the HBI error, i.e.

HBI_{det}-HBI_{GT} error, was typically below 60 ms.

The MAEs between the RRI and each JJI (the JJI_{det} resulting from R-Peaks with random jitter) are obtained and each resulting JJI_{det} time series is then considered for HRV feature estimation and further sleep staging. A sleep staging error is obtained and recorded against each MAE. The effect of those R-peak perturbations on different features of HRV, in both the frequency and time domains, is examined. The mentioned perturbations are supposed to mimic the heartbeat detection errors when using BCG for HRV analysis.

Lab-based JJI-RRI error

The data from 5.2.1 will later be used to estimate the total allowable difference between GT, R-peak based HBI (RRI) and detected, J-peak based HBI (JJI_{det}). This difference captures all of the sources of error listed in 1.1, i.e., physiology, platform effects, and system errors. By contrast, the metrics calculated in 4.2.4 refer to the temporal difference between GT and detected J-peaks (JJI_{GT} vs JJI_{det}), which captures only system errors. Thus the metrics are not directly comparable. Rather, we must augment the numbers in 4.2.4 with the RRI-JJI_{GT} error. The RRI-JJI_{GT} error captures both the physiological differences and platform effects, making the metrics comparable, and can be included through simple addition.

It is worth mentioning that the RRI-JJI_{GT} is a bi-product of the study conducted in Chapter 4 where simultaneous ECGs was recorded when collecting BCGs.

5.2.2 HRV features

Frequency and time domain features of the HRV for each RRI and JJI_{det} time series were calculated using 5 minute sliding windows with 90 % overlap.

Frequency-domain features

Low frequency (LF) and high frequency (HF) power was calculated using the Lomb-Scargle normalized periodograms [157, 158] due to the unevenly sampled nature of the RRI and JJI_{det} time series. The LF and HF frequency ranges correspond to 0.04-0.15 Hz and 0.15-0.4 Hz

respectively [153]. In addition, the ratio of LF to HF, and one-dimensional median-filtered version of the ratio were considered as two other frequency-domain features.

Time-domain features

The mean of RRI (HR) and standard deviation of RRI (SDNN) in each window were used as time domain features.

5.2.3 The effects of JJI-RRI error on sleep staging accuracy

In order to examine the effects of HBI error on the quality of HRV features, in terms of their role in sleep staging accuracy, the following tests were examined:

Bayes error test

Parametric estimates of the Bayes error: The Bayes error between two sleep stages was first estimated using parametric methods. In parametric methods, the simplest bounds of the Bayes error can be calculated from Bhattacharyya distance [159].

$$\delta = \frac{1}{8}(\mu_1 - \mu_2)^T \Big(\frac{\Sigma_1 + \Sigma_2}{2}\Big)^{-1}(\mu_1 - \mu_2) + \frac{1}{2}\ln\frac{|\frac{\Sigma_1+\Sigma_2}{2}|}{\sqrt{|\Sigma_1||\Sigma_2|}} \tag{5.1}$$

where μ_i and Σ_i are the mean vectors and covariance matrices for classes $i = 1 and 2$, respectively. Using the Bhattacharyya distance in Eq. 5.1 and prior class probabilities $p(c_i)$ for classes $i = 1, 2$, Bayes error bounds can be obtained [160]

$$\frac{1}{2}\big(1 - \sqrt{1 - 4p(c_1)p(c_2)\exp(-2\delta)}\big) \leq E_{bayes} \leq \exp(-\delta)\sqrt{p(c_1)p(c_2)} \tag{5.2}$$

Eq. 5.2 gives a simple way of computing Bayes error if the class distributions are known and it is restricted to a 2-class problem. In calculating Bayes error two scenarios, single feature and multiple feature, were tested. In the single feature scenario one HRV feature

was used to estimate Bayes error between distributions of that HRV feature from two sleep stages. In the multiple feature case, all the estimated features were used together to calculate Bayes error for separating the two sleep stages. The sleep stages were tested in their original labels as well as in their re-labeled version as REM and N-REM. The N-REM in that case would include all non-REM and non-wake stages. These errors were calculated for RRI time series and, as well as for all the JJI versions, obtained in 5.2.1.

Non-parametric estimate of the Bayes error: Parametric estimates of the Bayes error requires knowledge of class distribution parameters and their prior probabilities. To estimate Bayes error in the absence of this information, non-parametric approaches can be used. For instance, a method for L-class classification problem is provided in [161] using nearest-neighbor (NN) classification. The NN classifier uses a predetermined distance metric to find the closest class label for a given instance. Given an L-class problem with sufficiently large training data, the Bayes error bounds can be calculated using Eq. 5.3 [162]:

$$\frac{L-1}{L}(1-\sqrt{1-\frac{L}{L-1}E_{NN}}) \leq E_{bayes} \leq E_{NN} \tag{5.3}$$

Here again the data were tested using the original labels as well as in their re-labeled version (only REM and N-REM) as described above.

Classification accuracy tests

For this test, classification accuracy was estimated using the HRV features. The HRV features due to all levels of jitters in the R-Peaks as explained in 5.2.1 were examined and the resulting classification accuracy was recorded against MAE of the underlying HBI for plotting. Two classifiers were used in this process, k-nearest neighbors (K-NN) algorithm and support vector machine (SVM). Two scenarios were tested: (*i*) all labels of sleep stages were provided as class labels, and (*ii*) Non-REM sleep stages were merged to a single stage and assigned a single label resulting in three stages, REM, N-REM and Wake. In the latter scenario the

modified labels were provided as class labels to the classifier. In each scenario, two forms of tests were performed. In the first form, all the HRV features were provided to the classifier. In the second form, only one feature was provided to the classifier at a time.

5.3 Results

5.3.1 Parametric Bayes error

Fig. 5.1 includes plots of the Bayes error curves against the MAE between JJI_{det} and RRI due to the increased levels of time jitter in the R-peaks. The Bayes error is estimated between distributions of all HRV features of each pair of sleep stages. Vague gray lines in the background belong to error curves for each participant whereas the dotted, bold and black line is their ensemble average which shows the general trend of the curves.

Fig. 5.2 includes plots of the Bayes error curves against the MAE between JJI_{det} and RRI due to the increased levels of time jitters in the R-peaks. The Bayes error is estimated between distributions of all HRV features belonging to REM and N-REM pairs of sleep stages.

As can be seen in Fig. 5.3, the Bayes error between some Non-REM sleep stages (particularly S1/S2, and S2/S3) is quite large. Therefore further comparisons using parametric Bayes error for individual Non-REM stages is not done in this work.

KNN-based non-parametric Bayes error

Panel *a* of Fig. 5.4 shows KNN-based Bayes error due to all HRV features used together in the KNN algorithm. The resulting error curves are obtained using Eq. 5.3. All sleep stage labels were provided as classification labels for creating this plot. Similarly, panel *b* of Fig. 5.4 shows the error curves obtained from Eq. 5.3. While all features were still provided to the KNN algorithm, the sleep stage labels were modified such that non-REM sleep stages were all given a single label.

The panels of Fig. 5.4 show KNN-based Bayes error due to individual HRV features used

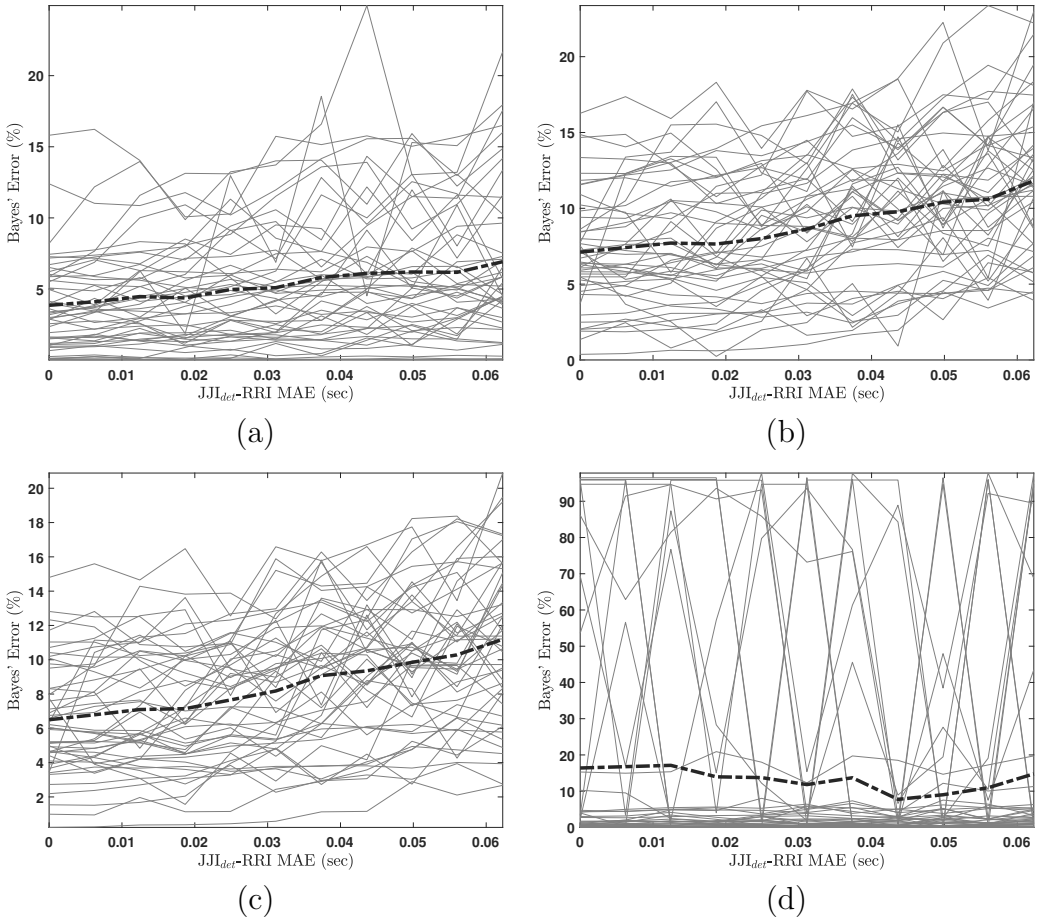

Figure 5.1: Bayes error between multi-variate distributions of all HRV features obtained from the sleep stages: (a) S1 and REM, (b) S3 and REM, (c) REM and N-REM, (d) S2 and REM.

one at a time in the KNN algorithm. Again, the resulting error curves are obtained using Eq. 5.3. All sleep stage labels were provided as classification labels for creating these plots.

Similar to the plots in Fig. 5.4, the plots in Fig. 5.6 show KNN-based Bayes error due to individual HRV features used one at a time in the KNN algorithm. However, the contrast is that the sleep stage labels are modified such that non-REM sleep stages are combined into a single label.

5.3.2 KNN classification error

The following figures provide sleep stage classification errors obtained using RRI and JJI$_{det}$s with different MAEs for HRV feature estimation. Again, the gray curves in the background

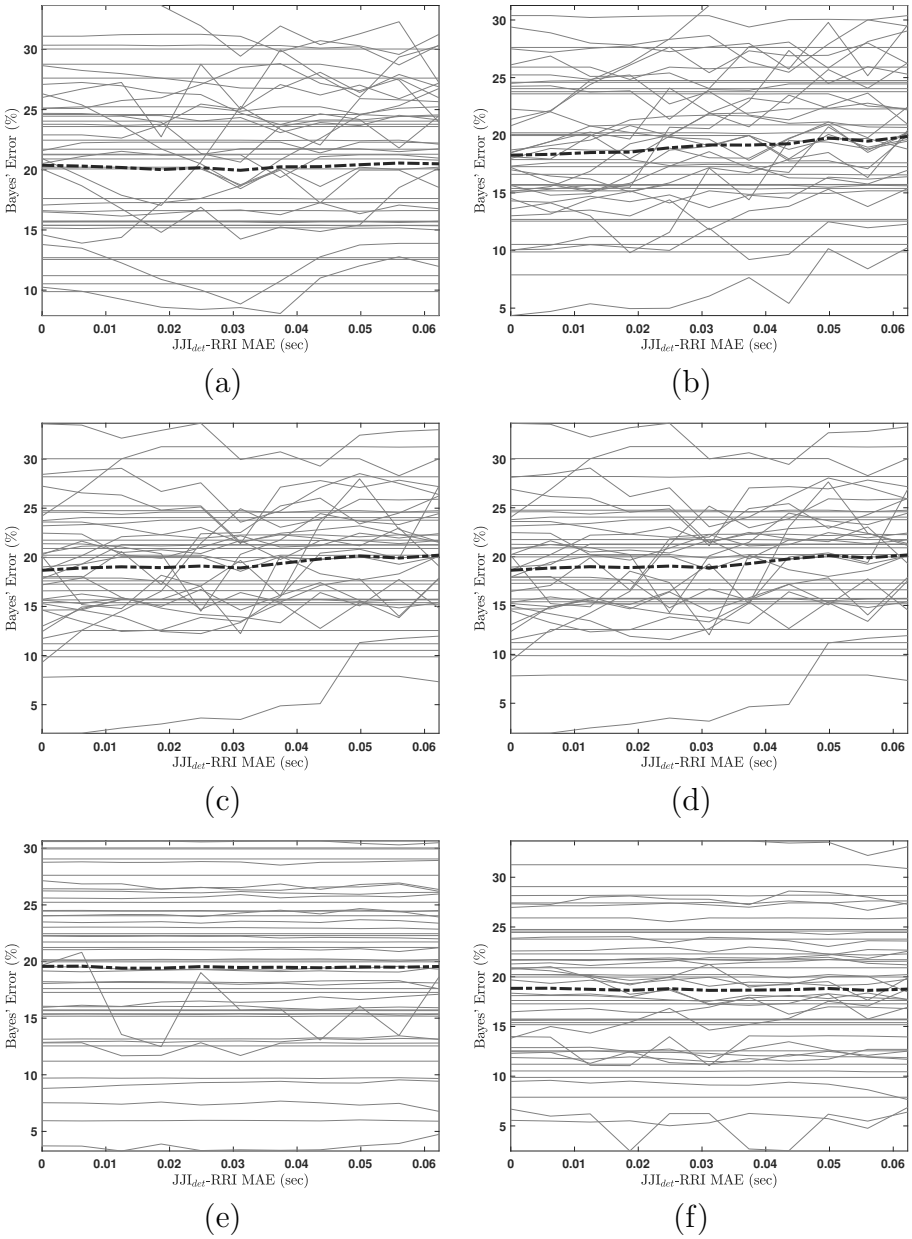

Figure 5.2: Bayes error across REM and N-REM using the HRV features: (a) LF, (b) HF, (c) ratio of LF to HF, (d) median-filtered ratio of LF to HF HR, (e) HR, (f) SDNN.

belong to each individual participant whereas the dotted bold black line is the ensemble average of those curves.

Panel *a* of Fig. 5.7 shows KNN-based classification error due to all HRV features used together in the KNN algorithm. All sleep stage labels were provided as classification labels for creating this plot. Panel *b* of Fig. 5.7, on the other hand, shows classification error

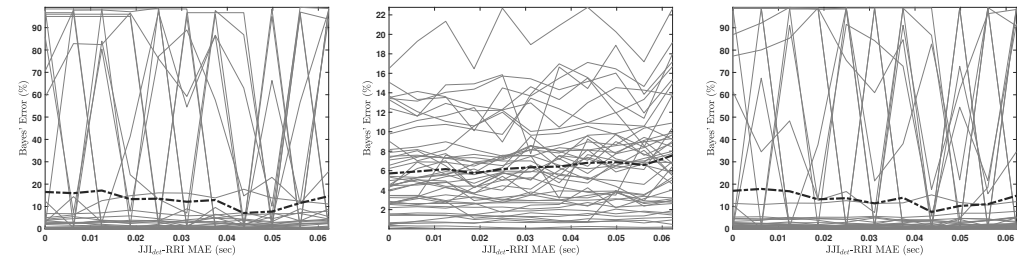

Figure 5.3: Bayes error between multi-variate distributions of all HRV features obtained from the sleep stages: (a) S1 and S2, (b) S1 and S3, (c) S2 and S3

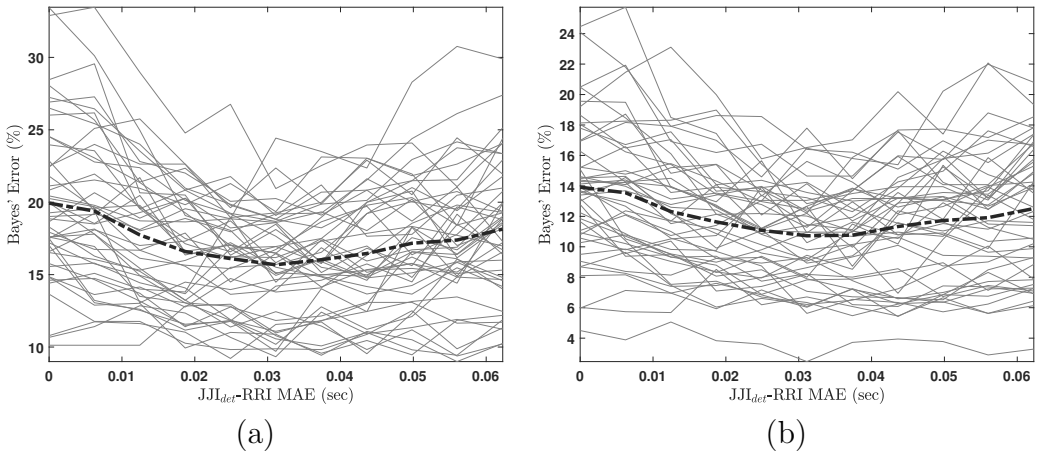

Figure 5.4: KNN-based Bayes error due to all HRV features when: (a) All sleep stage labels were present, (b) Non-REM sleep stages were merged.

between REM and N-REM stages where the sleep stages not belonging to the REM stage were given a single label, i.e., N-REM. Here, all HRV features were provided to the KNN algorithm.

The panels of Fig. 5.8 show KNN-based classification error due to individual HRV features used one at a time in the KNN algorithm. All sleep stage labels were provided as classification labels for creating these plots.

Similar to the plots in Fig. 5.8, the plots in Fig. 5.9 show KNN-based classification error due to individual HRV features used one at a time in the KNN algorithm. The contrast here, however, is that the sleep stage labels are modified such that non-REM sleep stages are combined into a single label, N-REM.

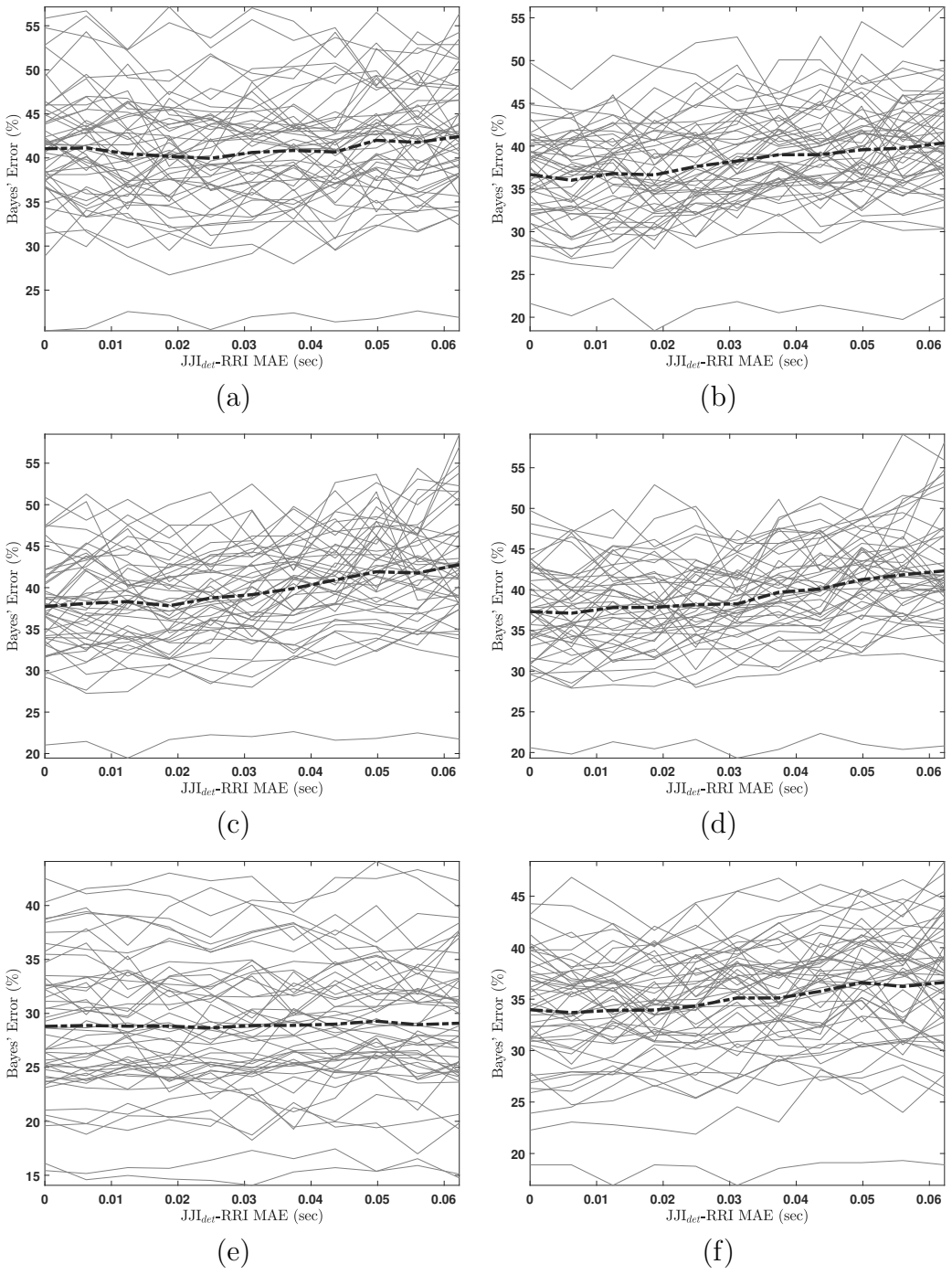

Figure 5.5: KNN-based Bayes error across all sleep stages using the HRV features: (a) LF, (b) HF, (c) ratio of LF to HF, (d) median-filtered ratio of LF to HF, (e) HR and (f) SDNN.

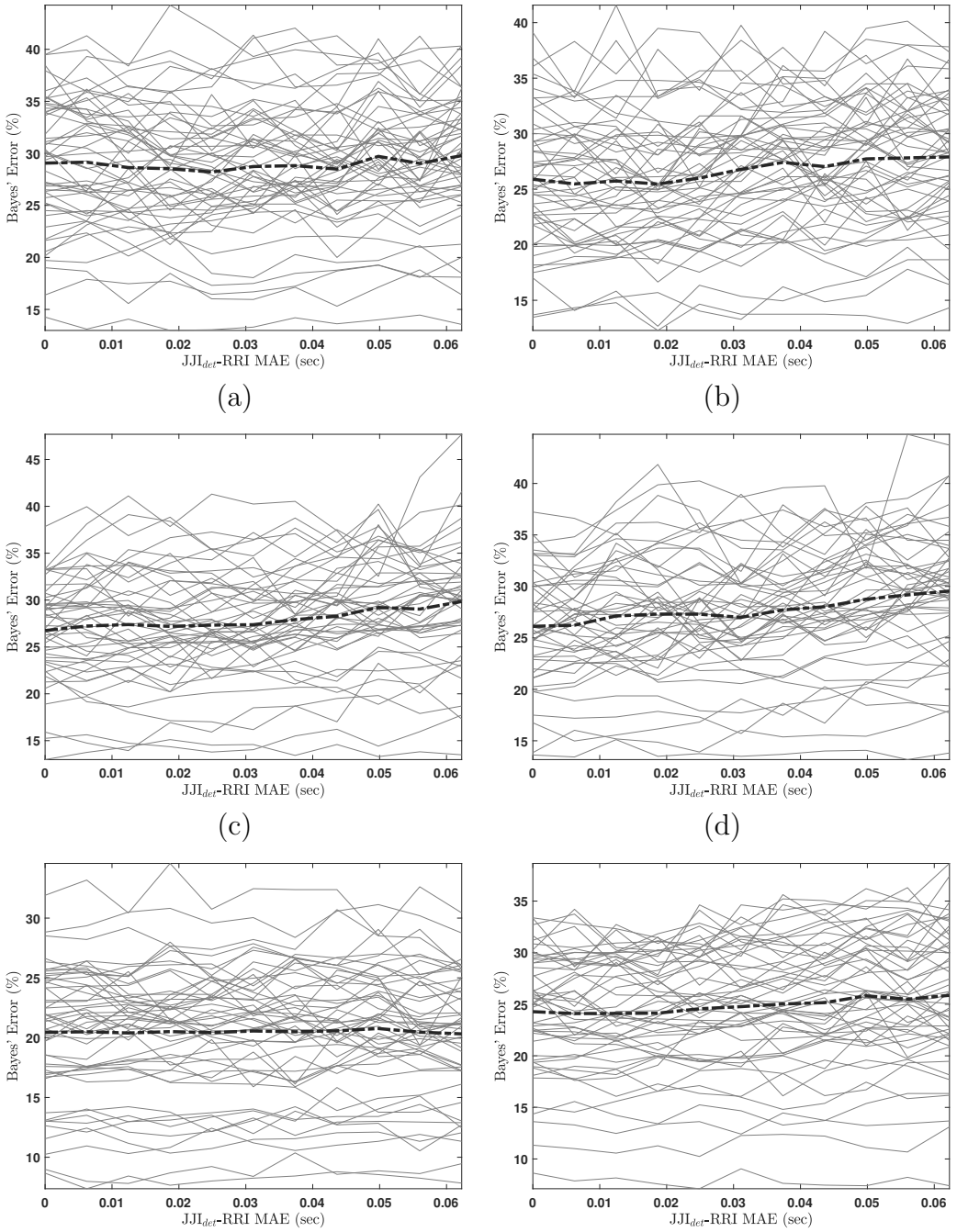

Figure 5.6: KNN-based Bayes error across all sleep stages when non-REM sleep stages were merged to a single stage of NREM. Bayes error was calculated using the HRV features: (a) LF, (b) HF, (c) ratio of LF to HF, (d) median-filtered ratio of LF to HF, (e) HR and (f) SDNN.

5.3.3 SVM classification error

Panel *a* of Fig. 5.10 shows SVM classification error due to all HRV features used together in the classification. All sleep stage labels were provided as classification labels for creating this

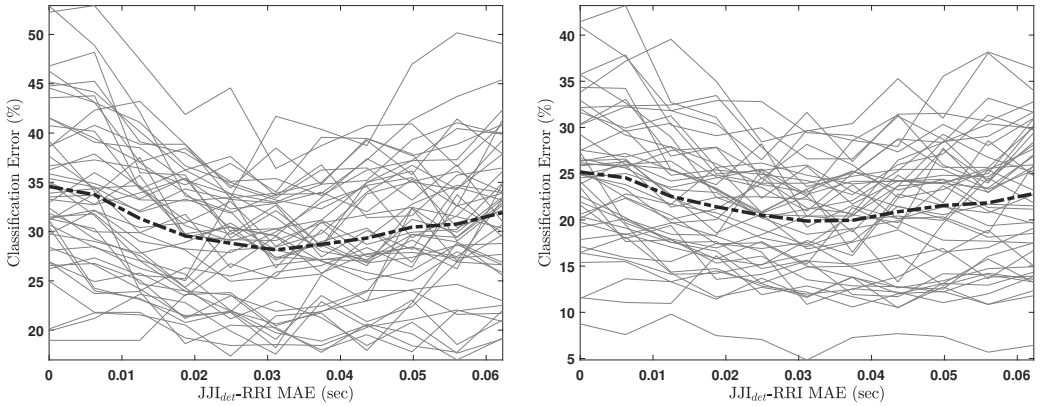

(a) (b)

Figure 5.7: KNN classification error due to all HRV features when: (a) All sleep stage labels were present, (b) Non-REM sleep stages were merged.

plot. Panel *b* of Fig. 5.10, on the other hand, shows classification error between REM and N-REM stages where the sleep stages not belonging to the REM stage were given a single label, i.e., N-REM. In both cases all HRV features were provided to the classifier.

The panels of Fig. 5.11 show SVM classification error due to individual HRV features used one at a time during the classification. All sleep stage labels were provided as classification labels for creating these plots.

Finally, the plots in Fig. 5.12 show SVM classification errors due to individual HRV features used one at a time for classifying REM and N-REM sleep stages. Again, non-REM sleep stage labels were modified to a single label representing the N-REM stage in creating the plots.

5.4 Discussion and conclusion

We examined both parametric and non-parametric Bayes error estimates and as well as two classification algorithms. In addition, different sleep stage labeling and HRV feature combination scenarios were tested. As observed from the results, SVM classification when provided with all HRV features and all sleep stage labels, proved to be helpful in finding a limit for JJI$_{det}$-RRI MAE that may result in acceptable sleep staging performance.

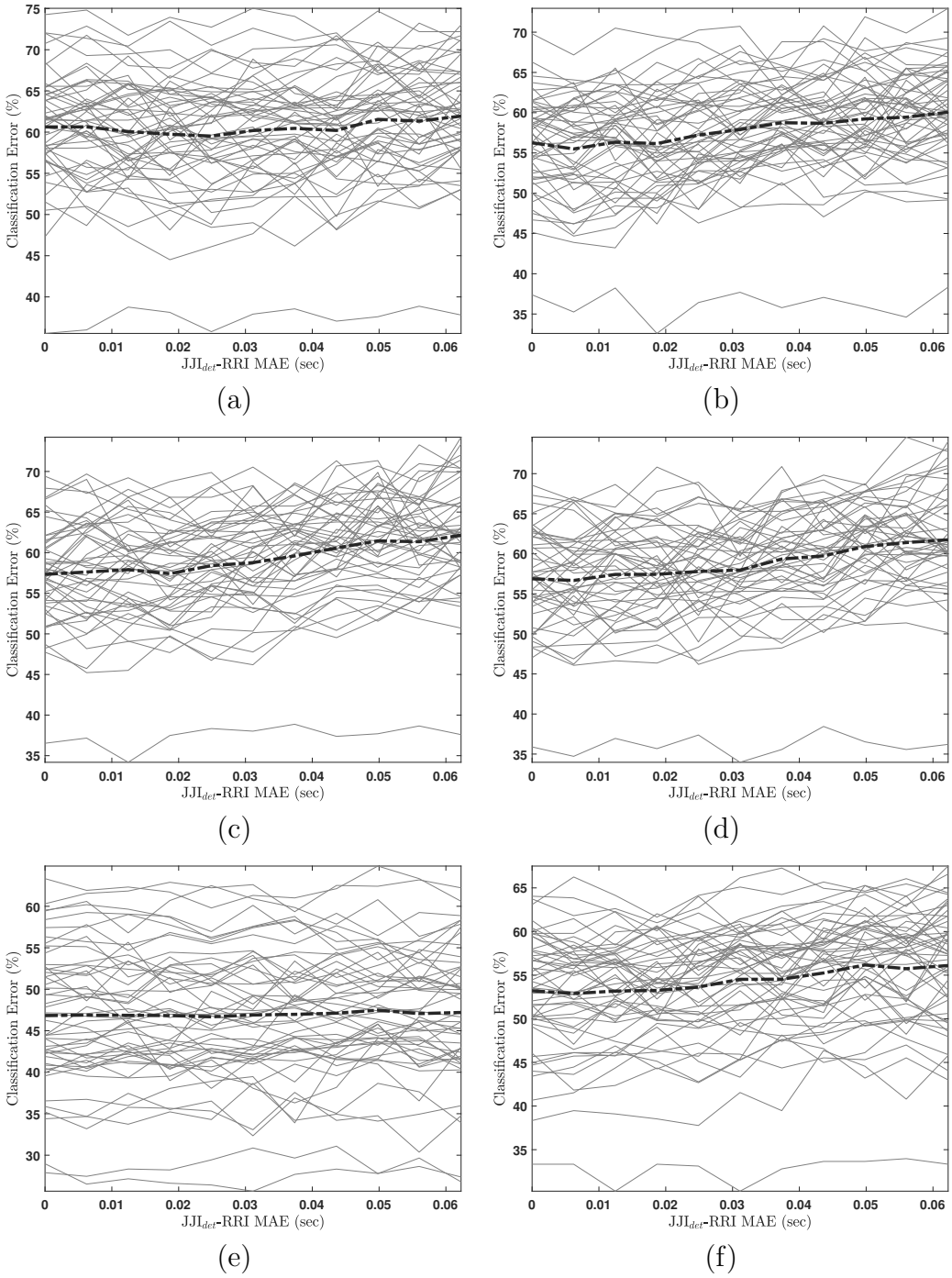

Figure 5.8: KNN classification error across all sleep stages using the HRV features: (a) LF, (b) HF, (c) ratio of LF to HF, (d) median-filtered ratio of LF to HF, (e) HR and (f) SDNN.

If we allow a 20% classification error, we need to limit the JJI$_{det}$-RRI MAE to approximately 30 ms as panel (a) of Fig. 5.10 suggests. The MAE of the HBI obtained using the best performing method identified in Chapter 4 is mostly below 20 ms as seen in the bottom-

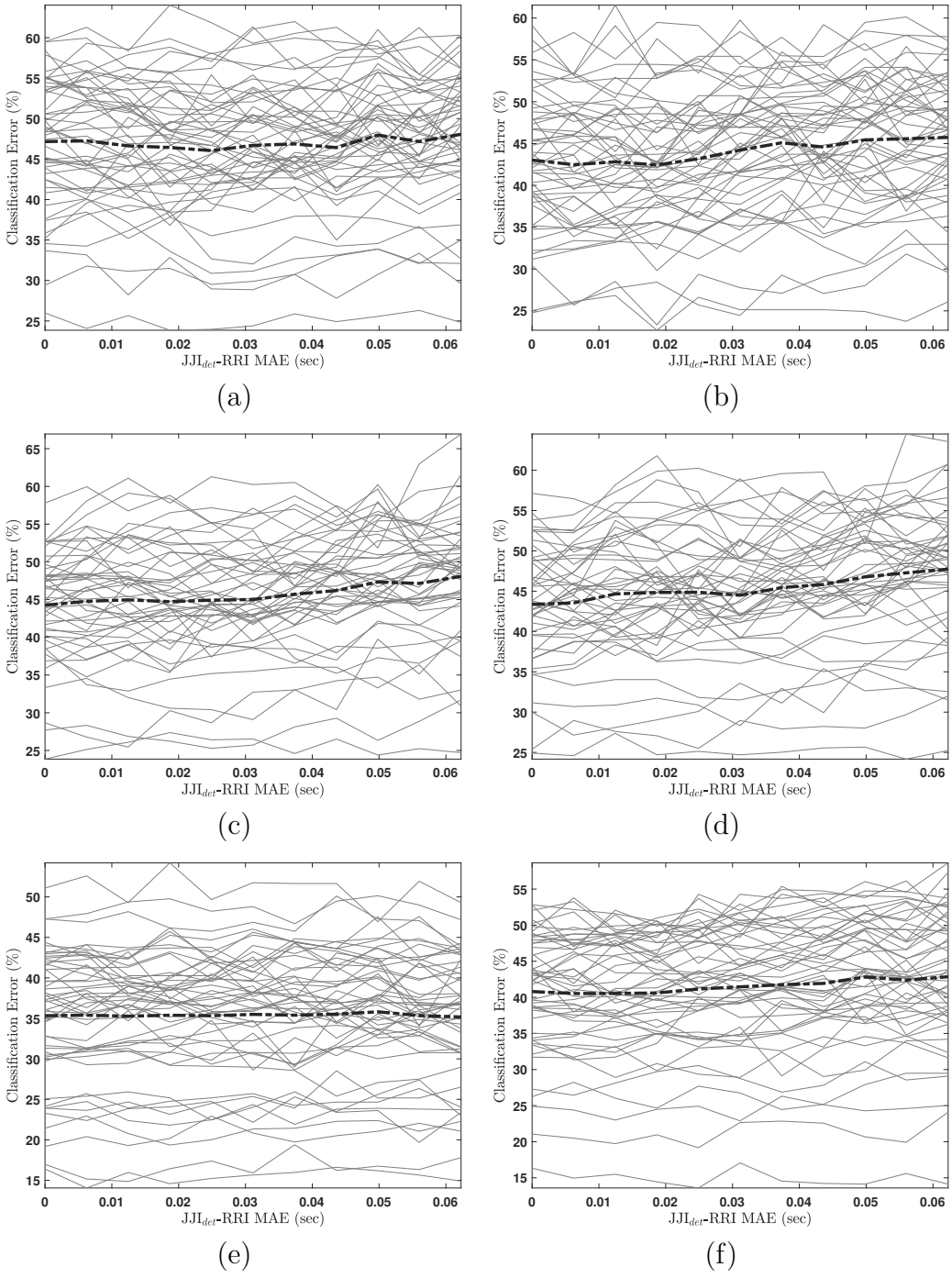

Figure 5.9: KNN classification error across all sleep stages when non-REM sleep stages were merged into a single stage of NREM, using the HRV features: (a) LF, (b) HF, (c) ratio of LF to HF, (d) median-filtered ratio of LF to HF, (e) HR and (f) SDNN.

most panel of Fig. 4.5. In addition, the MAE of JJI$_{GT}$-RRI was calculated to be 8.8 ms. Therefore, the combination of both MAEs is still below the limit identified in this chapter

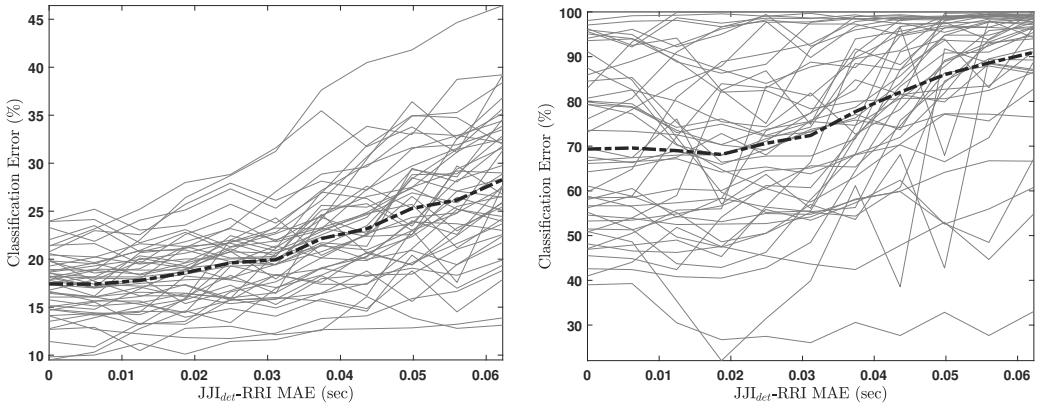

Figure 5.10: SVM classification error due to all HRV features when: (a) All sleep stage labels were present, (b) Non-REM sleep stages were merged.

(30ms). This comparison suggests that the system and methods presented in this dissertation are ready for BCG-based health monitoring studies and in particular sleep quality assessment.

Two main scenarios were examined in the study; (*i*) preserving all sleep stage labels as separate labels when provided to the classifier (Fig. 5.8 and Fig. 5.11); (*ii*) representing non-REM sleep stages as a single N-REM stage (Fig. 5.9 and Fig. 5.12). A comparison of the two scenarios suggests that finer grained sleep staging performance is more sensitive to JJI-RRI error compared to coarse sleep staging performance. In other words, analyzing the sleep microstructure with HRV features is difficult.

The error baseline is high in the plots of Fig. 5.8 and Fig. 5.11. Nonetheless, they assist us in drawing conclusions about sensitivity of quality of certain HRV features to JJI-RRI error. For example, HRV features LF, the ratio of LF to HF and HR are more sensitive to the JJI-RRI error compared to others based on panels *a*, *c* and *e* of the mentioned figures.

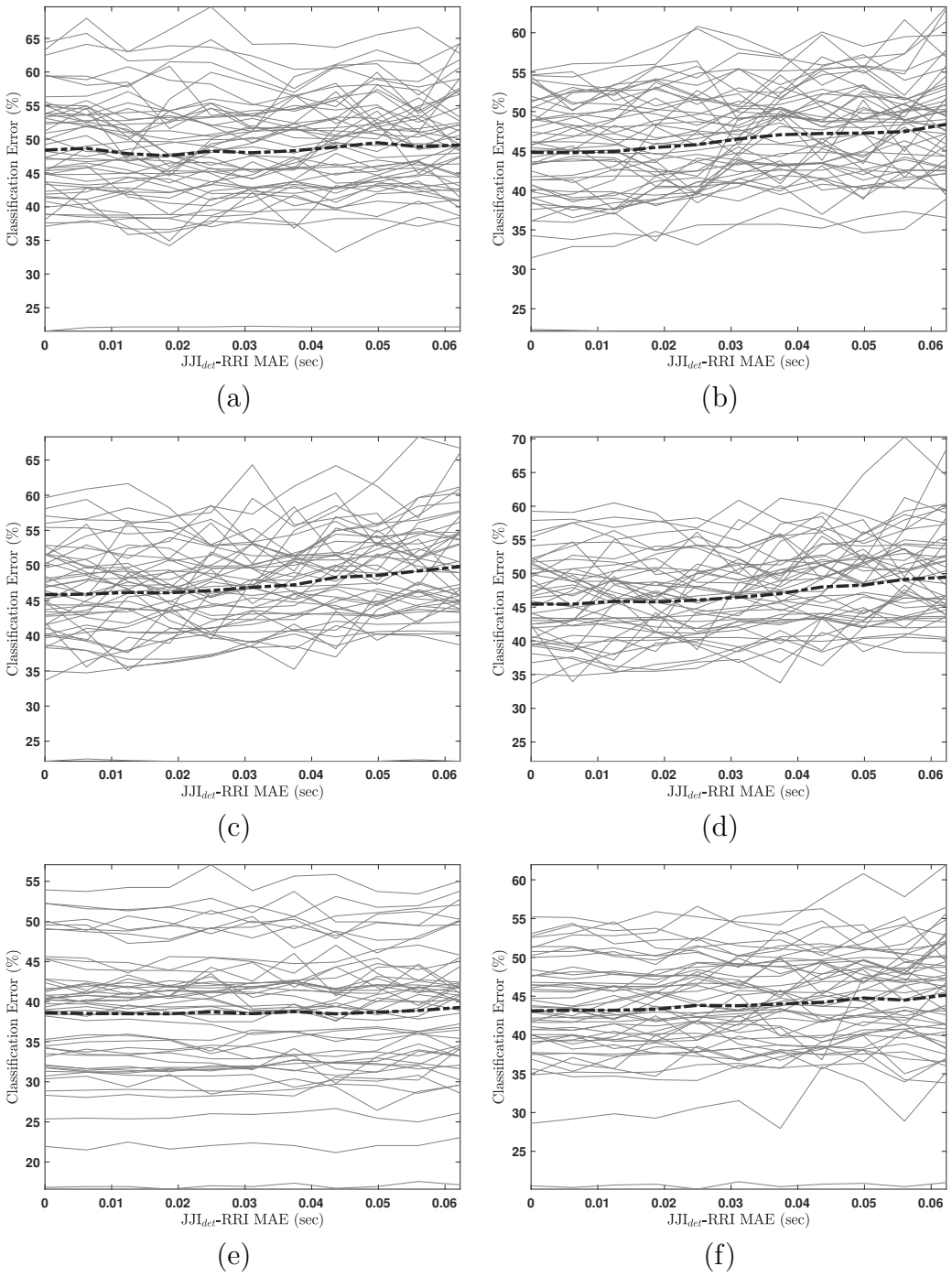

Figure 5.11: SVM classification error across all sleep stages using the HRV features: (a) LF, (b) HF, (c) ratio of LF to HF, (d) median-filtered ratio of LF to HF, (e) HR and (f) SDNN.

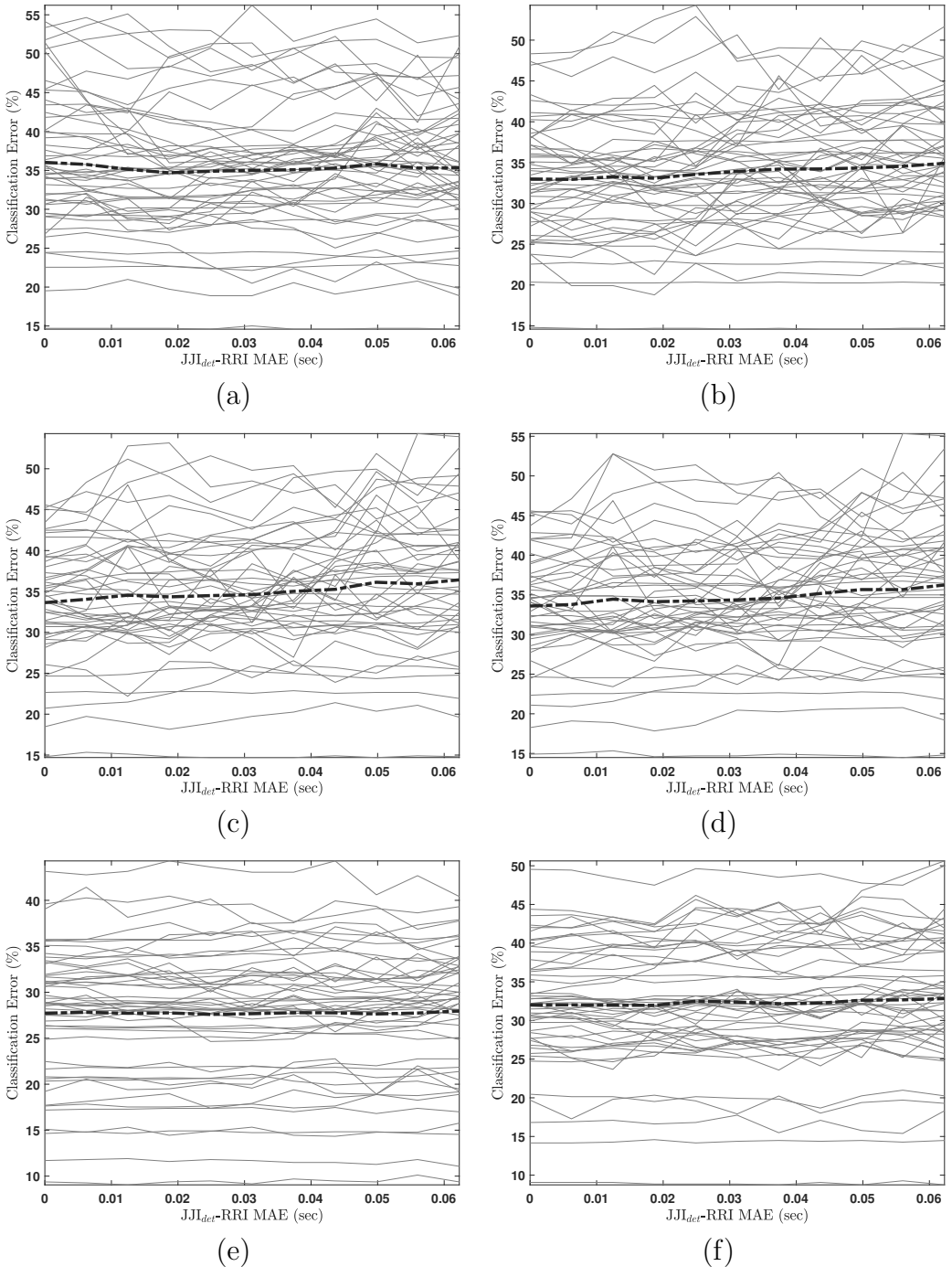

Figure 5.12: SVM classification error across all sleep stages when non-REM sleep stages were merged to a single stage of NREM using the HRV features: (a) LF, (b) HF, (c) ratio of LF to HF, (d) median-filtered ratio of LF to HF, (e) HR and (f) SDNN.

Chapter 6

Conclusions and future work

6.1 Conclusions

This work sheds light on both hardware and signal processing aspects of the challenges encountered in BCG-based HRV estimation. A summary of the contributions from each chapter follows.

Together, chapters 2 and 3 enabled us to design a multi-sensor, remotely accessible BCG bed system. Chapter 2 enabled the objective selection of the data acquisition configuration; Chapter 3 enabled the selection of a load cell for better BCG detection. Lessons learned from the experiments in the course of testing different data acquisition configurations and load cells were invaluable in the following experiments.

Chapter 4 is the first objective comparison of different BCG peak detection methods. In addition to suggesting a method for our laboratory's use, Chapter 4 identifies a baseline of performance for future BCG peak detection algorithms. In addition, this chapter establishes a platform for a performance comparison of BCG peak detection methods which can be extended to other non-contact methods for heartbeat detection.

The observations from Chapter 5 suggest that a long-term health monitoring system with sleep quality assessment capability using BCG is possible. The main contribution of the chapter is the identification of acceptable range of HBI error for useful HRV feature

extraction. Notably, the HBI error due to the hardware and BCG peak detection of our system is within the acceptable HBI error range, indicating that the system is ready for use in long-term, longitudinal studies.

6.2 Future work

As most of the error plots in Chapter 5 suggest, there is a relatively high error baseline in sleep staging accuracy even with clean R-peaks. Therefore, as pursued by other research groups, the inclusion of other physiological data such as breathing and motion information may be worthwhile. We expect to improve the performance of sleep staging by adding such information.

At the beginning of this dissertation, other health-related applications of HRV were mentioned. While ECG-based studies are currently ongoing in these application spaces, BCG-based HRV estimation has remained limited to sleep quality assessment in general. It might be interesting to learn more about the capabilities of BCG in these domains as well.

As pointed out in Chapter 4, the performance of the methods introduced heavily depend on subject-dependent parameters. Those parameters can be fine-tuned and personalized if longitudinal studies of BCG peak detection were conducted. The system and methods described in this dissertation could help plan and execute such studies.

For long-term BCG recordings, remotely accessible and compact systems are needed. In order to address human dignity and privacy issues, it is also necessary to provide control over the system to the user. Due to the fact that the system resides in a home environment, inconveniences due to repeated visits for data gathering, system maintenance and fault mitigation should be minimized if cannot be avoided altogether. For that reason and in particular for data gathering, the trending practice is to conduct remote data collection. For this purpose, the flexibility provided by cloud based services is ideal. The data acquisition hardware described in this dissertation can be modified to address these requirements and be deployed for home-based long-term health monitoring. Initial steps toward this direction in terms of hardware modifications, current status and the limitations are discussed in detail

in Appendix B.

Bibliography

[1] Emi Yuda, Yutaka Yoshida, Ryujiro Sasanabe, Haruhito Tanaka, Toshiaki Shiomi, and Junichiro Hayano. Sleep stage classification by a combination of actigraphic and heart rate signals. *Journal of Low Power Electronics and Applications*, 7(4):28, 2017.

[2] Junichiro Hayano, Emi Yuda, and Yutaka Yoshida. Sleep stage classification by combination of actigraphic and heart rate signals. In *Consumer Electronics-Taiwan (ICCE-TW), 2017 IEEE International Conference on*, pages 387–388. IEEE, 2017.

[3] Sami Nurmi, Tarja Saaresranta, Tero Koivisto, Ulf Merihein, and Lauri Palva. *Validation of an Accelerometer Based BCG Method for Sleep Analysis*. Aalto University, 2016. ISBN 978-952-60-6842-8. URL https://aaltodoc.aalto.fi:443/handle/123456789/21176.

[4] Hongbo Ni, Tingzhi Zhao, Xingshe Zhou, Zhu Wang, Lei Chen, and Jun Yang. Analyzing Sleep Stages in Home Environment Based on Ballistocardiography. In Xiaoxia Yin, Kendall Ho, Daniel Zeng, Uwe Aickelin, Rui Zhou, and Hua Wang, editors, *Health Information Science*, number 9085 in Lecture Notes in Computer Science, pages 56–68. Springer International Publishing, May 2015. ISBN 978-3-319-19155-3 978-3-319-19156-0. URL http://link.springer.com/chapter/10.1007/978-3-319-19156-0_7. DOI: 10.1007/978-3-319-19156-0_7.

[5] Meng Xiao, Hong Yan, Jinzhong Song, Yuzhou Yang, and Xianglin Yang. Sleep stages classification based on heart rate variability and random forest. *Biomedical Signal Processing and Control*, 8(6):624–633, November 2013. ISSN 1746-8094. doi: 10.1016/j.bspc.2013.06.001. URL http://www.sciencedirect.com/science/article/pii/S1746809413000864.

[6] Zhao Dong, Xiang Li, and Wei Chen. Frequency-network analysis of heart rate variability for obstructive apnea patient detection. *IEEE Journal of Biomedical and Health Informatics*, 2017.

[7] Da Woon Jung, Su Hwan Hwang, Hee Nam Yoon, Y.-J.G. Lee, Do-Un Jeong, and Kwang Suk Park. Nocturnal Awakening and Sleep Efficiency Estimation Using Unobtrusively Measured Ballistocardiogram. *IEEE Transactions on Biomedical Engineering*, 61(1):131–138, January 2014. ISSN 0018-9294. doi: 10.1109/TBME.2013.2278020.

[8] Claudia Arab, Luiz Carlos Marques Vanderlei, Laércio da Silva Paiva, Kyle Levi Fulghum, Carlos Elias Fristachi, Afonso Celso Pinto Nazario, Simone Elias, Luiz Henrique Gebrim, Celso Ferreira Filho, Yori Gidron, et al. Cardiac autonomic modulation impairments in advanced breast cancer patients. *Clinical Research in Cardiology*, pages 1–13, 2018.

[9] Kajsa Boman. Heart rate variability: A possible measure of subjective wellbeing?, 2018.

[10] Task Force of the European Society of Cardiology the North American Society of Pacing Electrophysiology. Heart rate variability. *Circulation*, 93(5):1043–1065, 1996. doi: 10.1161/01.CIR.93.5.1043. URL https://www.ahajournals.org/doi/abs/10.1161/01.CIR.93.5.1043.

[11] Konstantinos Georgiou, Andreas V Larentzakis, Nehal N Khamis, Ghadah I Alsuhaibani, Yasser A Alaska, and Elias J Giallafos. Can wearable devices accurately measure heart rate variability? a systematic review. *Folia medica*, 60(1):7–20, 2018.

[12] Isabelle Nault, Philippe André, Benoit Plourde, François Leclerc, Jean-François Sarrazin, François Philippon, Gilles O'Hara, Franck Molin, Christian Steinberg, Karine Roy, et al. Validation of a novel single lead ambulatory ecg monitor–cardiostat–compared to a standard ecg holter monitoring. *Journal of electrocardiology*, 53:57–63, 2019.

[13] An-Bang Liu, Hsien-Tsai Wu, Cyuan-Cin Liu, Chun-Hsiang Hsu, and Ding-Yuan Chen. The factors influence compatibility of pulse-pulse intervals with rr intervals. In *2013 35th Annual International Conference of the IEEE Engineering in Medicine and Biology Society (EMBC)*, pages 2068–2071. IEEE, 2013.

[14] Matthias Daniel Zink, Christoph Brüser, Björn-Ole Stüben, Andreas Napp, Robert Stöhr, Steffen Leonhardt, Nikolaus Marx, Karl Mischke, Jörg B Schulz, and Johannes Schiefer. Unobtrusive nocturnal heartbeat monitoring by a ballistocardiographic sensor in patients with sleep disordered breathing. *Scientific Reports*, 7:13175, 2017.

[15] Won Kyu Lee, Heenam Yoon, Chungmin Han, Kwang Min Joo, and Kwang Suk Park. Physiological Signal Monitoring Bed for Infants Based on Load-Cell Sensors. *Sensors*, 16(3):409, March 2016. doi: 10.3390/s16030409. URL http://www.mdpi.com/1424-8220/16/3/409.

[16] Joonas Paalasmaa, Hannu Toivonen, and Markku Partinen. Adaptive heartbeat modeling for beat-to-beat heart rate measurement in ballistocardiograms. *IEEE journal of biomedical and health informatics*, 19(6):1945–1952, 2015.

[17] C Brüser, S Winter, and S Leonhardt. Robust inter-beat interval estimation in cardiac vibration signals. *Physiological measurement*, 34(2):123, 2013.

[18] Christoph Brueser, Stefan Winter, and Steffen Leonhardt. Unsupervised heart rate variability estimation from ballistocardiograms. In *proceedings of the 7th International Workshop on Biosignal Interpretation*, 2012.

[19] C. Brüser, K. Stadlthanner, S. de Waele, and S. Leonhardt. Adaptive Beat-to-Beat Heart Rate Estimation in Ballistocardiograms. *IEEE Transactions on Information Technology in Biomedicine*, 15(5):778–786, September 2011. ISSN 1089-7771. doi: 10.1109/TITB.2011.2128337.

[20] Jae Hyuk Shin, Su Hwan Hwang, Min Hye Chang, and Kwang Suk Park. Heart rate

variability analysis using a ballistocardiogram during valsalva manoeuvre and post exercise. *Physiological measurement*, 32(8):1239, 2011.

[21] Juha M Kortelainen and Jussi Virkkala. Fft averaging of multichannel bcg signals from bed mattress sensor to improve estimation of heart beat interval. In *Engineering in Medicine and Biology Society, 2007. EMBS 2007. 29th Annual International Conference of the IEEE*, pages 6685–6688. IEEE, 2007.

[22] Xiaoce Feng, Yong Xu, Ming Dong, and Philip Levy. Non-contact home health monitoring based on low-cost high-performance accelerometers. In *Proceedings of the Second IEEE/ACM International Conference on Connected Health: Applications, Systems and Engineering Technologies*, pages 356–364. IEEE Press, 2017.

[23] Punit Prakash, Phillip Kuehl, Brogan McWilliams, Steve Rubenthaler, Emily Schnell, Gary Singleton, and Steve Warren. Sensors and instrumentation for unobtrusive sleep quality assessment in autistic children. In *2014 36th Annual International Conference of the IEEE Engineering in Medicine and Biology Society*, pages 800–803. IEEE, 2014.

[24] Steve Warren, P Prakash, E Brokesh, GW Singleton, and K Fowler. Design projects to quantify the health and development of autistic children. In *2014 Annual Conference & Exposition, American Society for Engineering Education*, pages 15–18, 2014.

[25] Charles Carlson, Ahmad Suliman, Punit Prakash, David Thompson, Shangxian Wang, Bala Natarajan, and Steve Warren. Bed-based instrumentation for unobtrusive sleep quality assessment in severely disabled autistic children. In *Engineering in Medicine and Biology Society (EMBC), 2016 IEEE 38th Annual International Conference of the*, pages 4909–4912. IEEE, 2016.

[26] Charles Carlson, Ahmad Suliman, Alaleh Alivar, Punit Prakash, David Thompson, Balasubramaniam Natarajan, and Steve Warren. A pilot study of an unobtrusive bed-based sleep quality monitor for severely disabled autistic children. In *2018 40th*

Annual International Conference of the IEEE Engineering in Medicine and Biology Society (EMBC), pages 4343–4346. IEEE, 2018.

[27] Charles Carlson. *Development of a Bed-Based Nighttime Monitoring Toolset*. PhD thesis, KSU, 2019.

[28] Daniel Austin, Zachary T Beattie, Thomas Riley, Adriana M Adami, Chad C Hagen, and Tamara L Hayes. Unobtrusive classification of sleep and wakefulness using load cells under the bed. In *Engineering in Medicine and Biology Society (EMBC), 2012 Annual International Conference of the IEEE*, pages 5254–5257. IEEE, 2012.

[29] Hong Ji Lee, Seung Min Lee, Kang Moo Lee, and Kwang Suk Park. Performance evaluation of electrocardiogram measured using capacitive textiles on a bed. In *BIODEVICES*, pages 436–439, 2011.

[30] Kin-fai Wu and Yuan-ting Zhang. Contactless and continuous monitoring of heart electric activities through clothes on a sleeping bed. In *Information Technology and Applications in Biomedicine, 2008. ITAB 2008. International Conference on*, pages 282–285. IEEE, 2008.

[31] Yong Gyu Lim, Ko Keun Kim, and Kwang Suk Park. Ecg recording on a bed during sleep without direct skin-contact. *IEEE Transactions on Biomedical Engineering*, 54 (4):718–725, 2007.

[32] Yong Gyu Lim, Ki Hwan Hong, Ko Keun Kim, Jae Hyuk Shin, Seung Min Lee, Gih Sung Chung, Hyun Jae Baek, Do-Un Jeong, and Kwang Suk Park. Monitoring physiological signals using nonintrusive sensors installed in daily life equipment. *Biomedical engineering letters*, 1(1):11–20, 2011.

[33] Masa Ishijima. Monitoring of electrocardiograms in bed without utilizing body surface electrodes. *IEEE Transactions on Biomedical Engineering*, 40(6):593–594, 1993.

[34] Bhavin Chamadiya, Kunal Mankodiya, Manfred Wagner, and Ulrich G Hofmann.

Textile-based, contactless ecg monitoring for non-icu clinical settings. *Journal of Ambient Intelligence and Humanized Computing*, 4(6):791–800, 2013.

[35] Mico Yee Man Wong, Emma Pickwell-MacPherson, and YT Zhang. Contactless and continuous monitoring of heart rate based on photoplethysmography on a mattress. *Physiological measurement*, 31(7):1065, 2010.

[36] Kenneth Humphreys, Tomas Ward, and Charles Markham. Noncontact simultaneous dual wavelength photoplethysmography: a further step toward noncontact pulse oximetry. *Review of scientific instruments*, 78(4):044304, 2007.

[37] Sun Yu, Sijung Hu, Vicente Azorin-Peris, Jonathon A Chambers, Yisheng Zhu, and Stephen E Greenwald. Motion-compensated noncontact imaging photoplethysmography to monitor cardiorespiratory status during exercise. *Journal of biomedical optics*, 16(7):077010, 2011.

[38] Ming-Zher Poh, Daniel J McDuff, and Rosalind W Picard. Non-contact, automated cardiac pulse measurements using video imaging and blind source separation. *Optics express*, 18(10):10762–10774, 2010.

[39] Ming-Zher Poh, Daniel J McDuff, and Rosalind W Picard. Advancements in noncontact, multiparameter physiological measurements using a webcam. *IEEE transactions on biomedical engineering*, 58(1):7–11, 2011.

[40] Lingqin Kong, Yuejin Zhao, Liquan Dong, Yiyun Jian, Xiaoli Jin, Bing Li, Yun Feng, Ming Liu, Xiaohua Liu, and Hong Wu. Non-contact detection of oxygen saturation based on visible light imaging device using ambient light. *Optics express*, 21(15): 17464–17471, 2013.

[41] Ubiratan S Freitas. Remote camera-based pulse oximetry. In *eTELEMED 2014, The Sixth International Conference on eHealth, Telemedicine, and Social Medicine*, pages 59–63. Citeseer, 2014.

[42] Sumit Majumder, Leon Chen, Ognian Marinov, Chih-Hung Chen, Tapas Monday, and M Jamal Deen. Non-contact wearable wireless ecg systems for long term monitoring. *IEEE Reviews in Biomedical Engineering*, 2018.

[43] Amy Droitcour, Victor Lubecke, Jenshan Lin, and Olga Boric-Lubecke. A microwave radio for doppler radar sensing of vital signs. In *Microwave Symposium Digest, 2001 IEEE MTT-S International*, volume 1, pages 175–178. IEEE, 2001.

[44] MYW Chia, SW Leong, CK Sim, and KM Chan. Through-wall uwb radar operating within fcc's mask for sensing heart beat and breathing rate. In *Radar Conference, 2005. EURAD 2005. European*, pages 267–270. IEEE, 2005.

[45] Yanming Xiao, Jenshan Lin, Olga Boric-Lubecke, and M Lubecke. Frequency-tuning technique for remote detection of heartbeat and respiration using low-power double-sideband transmission in the ka-band. *IEEE Transactions on Microwave Theory and Techniques*, 54(5):2023–2032, 2006.

[46] Hyoung Jong Kim, Ki Ho Kim, Yun Seok Hong, and Jin Joo Choi. Measurement of human heartbeat and respiration signals using phase detection radar. *Review of Scientific Instruments*, 78(10):104703, 2007.

[47] M Varanini, PC Berardi, F Conforti, M Micalizzi, D Neglia, and ALBERTO Macerata. Cardiac and respiratory monitoring through non-invasive and contactless radar technique. In *Computers in Cardiology, 2008*, pages 149–152. IEEE, 2008.

[48] K Mostov, E Liptsen, and R Boutchko. Medical applications of shortwave fm radar: Remote monitoring of cardiac and respiratory motion. *Medical physics*, 37(3):1332–1338, 2010.

[49] Ilya V Mikhelson, Sasan Bakhtiari, Thomas W Elmer, Alan V Sahakian, et al. Remote sensing of heart rate and patterns of respiration on a stationary subject using 94-ghz millimeter-wave interferometry. *IEEE Transactions on Biomedical Engineering*, 58(6): 1671–1677, 2011.

[50] Tsung-Hsin Liu, Miao-Lin Hsu, and Zuo-Min Tsai. High ranging accuracy and wide detection range interferometry based on frequency-sweeping technique with vital sign sensing function. *IEEE Transactions on Microwave Theory and Techniques*, (99):1–10, 2018.

[51] Antonio Lazaro, David Girbau, and Ramon Villarino. Analysis of vital signs monitoring using an ir-uwb radar. *Progress In Electromagnetics Research*, 100:265–284, 2010.

[52] Gabor Vinci, Stefan Lindner, Francesco Barbon, Sebastian Mann, Maximilian Hofmann, Alexander Duda, Robert Weigel, and Alexander Koelpin. Six-port radar sensor for remote respiration rate and heartbeat vital-sign monitoring. *IEEE Transactions on Microwave Theory and Techniques*, 61(5):2093–2100, 2013.

[53] Øyvind Aardal, Yoann Paichard, Sverre Brovoll, Tor Berger, Tor Sverre Lande, and Svein-Erik Hamran. Physical working principles of medical radar. *IEEE Transactions on Biomedical Engineering*, 60(4):1142–1149, 2013.

[54] Fadel Adib, Hongzi Mao, Zachary Kabelac, Dina Katabi, and Robert C Miller. Smart homes that monitor breathing and heart rate. In *Proceedings of the 33rd annual ACM conference on human factors in computing systems*, pages 837–846. ACM, 2015.

[55] Heng Zhao, Hong Hong, Li Sun, Yusheng Li, Changzhi Li, and Xiaohua Zhu. Noncontact physiological dynamics detection using low-power digital-if doppler radar. *IEEE Transactions on Instrumentation and Measurement*, 66(7):1780–1788, 2017.

[56] Adeel Ahmad, June Chul Roh, Dan Wang, and Aish Dubey. Vital signs monitoring of multiple people using a fmcw millimeter-wave sensor. In *Radar Conference (RadarConf18), 2018 IEEE*, pages 1450–1455. IEEE, 2018.

[57] AE Aubert, L Welkenhuysen, J Montald, L De Wolf, H Geivers, J Minten, Hugo Kesteloot, and H Geest. Laser method for recording displacement of the heart and chest wall. *Medical Engineering and Physics*, 6(2):134–140, 1984.

[58] HyunDae Hong and Martin D Fox. Noninvasive detection of cardiovascular pulsations by optical doppler techniques. *Journal of Biomedical optics*, 2(4):382–391, 1997.

[59] Chen-Chia Wang, Sudhir B Trivedi, Feng Jin, Serguei Stepanov, Zhongyang Chen, Jacob Khurgin, Ponciano Rodriguez, and Narasimha S Prasad. Human life signs detection using high-sensitivity pulsed laser vibrometer. *IEEE Sensors Journal*, 7(9): 1370–1376, 2007.

[60] Sara Casaccia, Erik J Sirevaag, Edward Richter, Joseph A O'Sullivan, Lorenzo Scalise, and John W Rohrbaugh. Decoding carotid pressure waveforms recorded by laser doppler vibrometry: Effects of rebreathing. In *AIP Conference Proceedings*, volume 1600, pages 298–312. AIP, 2014.

[61] Sara Casaccia. *Measurement of physiological parameters in the human body by non-contact technique: Laser Doppler Vibrometry.* PhD thesis, Universitá Politecnica delle Marche, 2015.

[62] Umberto Morbiducci, Lorenzo Scalise, Mirko De Melis, and Mauro Grigioni. Optical vibrocardiography: a novel tool for the optical monitoring of cardiac activity. *Annals of biomedical engineering*, 35(1):45–58, 2007.

[63] Ali Al-Naji, Kim Gibson, Sang-Heon Lee, and Javaan Chahl. Monitoring of cardiorespiratory signal: principles of remote measurements and review of methods. *IEEE Access*, 5:15776–15790, 2017.

[64] Jure Kranjec, S Beguš, G Geršak, and J Drnovšek. Non-contact heart rate and heart rate variability measurements: A review. *Biomedical Signal Processing and Control*, 13:102–112, 2014.

[65] Christoph Brüser, Anna Kerekes, Stefan Winter, and Steffen Leonhardt. Multi-channel optical sensor-array for measuring ballistocardiograms and respiratory activity in bed. In *Engineering in Medicine and Biology Society (EMBC), 2012 Annual International Conference of the IEEE*, pages 5042–5045. IEEE, 2012.

[66] Hiromichi Maki, Hidekuni Ogawa, Sosuke Tsukamoto, Yoshiharu Yonezawa, and W Morton Caldwell. A system for monitoring cardiac vibration, respiration, and body movement in bed using an infrared. In *Engineering in Medicine and Biology Society (EMBC), 2010 Annual International Conference of the IEEE*, pages 5197–5200. IEEE, 2010.

[67] Daphne Townsend, Rafik Goubran, Frank Knoefel, and Judith Leech. Validation of unobtrusive pressure sensor array for central sleep apnea screening. *IEEE Transactions on Instrumentation and Measurement*, 61(7):1857–1865, 2012.

[68] Ibrahim Sadek, Jit Biswas, Bessam Abdulrazak, Zhang Haihong, and Mounir Mokhtari. Continuous and unconstrained vital signs monitoring with ballistocardiogram sensors in headrest position. In *Biomedical & Health Informatics (BHI), 2017 IEEE EMBS International Conference on*, pages 289–292. IEEE, 2017.

[69] Hiroshi Kimura, Hisato Kobayashi, Kuniaki Kawabata, and HF Van der Loos. Development of an unobtrusive vital signs detection system using conductive fiber sensors. In *Intelligent Robots and Systems, 2004.(IROS 2004). Proceedings. 2004 IEEE/RSJ International Conference on*, volume 1, pages 307–312. IEEE, 2004.

[70] Yusuke Yamana, Sosuke Tsukamoto, Koji Mukai, Hiromichi Maki, Hidekuni Ogawa, and Yoshiharu Yonezawa. A sensor for monitoring pulse rate, respiration rhythm, and body movement in bed. In *Engineering in Medicine and Biology Society, EMBC, 2011 Annual International Conference of the IEEE*, pages 5323–5326. IEEE, 2011.

[71] Ben H Jansen, B Hans Larson, and Kris Shankar. Monitoring of the ballistocardiogram with the static charge sensitive bed. *IEEE Transactions on Biomedical Engineering*, 38(8):748–751, 1991.

[72] J Alihanka, K Vaahtoranta, and I Saarikivi. A new method for long-term monitoring of the ballistocardiogram, heart rate, and respiration. *American Journal of Physiology-Regulatory, Integrative and Comparative Physiology*, 240(5):R384–R392, 1981.

[73] Satu Rajala, Teemu Ahmaniemi, Harri Lindholm, Kiti Müller, and Tapio Taipalus. A chair based ballistocardiogram time interval measurement with cardiovascular provocations. In *2018 40th Annual International Conference of the IEEE Engineering in Medicine and Biology Society (EMBC)*, pages 5685–5688. IEEE, 2018.

[74] Ziran He, Min Wang, Qingsong Xie, Guoxing Wang, Yang Zhao, Yong Lian, Bo Meng, and Zhengchun Peng. A heart rate measurement system based on ballistocardiogram for smart furniture. In *2018 IEEE Asia Pacific Conference on Circuits and Systems (APCCAS)*, pages 151–154. IEEE, 2018.

[75] Kwang Jin Lee, Jongryun Roh, Dongrae Cho, Joonho Hyeong, and Sayup Kim. A chair-based unconstrained/nonintrusive cuffless blood pressure monitoring system using a two-channel ballistocardiogram. *Sensors*, 19(3):595, 2019.

[76] WB SpillmanJr, M Mayer, J Bennett, J Gong, KE Meissner, B Davis, RO Claus, AA MuelenaerJr, and X Xu. A 'smart'bed for non-intrusive monitoring of patient physiological factors. *Measurement Science and Technology*, 15(8):1614, 2004.

[77] Sebastijan Šprager and Damjan Zazula. Heartbeat and respiration detection from optical interferometric signals by using a multimethod approach. *IEEE transactions on biomedical engineering*, 59(10):2922–2929, 2012.

[78] Yongjoon Chee, Jooman Han, Jaewoong Youn, and Kwangsuk Park. Air mattress sensor system with balancing tube for unconstrained measurement of respiration and heart beat movements. *Physiological measurement*, 26(4):413, 2005.

[79] Kajiro Watanabe, Takashi Watanabe, Harumi Watanabe, Hisanori Ando, Takayuki Ishikawa, and Keita Kobayashi. Noninvasive measurement of heartbeat, respiration, snoring and body movements of a subject in bed via a pneumatic method. *IEEE transactions on biomedical engineering*, 52(12):2100–2107, 2005.

[80] David C Mack, James T Patrie, Paul M Suratt, Robin A Felder, and Majd Alwan. Development and preliminary validation of heart rate and breathing rate detection using

a passive, ballistocardiography-based sleep monitoring system. *IEEE Transactions on Information Technology in Biomedicine*, 13(1):111–120, 2009.

[81] Kajiro Watanabe, Yosuke Kurihara, and Hiroshi Tanaka. Ubiquitous health monitoring at home–sensing of human biosignals on flooring, on tatami mat, in the bathtub, and in the lavatory. *IEEE Sensors Journal*, 9(12):1847–1855, 2009.

[82] K. Lydon, B. Y. Su, L. Rosales, M. Enayati, K. C. Ho, M. Rantz, and M. Skubic. Robust heartbeat detection from in-home ballistocardiogram signals of older adults using a bed sensor. In *2015 37th Annual International Conference of the IEEE Engineering in Medicine and Biology Society (EMBC)*, pages 7175–7179, August 2015. doi: 10.1109/EMBC.2015.7320047.

[83] Licet Rosales, Marjorie Skubic, David Heise, Michael J Devaney, and Mark Schaumburg. Heartbeat detection from a hydraulic bed sensor using a clustering approach. In *Engineering in Medicine and Biology Society (EMBC), 2012 Annual International Conference of the IEEE*, pages 2383–2387. IEEE, 2012.

[84] Juha M Kortelainen, Martin O Mendez, Anna Maria Bianchi, Matteo Matteucci, and Sergio Cerutti. Sleep staging based on signals acquired through bed sensor. *IEEE Transactions on Information Technology in Biomedicine*, 14(3):776–785, 2010.

[85] Christoph Bruser, Jasper Diesel, Matthias DH Zink, Stefan Winter, Patrick Schauerte, and Steffen Leonhardt. Automatic detection of atrial fibrillation in cardiac vibration signals. *IEEE Journal of Biomedical and health informatics*, 17(1):162–171, 2013.

[86] Kyuichi Niizeki, Izumi Nishidate, K Uchida, and M Kuwahara. Unconstrained cardiorespiratory and body movement monitoring system for home care. *Medical and Biological Engineering and Computing*, 43(6):716–724, 2005.

[87] Feng Wang, Mami Tanaka, and Seiji Chonan. Development of a pvdf piezopolymer sensor for unconstrained in-sleep cardiorespiratory monitoring. *Journal of intelligent material systems and structures*, 14(3):185–190, 2003.

[88] Su Hwan Hwang, Hee Nam Yoon, Yu-Jin G Lee, Do-Un Jeong, Kwang Suk Park, et al. Nocturnal awakening and sleep efficiency estimation using unobtrusively measured ballistocardiogram. *IEEE transactions on biomedical engineering*, 61(1):131–138, 2014.

[89] Wei Li, Chenglu Sun, Chen Chen, and Wei Chen. Unobtrusive monitoring of cardiorespiratory signals during sleep based on pvdf sensor and singular spectrum analysis. In *2018 IEEE International Instrumentation and Measurement Technology Conference (I2MTC)*. IEEE, 2018.

[90] Gih Sung Chung, Byoung Hoon Choi, Do-Un Jeong, and Kwang Suk Park. Noninvasive heart rate variability analysis using loadcell-installed bed during sleep. In *Engineering in Medicine and Biology Society, 2007. EMBS 2007. 29th Annual International Conference of the IEEE*, pages 2357–2360. IEEE, 2007.

[91] Byung Hun Choi, Gih Sung Chung, Jin-Seong Lee, Do-Un Jeong, and Kwang Suk Park. Slow-wave sleep estimation on a load-cell-installed bed: a non-constrained method. *Physiological measurement*, 30(11):1163, 2009.

[92] A Sivanantham. Measurement of heartbeat, respiration and movements detection using smart bed. In *Intelligent Computational Systems (RAICS), 2015 IEEE Recent Advances in*, pages 105–109. IEEE, 2015.

[93] R Gonzalez-Landaeta, O Casas, and R Pallas-Areny. Heart rate detection from an electronic weighing scale. *Physiological measurement*, 29(8):979, 2008.

[94] OT Inan, M Etemadi, RM Wiard, L Giovangrandi, and GTA Kovacs. Robust ballistocardiogram acquisition for home monitoring. *Physiological measurement*, 30(2):169, 2009.

[95] Mark Brink, Christopher H Müller, and Christoph Schierz. Contact-free measurement of heart rate, respiration rate, and body movements during sleep. *Behavior research methods*, 38(3):511–521, 2006.

[96] Eliran Dafna, Ariel Tarasiuk, and Yaniv Zigel. Sleep staging using nocturnal sound analysis. *Scientific reports*, 8(1):13474, 2018.

[97] Anthony Kales and Allan Rechtschaffen. *A manual of standardized terminology, techniques and scoring system for sleep stages of human subjects*. US Department of Health, Education and Welfare, Public Health Service , 1968.

[98] Richard B Berry, Rita Brooks, Charlene E Gamaldo, Susan M Harding, Carole L Marcus, Bradley V Vaughn, et al. The aasm manual for the scoring of sleep and associated events. *Rules, Terminology and Technical Specifications, Darien, Illinois, American Academy of Sleep Medicine*, 176, 2012.

[99] Richard L Verrier, Ronald M Harper, and Allan J Hobson. Cardiovascular physiology: central and autonomic regulation. 2005.

[100] Ronny P Bartsch, Aicko Y Schumann, Jan W Kantelhardt, Thomas Penzel, and Plamen Ch Ivanov. Phase transitions in physiologic coupling. *Proceedings of the National Academy of Sciences*, 109(26):10181–10186, 2012.

[101] AJMM Camm, Marek Malik, JTGB Bigger, Günter Breithardt, Sergio Cerutti, R Cohen, Philippe Coumel, E Fallen, H Kennedy, RE Kleiger, et al. Heart rate variability: standards of measurement, physiological interpretation and clinical use. task force of the european society of cardiology and the north american society of pacing and electrophysiology. *Circulation*, 93(5):1043–1065, 1996.

[102] Heenam Yoon, Su Hwan Hwang, Jae-Won Choi, Yu Jin Lee, Do-Un Jeong, and Kwang Suk Park. REM sleep estimation based on autonomic dynamics using RR intervals. *Physiol. Meas.*, 38(4):631, 2017. ISSN 0967-3334. doi: 10.1088/1361-6579/aa63c9. URL http://stacks.iop.org/0967-3334/38/i=4/a=631.

[103] Heenam Yoon, Su Hwan Hwang, Jae-Won Choi, Yu Jin Lee, Do-Un Jeong, and Kwang Suk Park. Slow-wave sleep estimation for healthy subjects and osa patients

using r–r intervals. *IEEE journal of biomedical and health informatics*, 22(1):119–128, 2018.

[104] Shing-Tai Pan, Chih-Hung Wu, Chia-Ho Wu, Yung-Ran Lin, and Shie-Jue Lee. Ecg-based automatic sleep staging using hidden markov model. In *International Conference on Smart Vehicular Technology, Transportation, Communication and Applications*, pages 284–291. Springer, 2018.

[105] Keiko Tanida, Masashi Shibata, and Margaret M Heitkemper. Sleep stage assessment using power spectral indices of heart rate variability with a simple algorithm: limitations clarified from preliminary study. *Biological research for nursing*, 15(3):264–272, 2013.

[106] X. Long, P. Fonseca, R. Aarts, R. Haakma, J. Rolink, and S. Leonhardt. Detection of Nocturnal Slow Wave Sleep Based on Cardiorespiratory Activity in Healthy Adults. *IEEE Journal of Biomedical and Health Informatics*, PP(99):1–1, 2016. ISSN 2168-2194. doi: 10.1109/JBHI.2015.2487446.

[107] Pedro Fonseca, Xi Long, Mustafa Radha, Reinder Haakma, Ronald M Aarts, and Jérôme Rolink. Sleep stage classification with ecg and respiratory effort. *Physiological measurement*, 36(10):2027, 2015.

[108] Alaleh Alivar, Charles Carlson, Ahmad Suliman, Steve Warren, Punit Prakash, Dave Thompson, and Balasubramaniam Natarajan. Motion detection in bed-based ballistocardiogram to quantify sleep quality. In *GLOBECOM 2017-2017 IEEE Global Communications Conference*, pages 1–6. IEEE, 2017.

[109] Alaleh Alivar, Charles Carlson, Ahmad Suliman, Steve Warren, Punit Prakash, David E Thompson, and Balasubramaniam Natarajan. Motion artifact detection and reduction in bed-based ballistocardiogram. *IEEE Access*, 2019.

[110] Ahmad Suliman, Charles Carlson, Steve Warren, and David Thompson. Performance evaluation of processing methods for ballistocardiogram peak detection. In *2018 40th*

Annual International Conference of the IEEE Engineering in Medicine and Biology Society (EMBC), pages 502–505. IEEE, 2018.

[111] Ahmad Suliman, Charles Carlson, Carl Ade, Steve Warren, and David E Thompson. Performance comparison for ballistocardiogram peak detection methods. *IEEE Access*, 2019.

[112] Joonas Paalasmaa and Mika Ranta. Detecting heartbeats in the ballistocardiogram with clustering. In *Proceedings of the ICML/UAI/COLT 2008 Workshop on Machine Learning for Health-Care Applications, Helsinki, Finland*, volume 9, 2008.

[113] Satu Rajala and Jukka Lekkala. Film-type sensor materials pvdf and emfi in measurement of cardiorespiratory signalsa review. *IEEE Sensors Journal*, 12(3):439–446, 2012.

[114] Omer T Inan, Pierre-Francois Migeotte, Kwang-Suk Park, Mozziyar Etemadi, Kouhyar Tavakolian, Ramon Casanella, John Zanetti, Jens Tank, Irina Funtova, G Kim Prisk, et al. Ballistocardiography and seismocardiography: A review of recent advances. *IEEE journal of biomedical and health informatics*, 19(4):1414–1427, 2015.

[115] MO Mendez, Matteo Matteucci, Sergio Cerutti, AM Bianchi, and Juha M Kortelainen. Automatic detection of sleep macrostructure based on bed sensors. In *2009 Annual International Conference of the IEEE Engineering in Medicine and Biology Society*, pages 5555–5558. IEEE, 2009.

[116] Gih Sung Chung, Jeong Su Lee, Su Hwan Hwang, Young Kyu Lim, Do-Un Jeong, and Kwang Suk Park. Wakefulness estimation only using ballistocardiogram: Nonintrusive method for sleep monitoring. In *2010 Annual International Conference of the IEEE Engineering in Medicine and Biology*, pages 2459–2462. IEEE, 2010.

[117] Christoph Brüser, Stefan Winter, and Steffen Leonhardt. How speech processing can help with beat-to-beat heart rate estimation in ballistocardiograms. In *Medical Mea-*

surements and Applications Proceedings (MeMeA), 2013 IEEE International Symposium on, pages 12–16. IEEE, 2013.

[118] Antti Vehkaoja, Satu Rajala, Pekka Kumpulainen, and Jukka Lekkala. Correlation approach for the detection of the heartbeat intervals using force sensors placed under the bed posts. *Journal of medical engineering & technology*, 37(5):327–333, 2013.

[119] Yu Yao, Christoph Bruser, Uwe Pietrzyk, Steffen Leonhardt, Stefan van Waasen, and Michael Schiek. Model-based verification of a non-linear separation scheme for ballistocardiography. *IEEE journal of biomedical and health informatics*, 18(1):174–182, 2014.

[120] Yu Yao, J Schiefer, Stefan van Waasen, and Michael Schiek. A non-parametric model for ballistocardiography. In *Statistical Signal Processing (SSP), 2014 IEEE Workshop on*, pages 69–72. IEEE, 2014.

[121] Ibrahim Sadek, Jit Biswas, Victor Foo Siang Fook, and Mounir Mokhtari. Automatic heart rate detection from fbg sensors using sensor fusion and enhanced empirical mode decomposition. In *Signal Processing and Information Technology (ISSPIT), 2015 IEEE International Symposium on*, pages 349–353. IEEE, 2015.

[122] Mariusz Krej, Łukasz Dziuda, and Franciszek Wojciech Skibniewski. A method of detecting heartbeat locations in the ballistocardiographic signal from the fiber-optic vital signs sensor. *IEEE journal of biomedical and health informatics*, 19(4):1443–1450, 2015.

[123] Carlos Alvarado-Serrano, Pablo Samuel Luna-Lozano, and Ramon Pallàs-Areny. An algorithm for beat-to-beat heart rate detection from the bcg based on the continuous spline wavelet transform. *Biomedical Signal Processing and Control*, 27:96–102, 2016.

[124] Ibrahim Sadek, Jit Biswas, Zhu Yongwei, Zhang Haihong, Jayachandran Maniyeri, Chen Zhihao, Teo Ju Teng, Ng Soon Huat, and Mounir Mokhtari. Sensor data quality processing for vital signs with opportunistic ambient sensing. In *Engineering in*

Medicine and Biology Society (EMBC), 2016 IEEE 38th Annual International Conference of the, pages 2484–2487. IEEE, 2016.

[125] Ibrahim Sadek, Joaquim Bellmunt, Martin Kodyš, Bessam Abdulrazak, and Mounir Mokhtari. Novel unobtrusive approach for sleep monitoring using fiber optics in an ambient assisted living platform. In *International Conference on Smart Homes and Health Telematics*, pages 48–60. Springer, 2017.

[126] Licet Rosales Paniagua. *Short-term heart rate variability as a general indicator of health estimated by ballistocardiography using a hydraulic bed sensor in elder care*. PhD thesis, University of Missouri–Columbia, 2016.

[127] Ibrahim Sadek and Jit Biswas. Nonintrusive heart rate measurement using ballistocardiogram signals: a comparative study. *Signal, Image and Video Processing*, pages 1–8, 2018.

[128] A Ozan Bicen and Omer T Inan. A signal quality index for ballistocardiogram recordings based on electrocardiogram rr intervals and matched filtering. In *Biomedical & Health Informatics (BHI), 2018 IEEE EMBS International Conference on*, pages 145–148. IEEE, 2018.

[129] Xianwen Zhang, Liyan Zhang, Kun Wang, Chao Yu, Tiangang Zhu, and Jintian Tang. A rapid approach to assess cardiac contractility by ballistocardiogram and electrocardiogram. *Biomedical Engineering/Biomedizinische Technik*, 2016.

[130] Isaac Starr, AJ Rawson, HA Schroeder, and NR Joseph. Studies on the estimation of cardiac ouptut in man, and of abnormalities in cardiac function, from the heart's recoil and the blood's impacts; the ballistocardiogram. *American Journal of Physiology-Legacy Content*, 127(1):1–28, 1939.

[131] William R Scarborough, Samuel A Talbot, John R Braunstein, Maurice B Rappaport, William Dock, William R Scarborough, WF Hamilton, John E Smith, John L Nickerson, Samuel A Talbot, et al. Proposals for ballistocardiographic nomenclature

and conventions: Revised and extended: Report of committee on ballistocardiographic terminology. *Circulation*, 14(3):435–450, 1956.

[132] Jan S Krouwer. Why bland–altman plots should use x, not (y+ x)/2 when x is a reference method. *Statistics in medicine*, 27(5):778–780, 2008.

[133] C. Brüser, J.M. Kortelainen, S. Winter, M. Tenhunen, J. Parkka, and S. Leonhardt. Improvement of Force-Sensor-Based Heart Rate Estimation Using Multichannel Data Fusion. *IEEE Journal of Biomedical and Health Informatics*, 19(1):227–235, January 2015. ISSN 2168-2194. doi: 10.1109/JBHI.2014.2311582.

[134] Iwao Fujimasa, Tsuneo Chinzei, and Itsuro Saito. Converting far infrared image information to other physiological data. *IEEE Engineering in Medicine and Biology Magazine*, 19(3):71–76, 2000.

[135] Ioannis Pavlidis and James Levine. Thermal image analysis for polygraph testing. *IEEE Engineering in Medicine and Biology Magazine*, 21(6):56–64, 2002.

[136] Marc Garbey, Nanfei Sun, Arcangelo Merla, and Ioannis Pavlidis. Contact-free measurement of cardiac pulse based on the analysis of thermal imagery. *IEEE transactions on Biomedical Engineering*, 54(8):1418–1426, 2007.

[137] Liqian Zhou, Ming Yin, Xi Xu, Xinpan Yuan, and Xiaojun Liu. Non-contact detection of human heart rate with kinect. *Cluster Computing*, pages 1–8, 2018.

[138] Kazuki Nakajima, Tsuyoshi Maekawa, and Hidetoshi Miike. Detection of apparent skin motion using optical flow analysis: Blood pulsation signal obtained from optical flow sequence. *Review of scientific instruments*, 68(2):1331–1336, 1997.

[139] Ali Al-Naji and Javaan Chahl. Remote optical cardiopulmonary signal extraction with noise artifact removal, multiple subject detection & long-distance. *analysis*, 1:1, 2018.

[140] Ran Vas, Claude R Joyner, David E Pittman, and Thomas C Gay. The displacement cardiograph. *IEEE Transactions on Biomedical Engineering*, (1):49–54, 1976.

[141] David L Wilson and David B Geselowitz. Physical principles of the displacement cardiograph including a new device sensitive to variations in torso resistivity. *IEEE Transactions on Biomedical Engineering*, (10):702–710, 1981.

[142] R Guardo, S Trudelle, A Adler, C Boulay, and P Savard. Contactless recording of cardiac related thoracic conductivity changes. In *Engineering in Medicine and Biology Society, 1995., IEEE 17th Annual Conference*, volume 2, pages 1581–1582. IEEE, 1995.

[143] Falk Liebold, Matthias Hamsch, and Claudia Igney. Contact-less human vital sign monitoring with a 12 channel synchronous parallel processing magnetic impedance measurement system. In *4th European Conference of the International Federation for Medical and Biological Engineering*, pages 1070–1073. Springer, 2009.

[144] Axel Cordes, Jérôme Foussier, Daniel Pollig, and Steffen Leonhardt. A portable magnetic induction measurement system (pims). *Biomedizinische Technik/Biomedical Engineering*, 57(2):131–138, 2012.

[145] C. Brüser, C. H. Antink, T. Wartzek, M. Walter, and S. Leonhardt. Ambient and Unobtrusive Cardiorespiratory Monitoring Techniques. *IEEE Reviews in Biomedical Engineering*, 8:30–43, 2015. ISSN 1937-3333. doi: 10.1109/RBME.2015.2414661.

[146] David Friedrich, Xavier L Aubert, Hartmut Führ, and Andreas Brauers. Heart rate estimation on a beat-to-beat basis via ballistocardiography-a hybrid approach. In *Engineering in Medicine and Biology Society (EMBC), 2010 Annual International Conference of the IEEE*, pages 4048–4051. IEEE, 2010.

[147] Daniel Waltisberg. *Sleep assessment using bed-mounted sensors*. PhD thesis, ETH Zurich, 2017.

[148] David C Mack, James T Patrie, Robin A Felder, Paul M Suratt, and Majd Alwan. Sleep assessment using a passive ballistocardiography-based system: Preliminary validation. In *Engineering in Medicine and Biology Society, 2009. EMBC 2009. Annual International Conference of the IEEE*, pages 4319–4322. IEEE, 2009.

[149] Takashi Watanabe and Kajiro Watanabe. Noncontact method for sleep stage estimation. *IEEE Transactions on biomedical engineering*, 51(10):1735–1748, 2004.

[150] Kwang Suk Park and Heenam Yoon. Ballistocardiography. In *Seamless Healthcare Monitoring*, pages 127–155. Springer, 2018.

[151] Lauren Samy, Ming-Chun Huang, Jason J Liu, Wenyao Xu, and Majid Sarrafzadeh. Unobtrusive sleep stage identification using a pressure-sensitive bed sheet. *IEEE Sensors Journal*, 14(7):2092–2101, 2014.

[152] Farideh Ebrahimi, Seyed-Kamaledin Setarehdan, Jose Ayala-Moyeda, and Homer Nazeran. Automatic sleep staging using empirical mode decomposition, discrete wavelet transform, time-domain, and nonlinear dynamics features of heart rate variability signals. *Computer methods and programs in biomedicine*, 112(1):47–57, 2013.

[153] Meng Xiao, Hong Yan, Jinzhong Song, Yuzhou Yang, and Xianglin Yang. Sleep stages classification based on heart rate variability and random forest. *Biomedical Signal Processing and Control*, 8(6):624–633, 2013.

[154] Stephen James Redmond and Conor Heneghan. Cardiorespiratory-based sleep staging in subjects with obstructive sleep apnea. *IEEE Transactions on Biomedical Engineering*, 53(3):485–496, 2006.

[155] Stephen J Redmond, Philip de Chazal, Ciara O'Brien, Silke Ryan, Walter T McNicholas, and Conor Heneghan. Sleep staging using cardiorespiratory signals. *Somnologie-Schlafforschung und Schlafmedizin*, 11(4):245–256, 2007.

[156] Tim Willemen, Dorien Van Deun, Vincent Verhaert, Marie Vandekerckhove, Vasileios Exadaktylos, Johan Verbraecken, Sabine Van Huffel, Bart Haex, and Jos Vander Sloten. An evaluation of cardiorespiratory and movement features with respect to sleep-stage classification. *IEEE journal of biomedical and health informatics*, 18(2): 661–669, 2014.

[157] Nicholas R Lomb. Least-squares frequency analysis of unequally spaced data. *Astrophysics and space science*, 39(2):447–462, 1976.

[158] Jeffrey D Scargle. Studies in astronomical time series analysis. ii-statistical aspects of spectral analysis of unevenly spaced data. *The Astrophysical Journal*, 263:835–853, 1982.

[159] Keinosuke Fukunaga. *Introduction to statistical pattern recognition*. Elsevier, 2013.

[160] Pierre A Devijver and Josef Kittler. *Pattern recognition: A statistical approach*. Prentice hall, 1982.

[161] Thomas M Cover, Peter E Hart, et al. Nearest neighbor pattern classification. *IEEE transactions on information theory*, 13(1):21–27, 1967.

[162] Kagan Tumer and Joydeep Ghosh. Bayes error rate estimation using classifier ensembles. *International Journal of Smart Engineering System Design*, 5(2):95–109, 2003.

Appendix A

Supplimental material for Chapter 4

A.1 Replicated methods

A.1.1 Lee's method

In this method, the signals from all the load cells are first windowed with length of five seconds and band-pass filtered (5th order Butterworth with 1 to 20 Hz pass band). Then, the resulting signal is differentiated and passed through a nonlinear transformation resulting in the Shannon entropy (SE) values. Finally, a moving average is applied on the output of the SE process for further smoothing. Peak detection is eventually performed on the automatically selected optimal result from one of the four load cells. The next window is then defined to begin 0.2 seconds after the last detected peak in the current window. Since Lee's method was proposed for data sampled at 1000 Hz, and our sampling rate is 250Hz, we also tested an up-sampled BCG for this method to assess the impact of the sampling rate mismatch on the performance of this method.

A.1.2 Lydon's method

In the Lydon method, windowing is applied on the preprocessed BCG (6^{th} order Butterworth with 0.7 to 10 Hz pass band). The length of the window is proposed to be 0.3 seconds that

will move across the BCG every 0.01 seconds. Then the energy of each sliding window is obtained. The peaks in the resulting signal is supposed to correspond to the BCG and thus is considered for peak detection. Since this method was proposed for data sampled at 100 Hz and again different with what we have sampled our data at, a down-sampled BCG was tested for this method too. Furthermore, two moving-average filters were added to the Lydon method to reduce the large number of false positives that were found in our data; this addition can be justified by the use of a similar filter in Lee and similarity between Lee and Lydon's methods (we later learned from the original code that such a smoothing was included but not mentioned in the paper).

A.1.3 Brüser's method

Brüser also proposes a sliding window method, but takes a statistical approach to estimate heartbeat intervals (HBI's) within that sliding window at each iteration constrained to two "upper and lower thresholds" based on prior knowledge of typical HR range. This method has two main parts, the "basic" and the "extended" parts of the algorithm.

In the "basic" part of the algorithm a sliding window or as they call it "analysis window" centered at a given point in time is selected. The length of the "analysis window" is restricted to less than twice the "upper threshold" for time between two heartbeats to ensure inclusion of at least two heartbeat events. A level thresholding is applied to each sliding window for motion artifact removal. Then, a local interval length is estimated in each sliding window using the estimators "Modified autocorrelation", "Modified average magnitude difference function (AMDF)" and "Maximum amplitude pairs (MAP)" at each window. The term "Modified" is prefixed for the first two estimators due to varying length of the sliding window. The mentioned estimators are then fused to obtain a "Probabilistic estimator" for the beat to beat interval. For the definitions of the mentioned estimators and the fusion algorithm in use, please refer to the original work.

The "extended" part of the algorithm makes use of the redundant peaks introduced due to the sliding window in the "basic" part. All the estimates around the centers of each

sliding window are narrowed down and merged using a confidence threshold constrained under two conditions. The conditions are: 1. the peaks should be apart by approximately the length of the local interval for a given center; and 2. they must be mirrored about the center of the sliding window. Then if such peaks have the largest combined amplitudes, they were called the "boundary peaks" of the interval and the peak to the right of the center was referred to as the "anchor point". These anchor points were later used to group the interval estimates together and are "irrelevant" to the final interval estimation. In order to exclude unreliable estimates from the set, a "quality indicator" or "confidence indicator" $\overline{Q_k}$ is derived by averaging the individual confidence values associated with each estimate and then a fixed threshold th_Q to be applied to each $\overline{Q_k}$. As can be inferred from the original paper, th_Q is a subject-specific threshold.

A.1.4 Alvarado's method

This work applies a continuous wavelet transform (CWT) with B-Spline wavelets on the band pass filtered BCG (0.5-20Hz 2^{nd} order). Then it is hypothesized that the zero crossings in the 5^{th} scale of CWT of the BCG correspond to the J-Peaks of the original BCG. Once the 5^{th} scale CWT of the BCG is obtained the rest of their work emphasizes more on how those zero crossings in the new CWT signal are automatically identified by use of adaptive level and interval thresholds to avoid false zero crossing events and consequently false J-Peaks. The process has two steps of "Learning Stage" and "Decision Stage". In the "Learning Stage", a set of detection thresholds to detect the first four beats is defined and a J-J interval average is estimated. Also, a "refractory period" of 300 ms is introduced in this stage to avoid false detection. In the "Decision Stage", the information from the "Learning Stage" is used as initial values based on which new level and J-J interval thresholds are estimated and decisions made on peak detection. This process continues in this manner till the end.

A.1.5 Sadek's method

In this method the band-pass filtered BCG (Chebyshev 2.5 to 5 Hz pass band and sampled at 50 Hz (or based on the paper, Butterworth 1 to 10 Hz pass band)) is decomposed into approximation and detail coefficients using MODWT. Then the 4th level "smooth coefficient" is selected for ten-second-long windowing and peak detection. The wavelet applied in the decomposition is the 8^{th} order Symlet (Sym8 in MATLAB). The peak detection part is not described in detail, but from our inspection of the python code we were provided with, appears very similar to the built-in function "findpeaks()" in MATLAB.

A.1.6 Simple cross-correlation method

For the cross correlation (XCOR) method, the BCG underwent preprocessing steps identical to what is proposed in Lydon method. Then a single BCG complex is picked as a template for performing the cross-correlation step and then using it for peak detection.

A.2 Parameters of interest in each method

Lee, Lee with up-sampled BCG (Lee-US), Lydon, Lydon with down-sampled BCG (Lydon-DS) and XCOR methods use two moving-average filters for smoothing purposes and the lengths for the filters had to be adjusted. The lengths of the filters were mostly subject-specific for Lee and Lydon methods and subject-independent for XCOR method with the exception of only one participant. The BCG for that particular participant had to be removed later from the study as cross-correlation method failed to obtain non-zero detect and false peaks which made it impossible to calculate the MAE_p.

For the peak detection step, the "findpeaks" built-in function of MATLAB seems very likely to have been used in the original work of Lee and we used it for Lee-US, Lydon, Lydon-DS and XCOR methods as well. We also had to tune the "Mininimum Peak Prominence" input of the mentioned MATLAB built-in function, "findpeaks". Therefore, this was a two-step optimization process. First, for a certain value of "Mininimum Peak Prominence" that

produced a reasonable pair of Det. and FAR, the lengths for the moving average filters were optimized. Then using those optimal window lengths, "Mininimum Peak Prominence" was iterated over different values to produce the ROC curves and a value for "Mininimum Peak Prominence" was selected.

For Brüser Method, we had to first find an optimal value for the percent-overlap of the "analysis window". A single value for this parameter turned out to be optimal for all other BCGs from the other participants. Next, the "confidence indicator threshold", th_Q, as discussed when introducing Brüser method was tuned to yield good performance in terms of "anchor points" or peaks elaborated earlier. Per our understanding from the original work, this threshold has to be adjusted for the BCG data from each participant.

In Alvarado method, since the process is adaptive, any alterations to their proposed constants or initial values for their proposed parameters turned out to have no effect on the performance of this method. Therefore, those parameters were set to the same values as initially proposed. However, the scale of the wavelet component of the BCG used for peak detection, and the choice of wavelet for decomposition were affecting the performance of this method significantly for our data. Since scale 5 of the CWT was resulting in very poor performance for our data, we tried a range of scales until an acceptable range of scales was found. Then within that range, scale numbers specific to each BCG set was selected for optimal performance. For the choice of an optimal wavelet, MATLAB provides family of "bior" wavelets that implement a B-Spline wavelet with bi-orthogonality and different members of this family proved to be optimal for some of the BCG sets. For the BCG sets where an optimal member from the "bior" family was not found, a member from its inverse, "rbio", or a member from the "sym" family was used. It is worth mentioning that for the cases where a wavelet was not optimal, the performance was severely affected and therefore sticking to a single wavelet was avoided in order not to penalize this method harshly. A summary of wavelets and scale combination is reported in Table A.1.

For Sadek method, the first author assisted us by providing python code for it. Therefore, little ambiguity were left to address in implementing their code in MATLAB. Due to different sampling frequency (50Hz vs 250Hz which affects level selection in the wavelet transform), we

did have to run some experiments to optimize for the right wavelet decomposition scale and window length. A summary of wavelet decomposition scales and window lengths used in this method for different participants is provided in Table A.2. Since the python code was using "minimum peak distance" as a parameter to help find the peaks in the peak detection code, the same parameter was used with MATLAB in this work to be consistent with the original work when comparing the performance. Clearly, different values for the mentioned parameter affect the overall performance of the method significantly and therefore this parameter was also considered for optimization. It is worth mentioning that this parameter is not specified in the paper and in the code we were provided with, a value of 1 i.e. one sample was assigned to this parameter which was introducing tremendous number of false peaks and that was another reason to optimize for that parameter. The drawback of using "minimum peak distance" is that we need to have prior knowledge about heartbeat distances in order to assign a value for this parameter which makes peak detection hard in an online scenario. In addition, the mentioned parameter was not used in Lee, Lee-US, Lydon, Lydon-US and cross-correlation methods which makes the comparison task harder. Therefore, the performance of this method is evaluated based on the "minimum peak prominence" values as well. When optimizing for this parameter, the decomposition scales determined earlier were first used to find a value for the "minimum peak prominence" parameter such that a good pair of detection and FAR was obtained. Then, using the values found for the "minimum peak prominence", the performance of the method was tested again for different decomposition scales to check if a different scale would be optimal in this scenario. During this process, different scales proved to be optimal for only BCGs from three participants. For those BCGs, a new set of "minimum peak prominence" parameters corresponding to the optimal scales were then sought.

A.3 Wavelets and wavelet decomposition scales

Table A.1 summarizes the combination of wavelet and wavelet decomposition levels used to optimize the performance of Alvarado method. The "Number of Participants" column

indicates the total number of participants for whom a certain combination of wavelet and decomposition level that resulted in good performance for the method.

Table A.1: Wavelet name and wavelet component used to optimize the performance of Alvarado method for different participants

Number of Participants	Wavelet Name	Decomposation Levels
13	bior2.2	37, 30, 48, 37, 42, 32, 20, 49, 34, 50, 25, 47, 31
4	bior3.9	59, 76, 61, 41
7	bior4.4	34, 32, 48, 29, 29, 28, 19
4	rbio3.9	68, 31, 50, 50
1	sym4	25
1	sym8	39

Table A.2, summarizes the wavelet decomposition scales (left) and window lengths (right) used to optimize the performance of Sadek method. Again, the "Number of Participants" column indicates the total number of participants for whom a certain wavelet component and window length maximized the performance of the method.

A.4 Signal quality index

The process of signal quality index (SQI), is based on Matched Filter approach [128]. The matching is performed by comparing the signal in question with a known signal by obtaining the correlation coefficient of the two [128]. In order to have a known BCG, BCG stream is segmented and the ensemble average of the segments is taken [128]. In order to figure out the starting point for each segment, R-peaks of the ECG were used as reference points; the ECG was simultaneously recorded with the BCG. The minimum R-R interval was used for the length of each BCG segment in [128].

In our case however, the segments' lengths were left to be the same distance between their corresponding R-R interval. This lead to unequal lengths of the segments. The length deficiencies were corrected by zero padding the short vectors; and when obtaining the ensemble averages, the zeros were excluded in the calculation.

Table A.2: Left: Wavelet component used to optimize the performance of Sadek method for different participants. Right: Window lengths used to optimize the performance of Sadek method for different participants.

Number of Participants	Decomposition Scale
4	4
9	5
17	6

Number of Participants	Window Length
1	16
1	12
7	14
21	10

The obtained ensemble average is considered to be the known signal [128] or the "main template" as referred to it in [128]. In addition, sub-templates were also made out of a number of adjacent BCG segments such that sum of all those numbers will add up to the total number of BCG segments in the stream.

Correlation coefficients were obtained by matching each sub-template with the main template and the average of all the resulting correlation coefficients was called SQI [128].

Appendix B

Nighttime vital signs recording system

B.1 Introduction

This appendix provides a description of the building blocks of a long-term health monitoring system. In addition to the basic circuitry necessary to detect and record BCG, this system is equipped with additional features necessary for a DAQ system that is intended to dwell in a home sitting of a person under study. The mentioned necessary parts and features are described in the subsequent sections.

B.2 DAQ system description

The basic building block for this system is made of the signal conditioning circuit described in 2.4 and data acquisition configuration III described in 2.5.3. The data acquisition configurations introduced in 2.5.1 and 2.5.2 are modified and re-arranged slightly to adapt the Configuration III and to address some issues concerning home-based remote data acquisition. Recall that Configuration III was suffering from the interfacing limitation with the host PC. This limitation can be overcome by employing a Raspberry Pi unit. In addition including a

Raspberry Pi unit to the design makes interfacing to the cloud services significantly easier.

B.2.1 Recording control and observation

In order to provide the user sufficient control over the system, controlling push-buttons are provided to help the user stop data recording when not desired and re-start recording when desired. In addition, visual indicators are provided by means of LEDs to make the system observable so the user know that the system has acknowledged their command to whether start or stop recording. This part is integrated in the DAQ board and its circuit diagram is provided in Appendix C Fig. C.3.

B.2.2 Ambient disturbance detector

An audio envelop amplifier is also included in the system to pickup noticeable ambient noise without providing further auditory details due to privacy concerns. The recorded audio envelops will help as a reference in case noisy segments of BCG is observed to confirm if the noise is due to the environment or the system. In addition, the noise reference can be used for further cleaning up the obtained BCG using adaptive filter approaches.

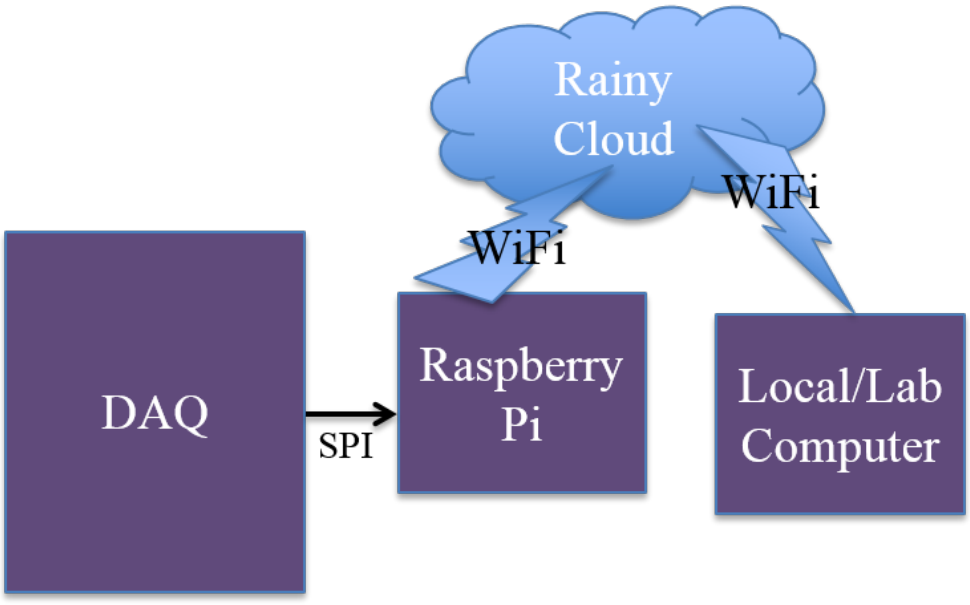

Figure B.1: The overall system overview.

The DAQ block in the diagram of Fig. B.1 is further detailed in Fig. B.2. The Sig. Cond blocks refer to the signal conditioning boards described in 2.4 which provides signal conditioning to the load cell signals. Based on results of Chapter 2 (Table 2.1), a signal conditioning in the vicinity of load cell helps maintain a better SNR for the signal.

The EMFi Sig. Cond block represent signal conditioning circuit that processes the signal from the EMFi. This circuit is similar to the Sig. Cond. circuit with one difference that the instrumentation amplifier is replaced with a charge amplifier. EMFi sensors are conisered in the design to provide redundancy in hardware for BCG detection.

Aud Env Amp block represents the audio amplifier circuit necessary to provide ambient noise detection capability. This part is integrated in the DAQ board and its circuit diagram is provided in Appendix C Fig. C.4.

A circuit-level detail and PCB layout of the DAQ board is provided in Fig. B.3 and Fig. B.4 respectively. Circuit diagrams for other peripheral parts necessary to run the system are included in Appendix C Fig. C.5 through C.9. A PCB realization of the layout in Fig. B.4 is shown in Fig. B.5.

B.3 Raspberry Pi

Raspberry Pi unit is a Unix-based platform that operates as an stand-alone PC. Its robust WiFi and Ethernet interfaces makes its connection to the internet very easy. In addition, availability of I^2C and SPI interface on its header board makes it possible to interface ADC with it. Thus, it becomes a system of choice for our long-term home-based application.

B.4 Preliminary tests

The ADC in use in the DAQ system provides multiplexed channels with both options of differential and single-ended modes. Furthermore, the Raspberry Pi unit provides 5 V and 3.3 V power supply pin-outs on its header interface while it was also possible to implement power supply on the DAQ board. In order to decide on the best option, preliminary sine

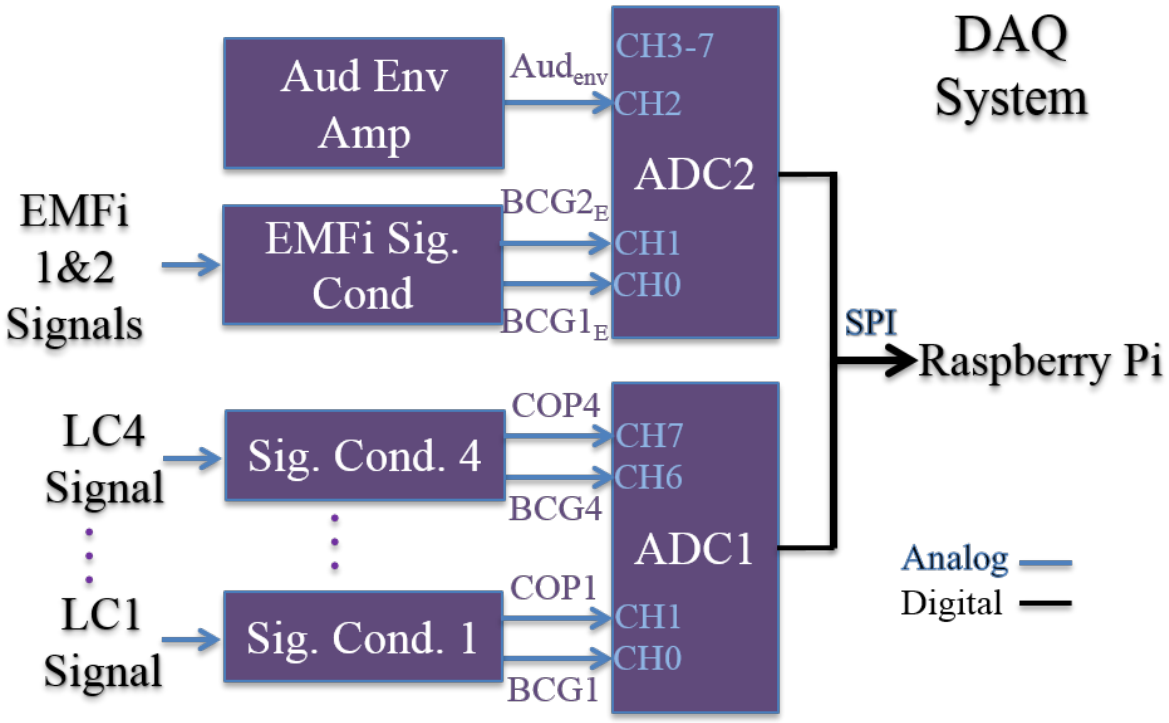

Figure B.2: DAQ block description.

Table B.1: ADC Input, and Power Supply effects on the sine wave SNR

ADC Input	Power Supply	SNR	Remarks
Single Ended	3.3 from Pi Unit	28.61839	
Single Ended	3.3 regulated from 5v on ADC board	26.63543	
Differential	3.3 regulated from 5v on Pi Unit	26.57994	Regulator on ADC board
Differential	3.3 from Pi Unit	25.50507	
Single Ended	3.3 regulated from 5v on Pi Unit	25.21033	Regulator on ADC board
Differential	3.3 regulated from 5v on ADC board	25.05374	

wave tests were performed. Table B.1 provides the details of the test as well as the results in terms of SNR values. The SNR values were obtained by applying a low amplitude sine wave to the ADC and recording the ADC results in the PC. Then snr function of MATLAB was used to evaluate the SNR similar to what was done in 2.6.1.

Based on the SNR values provided in Table B.1, we decided to use the ADC channels in

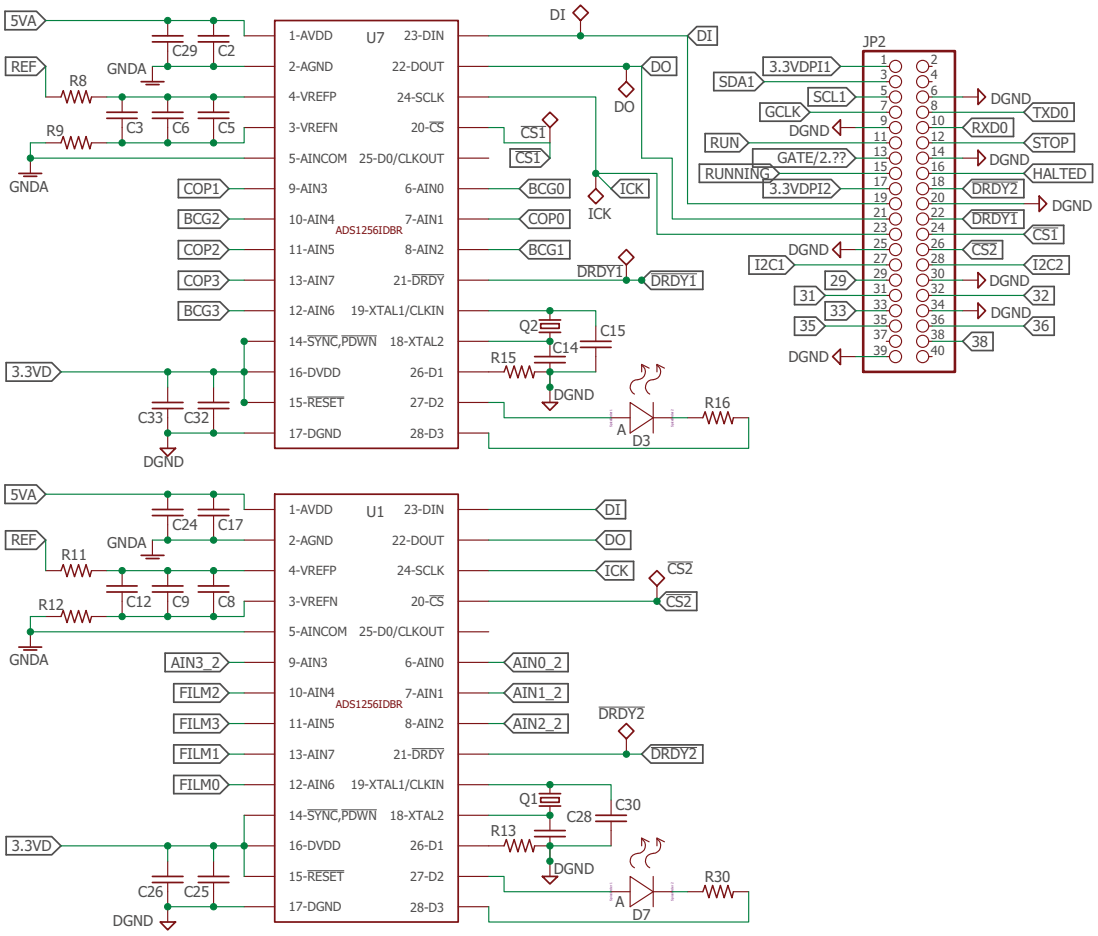

Figure B.3: Circuit diagram implementing the multi-channel ADC-based DAQ.

single ended mode. Also, the 3.3 V power supply provided by the Raspberry Pi unit was selected. A layout spot was still provided on the DAQ board for providing space for a voltage regulator in case external power supply would be required in the future.

B.5 Current status

Successful sine wave test as reflected from the results provided in B.4 has been performed. However, this was limited to smaller number of channels to be sampled or if all channels were to be sampled, lower sampling rates (as low as 125 Hz) had to be considered.

Successful far end data communication with host PC has also been tested. Counters were sent by the Raspberry Pi unit to a cloud based server and the host PC was able to

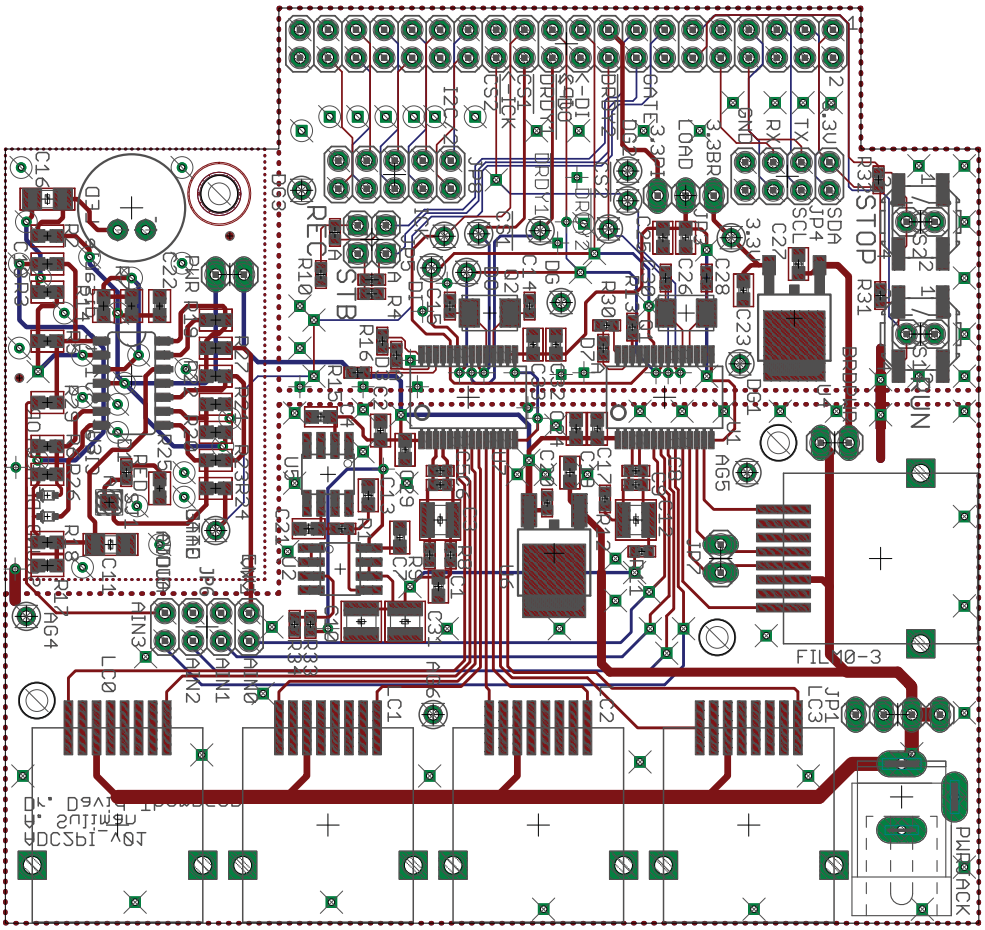

Figure B.4: Board layout for the circuit diagram implementing the multi-channel ADC-based DAQ.

access, download and interpret them. Bandwidth was not an issue either for the data rates addressing our needs.

B.6 Limitations and alternative solutions

As mentioned earlier, Raspberry Pi unit was introduced to provide a solution to the problem of data acquisition in the far-end by facilitating Ethernet or WiFi. However, the SPI interface provided by this unit does not perform well for real-time applications as pointed out in B.5. The issue is related to the general purpose operating system on the Raspberry Pi unit. This leads to scheduling-related delays in communication with ADC over the SPI. Consequently, unevenly samples were being recorded around the specified sampling rate.

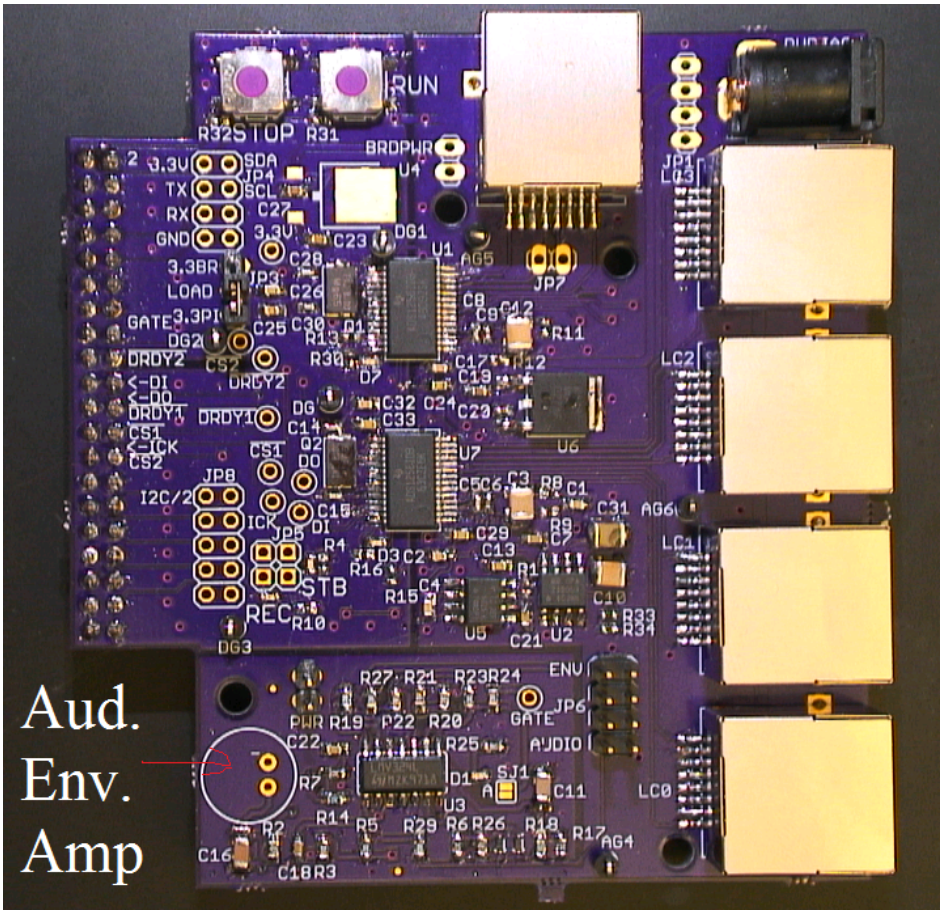

Figure B.5: Board layout realization for the circuit diagram implementing the multi-channel ADC-based DAQ.

The problem can be addressed in two ways: (*i*) installing a real-time operating system or (*ii*) including a microcontroller between the Raspberry Pi unit and the DAQ board. While the former solution is not immediately pursued due to limited expertise in the real-time operating system domain, the latter solution is tested. The microcontroller takes over the responsibility of evenly sampling on its interface with ADC over the SPI. Then with a second SPI module it communicates with the Raspberry Pi unit. However, this solution is pending on proper handshaking protocols and data handling between the microcontroller and the Raspberry Pi unit and is expected to be addressed soon.

The circuit diagram for the intermediate microcontroller is provided in Fig. B.6 and the PBC implementation is shown in Fig. B.7. Other peripherals needed in implementing this system in Appendix C Fig. C.10 and Fig. C.11.

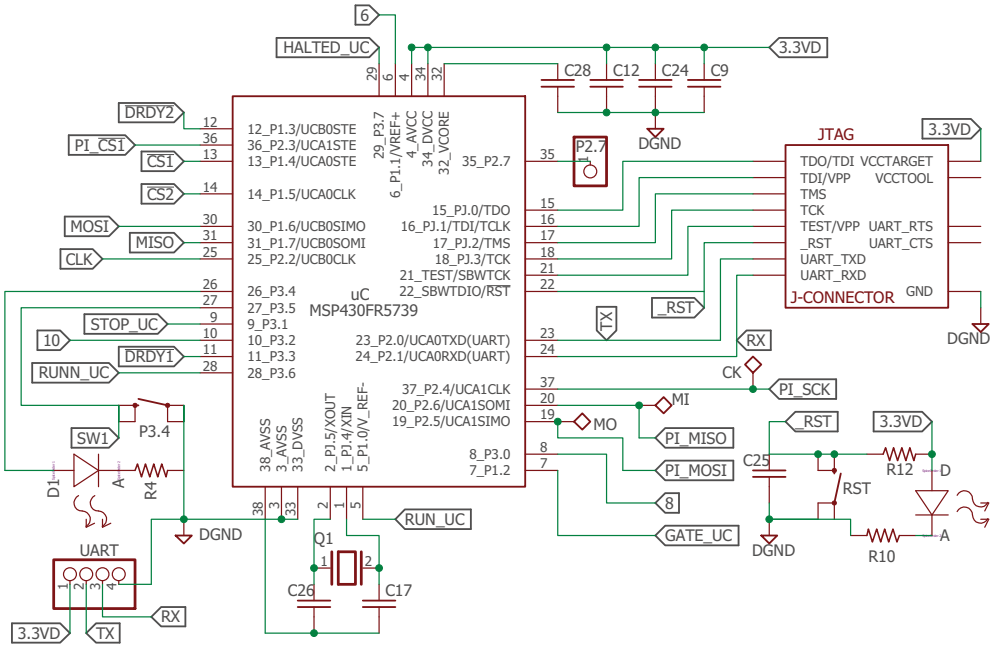

Figure B.6: microcontroller circuit diagram for interconnection between DAQ and Raspberry Pi unit.

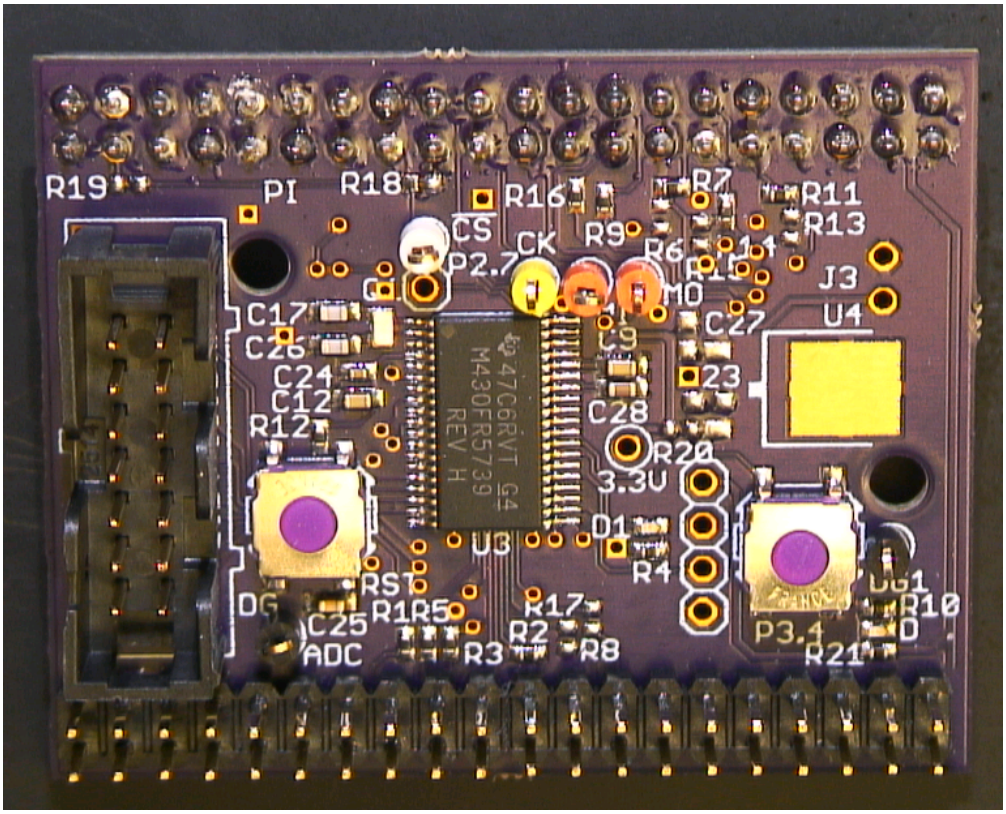

Figure B.7: PCB implementation of the microcontroller circuit diagram for interconnection between DAQ and Raspberry Pi unit.

Appendix C

Bill of Material

This appendix includes additional peripheral circuits necessary of the operation of the core material proved in Chapters 2 and B. In addition, bill of material used in realizing the circuits is provided.

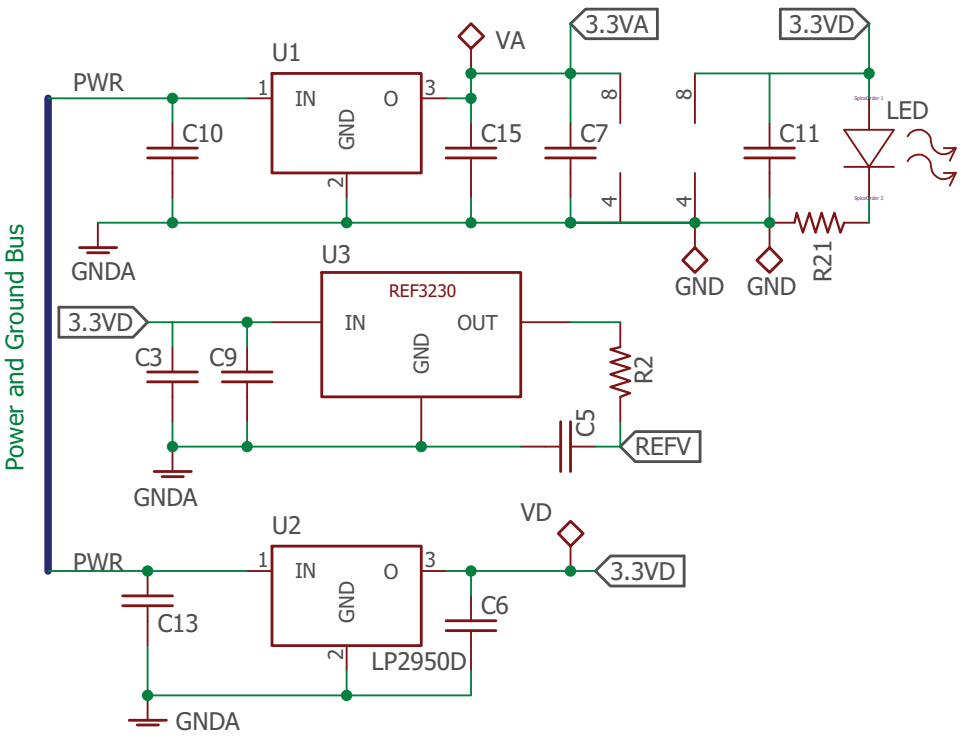

Figure C.1: Power supply circuit used in the circuits of Fig. 2.3 and Fig. 2.6

Fig. C.5 provide detail diagram of terminated PCB wires to the jumpers. The terminated

Item	Qty	Ref	Part	MFR	MFR#	SPEC	Footprint	Qty needed for 4 Systems	Comments
1	2	C26, C28	0.056uF			Ceramic, SMD, C-SMD0603	SMD0603	8	
2	5	C1, C3, C7, C24, C27	0.1uF			Ceramic, SMD, C-SMD0603	SMD0603	20	
3	2	C10, C13	0.33uF			Ceramic, SMD, C-SMD0603	SMD0603	8	
4	1	C9	0.47uF			Ceramic, SMD, C-SMD0603	SMD0603	4	
5	10	C2, C4, C5, C6, C11, C12, C15, C16, C29, C30	1uF			Ceramic, SMD, C-SMD0603	SMD0603	40	
6	4	C14, C17, C25, C31	10uF			Ceramic, SMD, C-SMD0603	SMD0603	16	
7	3	C18, C19, C20	0.01uF			Ceramic, SMD, C-SMD0402	SMD0402	12	
8	3	C21, C22, C23	0.1uF			Ceramic, SMD, C-SMD0402	SMD0402	12	
9	1	C8	6.8uF			Polarized Alum. Cap. TH	TH	4	Will be mounted later
10	1	R9	0.2			R-SMD0402	SMD0402	4	
11		ROPEN				R-SMD0402	SMD0402	4	No to be populated
12	3	R11, R15, R18	100			R-SMD0402	SMD0402	12	
13	2	R7, R21	1K			R-SMD0402	SMD0402	8	
14	10	R1, R2, R3, R5, R10, R12, R13, R14, R16, R17	10K			R-SMD0402	SMD0402	40	
15	1	R8	20K			R-SMD0402	SMD0402	4	
16	2	R6, R19	30K			R-SMD0402	SMD0402	8	
17	1	R4	100K			R-SMD0402	SMD0402	4	
18	1	R20	300K			R-SMD0402	SMD0402	4	
19	1	LED				SMD0402	SMD0402	4	
20	2	U1, U2	LP2950D			TO252	TO252	8	
21	1	U3	REF3230			SOT23 - 6	SOT23 - 6	4	
22	1	U4	LM2904			8-SOIC	8-SOIC	4	
23	1	U5	INA122U			8-SOIC	8-SOIC	4	
24	1	U6	OPA2333D			8-SOIC	8-SOIC	4	
25	1	U7	THS4281			8-SOIC	8-SOIC	4	
26	2	U8, U9	ADS8866			10 VSSOP	10 VSSOP	8	
27	3	U10, U11, U12	DS90LV019			14 TSSOP	14 TSSOP	12	
28	2	IN, OUT	RJLSE4238101T				SMD	8	

Figure C.2: Bill of material for the circuits in Fig. 2.3 and Fig. 2.6.

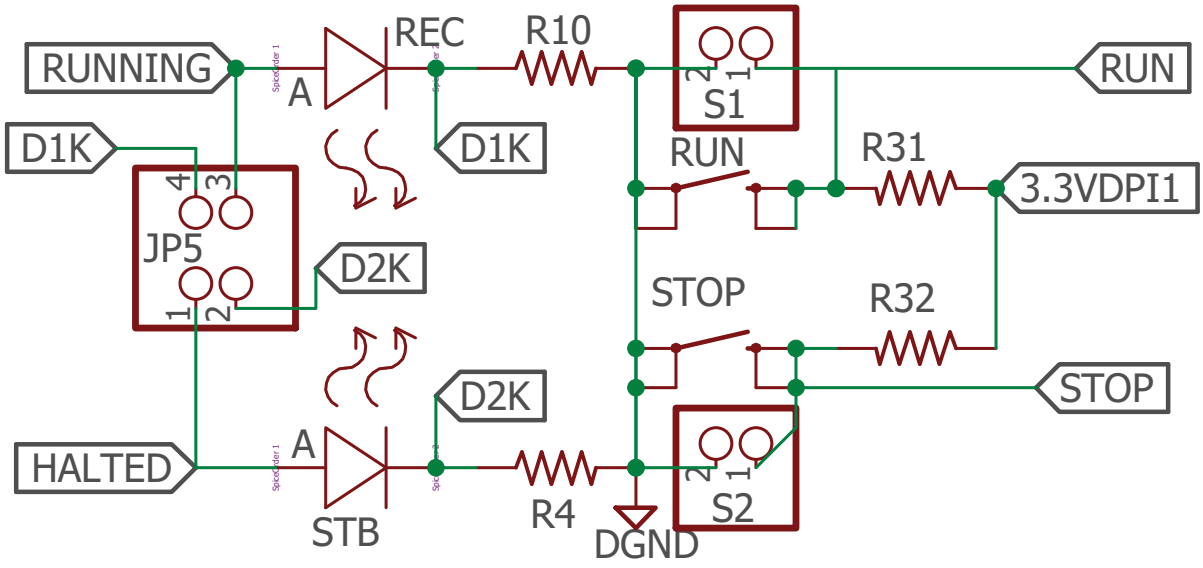

Figure C.3: Circuit diagram detailing the recording control and indicator part.

wires are labeled in the circuits of Fig. B.6 and Fig. C.10. The corresponding labels also appear in the Fig. C.5. These jumpers provide flexibility to the system for future requirements in case alternative sources would be required to be connected to the ADC2 of the DAQ system.

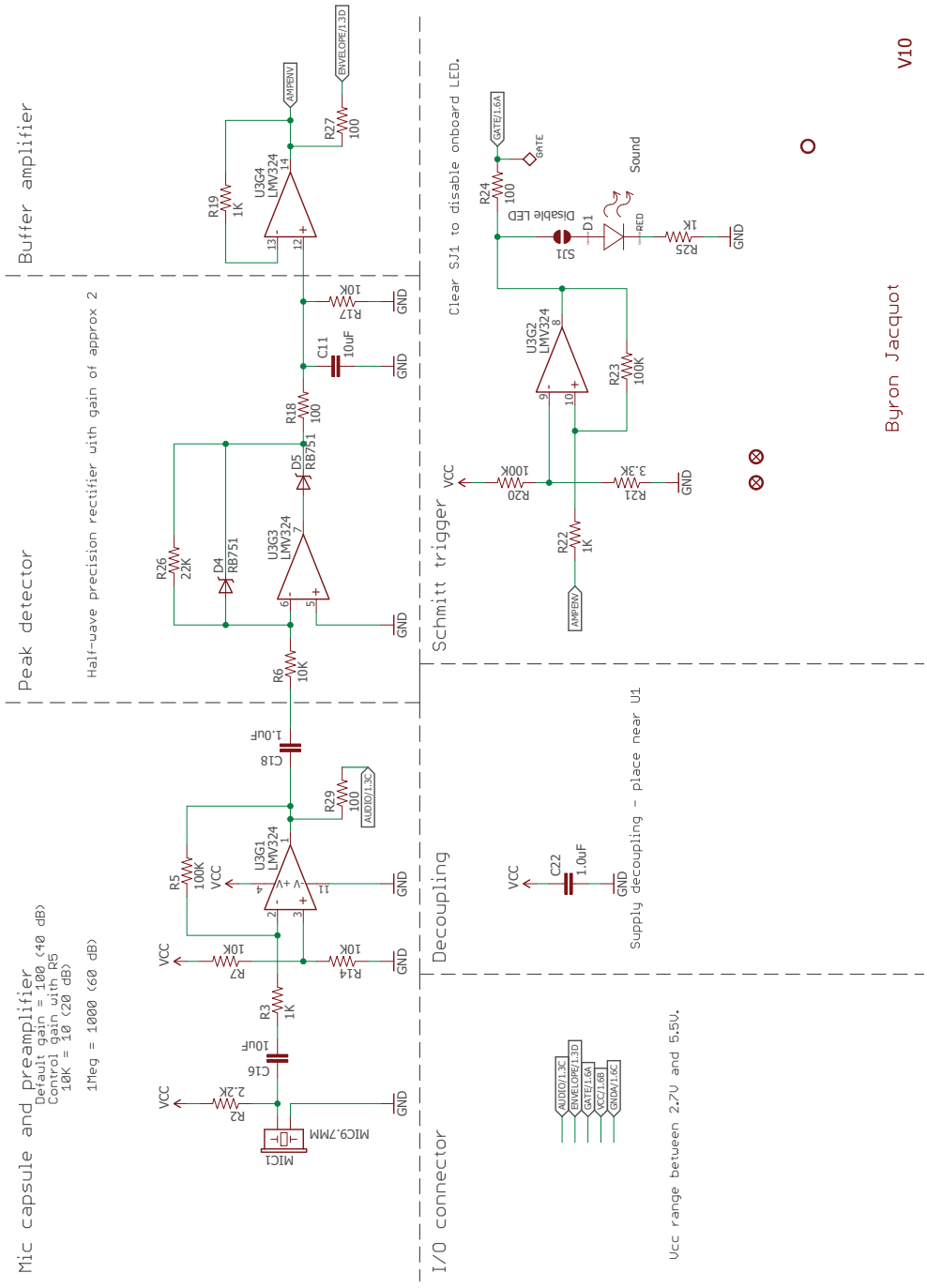

Figure C.4: Audio envelop amplifier for detecting ambient noise and disturbances.

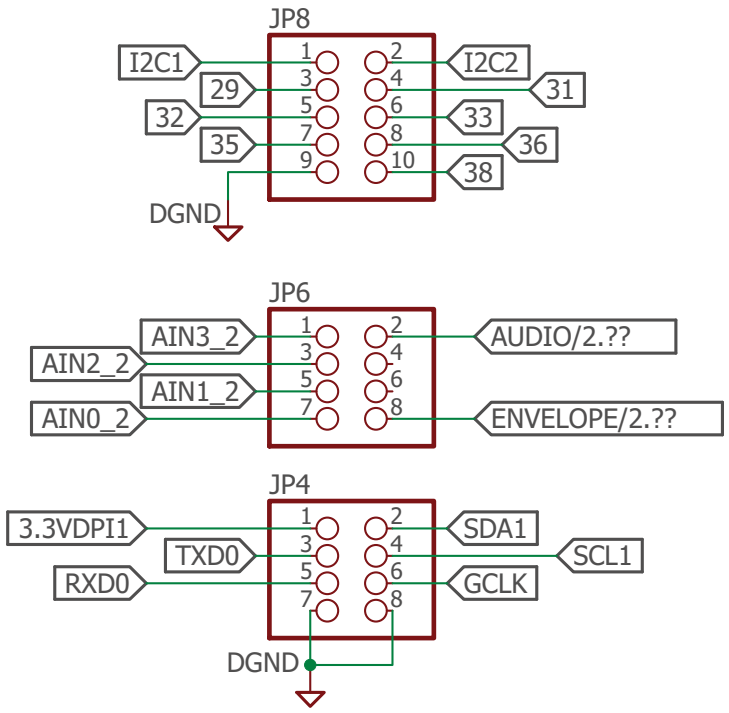

Figure C.5: Jumper headers providing flexible interconnection between various pieces of hardware with the DAQ board.

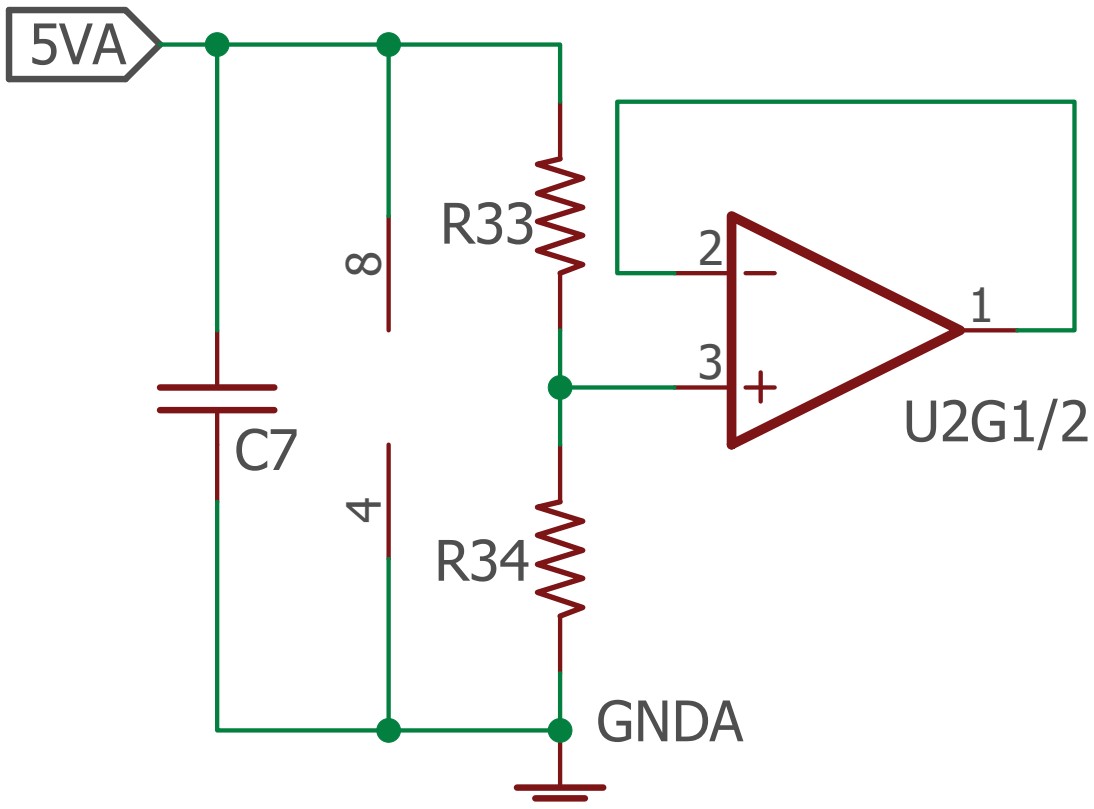

Figure C.6: Circuit diagram for analog ground supply to address dual supply requirement of the devices.

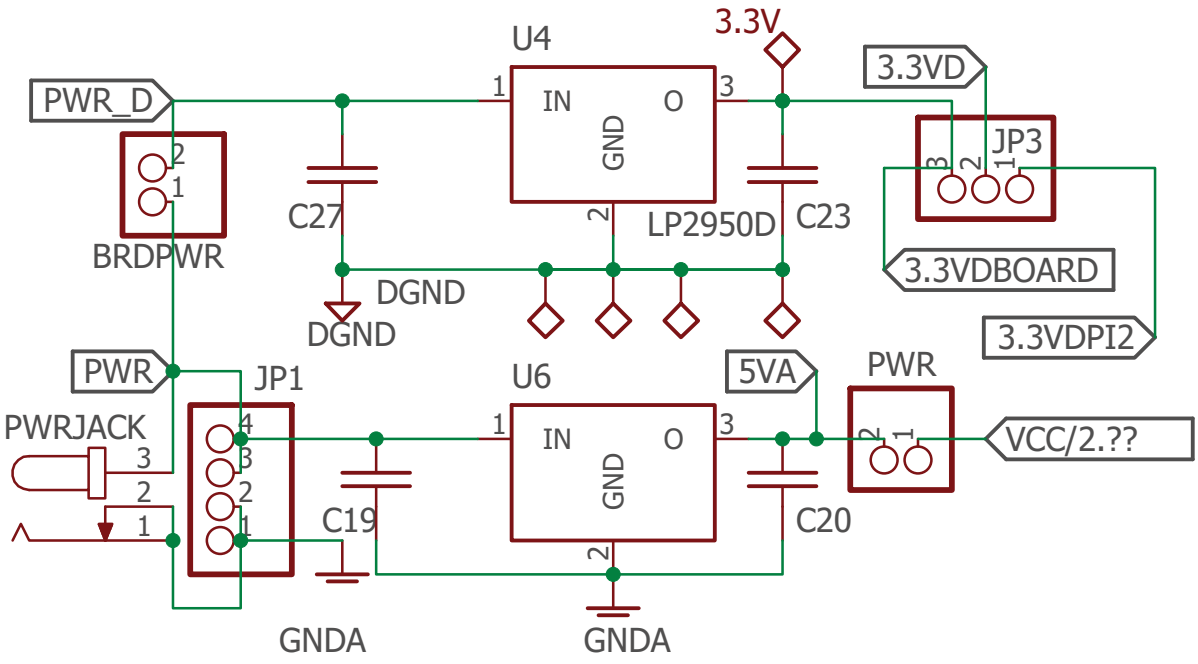

Figure C.7: Circuit diagram of the power supply used in the DAQ board.

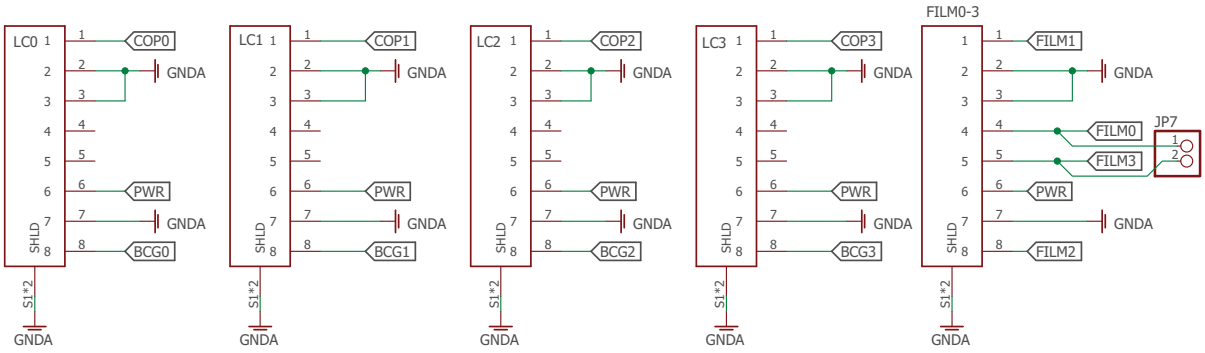

Figure C.8: Wiring diagram of Ethernet jacks providing power and signaling between the signals conditioning boards and the main DAQ board

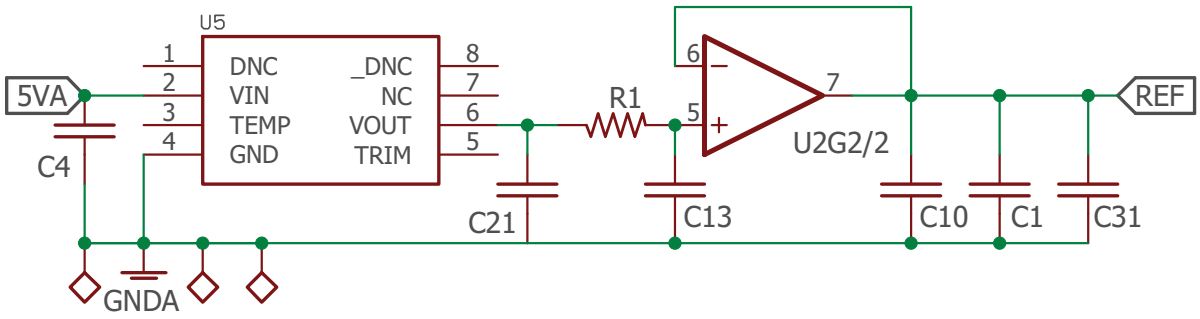

Figure C.9: Circuit diagram for the reference voltage (V_{REF}) regulation necessary for the V_{REF} inputs of the ADC.

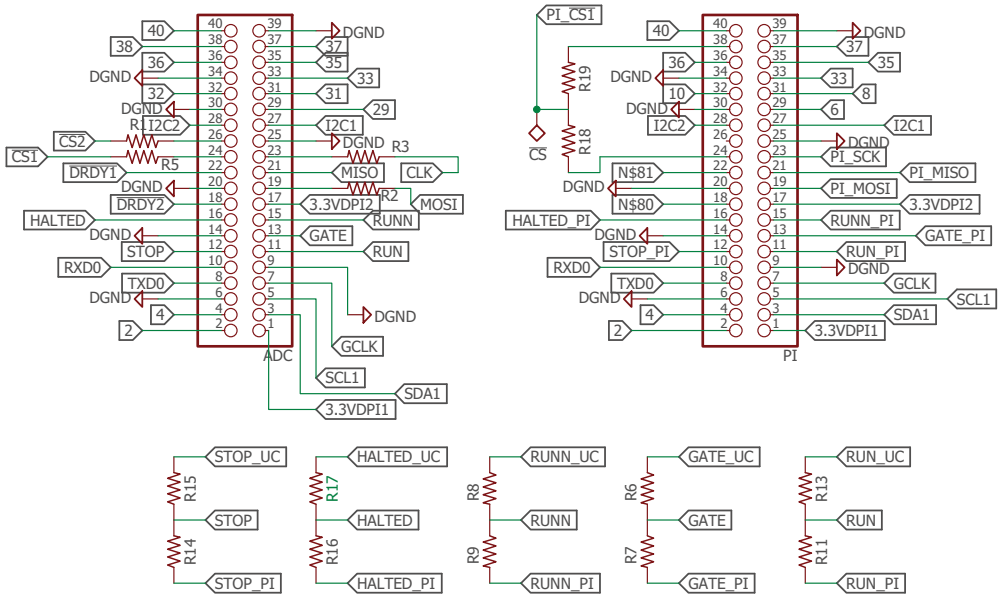

Figure C.10: Interconnection diagram of headers in use on both sides of the microcontroller board.

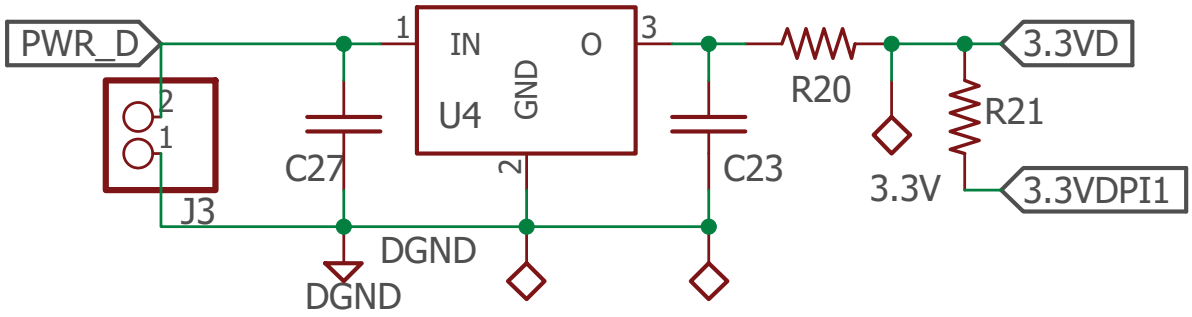

Figure C.11: Circuit diagram of the power supply used in the microcontroller board.

Appendix D

Abbreviations

ADC	Analog to Digital Converter
ANS	Autonomic Nervous System
BBI	Beat-to-Beat Interval
BCG	Ballistocardiogram
COP	Center of Pressure
dBc	Deci bell measuring the noise power density at a given offset from the Carrier.
ECG	Electrocardiogram
HBI	Heartbeat Interval
HPF	Highpass Filter
HR	Heart Rate
HRV	Heart Rate Variability
JJI	J peak to J peak Interval
J peak	The prominent peak of a BCG related to blood ejection at the aortic artery.
LPF	Lowpass Filter
RR	Respiration Rate
RRI	R peak to R peak Interval
R peak	The prominent peak of an ECG related to ventricular contraction events.
SNR	Signal to Noise Ratio
SPI	Serial Peripheral Interface
SVM	Support Vector Machine (SVM)
UART	Universal Asynchronous Receiver/Transmitter